Thermo-mechanical Properties of Mixed Ionic-Electronic Conducting Membranes for Gas Separation

Vasiliki Kallirroi Stournari

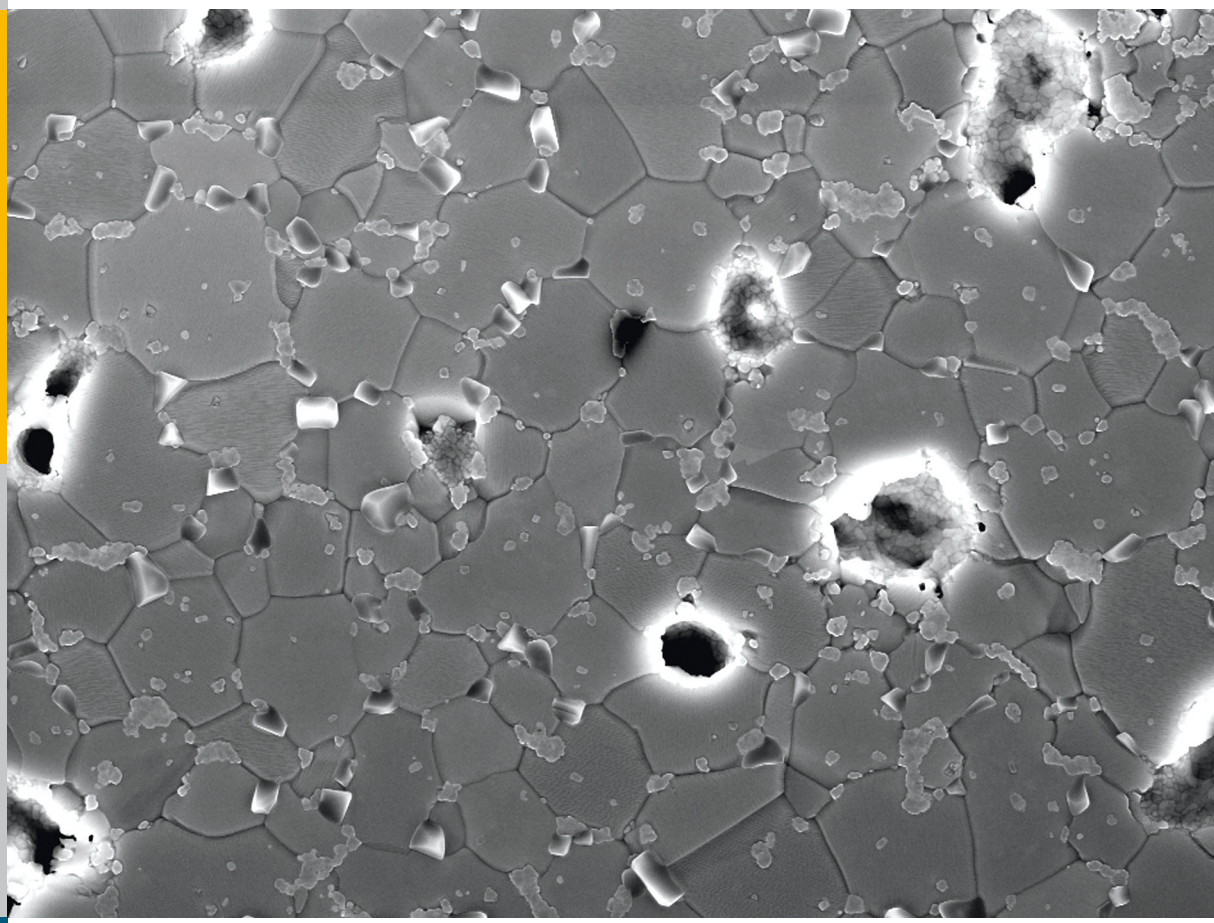

Member of the Helmholtz Association

Energie & Umwelt / Energy & Environment
Band / Volume 304
ISBN 978-3-95806-117-0

JÜLICH FORSCHUNGSZENTRUM

Schriften des Forschungszentrums Jülich
Reihe Energie & Umwelt / Energy & Environment Band / Volume 304

Forschungszentrum Jülich GmbH
Institute of Energy and Climate Research (IEK)
Microstructure and Properties of Materials (IEK-2)

Thermo-mechanical Properties of Mixed Ionic-Electronic Conducting Membranes for Gas Separation

Vasiliki Kallirroi Stournari

Schriften des Forschungszentrums Jülich
Reihe Energie & Umwelt / Energy & Environment Band / Volume 304

ISSN 1866-1793 ISBN 978-3-95806-117-0

Bibliographic information published by the Deutsche Nationalbibliothek.
The Deutsche Nationalbibliothek lists this publication in the Deutsche Nationalbibliografie; detailed bibliographic data are available in the Internet at http://dnb.d-nb.de.

Publisher and Distributor: Forschungszentrum Jülich GmbH
Zentralbibliothek
52425 Jülich
Tel: +49 2461 61-5368
Fax: +49 2461 61-6103
Email: zb-publikation@fz-juelich.de
www.fz-juelich.de/zb

Cover Design: Grafische Medien, Forschungszentrum Jülich GmbH

Printer: Grafische Medien, Forschungszentrum Jülich GmbH

Schriften des Forschungszentrums Jülich
Reihe Energie & Umwelt / Energy & Environment, Band / Volume 304

D 82 (Diss. RWTH Aachen University, 2015)

ISSN 1866-1793
ISBN 978-3-95806-117-0

The complete volume is freely available on the Internet on the Jülicher Open Access Server (JuSER) at www.fz-juelich.de/zb/openaccess.

Abstract

In this work membrane materials with mixed ionic / electronic and protonic / electronic conductivity for oxygen (Oxygen Transport Membranes - OTM) and hydrogen separation (Hydrogen Transport Membranes - HTM) were investigated regarding the thermo-mechanical properties.

In case of OTM, perovskite-type materials $Ba_{0.5}Sr_{0.5}(Co_{0.8}Fe_{0.2})_{1-x}Zr_xO_{3-\delta}$ (BSCF·Z100*x*), where *x* = 0.01, 0.03, 0.05 and 0.1, as well as alternative $SrTi_{1-x}Fe_xO_{3-\delta}$ (ST·F100x) with x= 0.03, 0.05 and 0.07, while the fluorite structured $La_{5.4}WO_{12-\delta}$ (LWO54) and $Nd_{5.5}WO_{12-\delta}$ (NWO55) were investigated as HTM membrane materials. Compressive creep tests were carried out for all compounds in different temperature (900 – 1450 °C) and stress regimes (20 – 100 MPa) in air, vacuum and Ar / 4 % H_2 2.5 % H_2O-atmosphere. The observed activation energies and stress exponents point to diffusional creep as the predominant creep mechanism. In case of BSCF-Z100·x ceramics, this was further supported by the fact that the grain-size-normalized steady-state creep rate varies little for the different BSCF-Z100·x compositions. It was confirmed that Zr substitution does not significantly affect the thermal hysteresis of the creep behavior as observed for pure BSCF. Regarding ST·F100x and LWO54 materials all materials maintained their main structure after the tests. Coming to the HTM materials, the creep mechanism for LWO54 was suggested to be cation aided diffusion with a common migration of La^{3+} / W^{6+} as rate controlling species along grain boundaries / through lattice. ST·F100x, LWO54 and NWO55 materials are promising membrane materials regarding creep resistance.

Elastic and fracture properties were determined for dense and porous tape casted LWO54. Young's moduli via Vickers indentation, ring-on-ring and impulse excitation technique at room and elevated temperatures show a decrease by ~ 20 % when the material is heated up from room temperature to 1000 °C in air and Ar / 4 % H_2 atmosphere. Strength decreases by ~30 % when it is heated up to 1000 °C in air for dense materials while at room temperature it can be increased by a factor ~ 2 for homogeneous microstructure. Subsequent fractographic analysis reveals agglomerates of large irregular pores as fracture origins. For porous LWO54 the strength is decreasing with porosity and the presence of the secondary phase $La_6W_2O_{15}$. Micro-mechanical properties at room temperature by Vickers indentation test are also determined.

Kurzfassung

In der vorliegenden Arbeit wurden keramische mischleitende Membranen mit sowohl elektronischer als auch ionischer / protonischer Leitfähigkeit zur Trennung von Sauerstoff (Sauerstoff-Transport Membran, OTM) und Wasserstoff (Wasserstoff-Transport Membran, HTM) hinsichtlich ihrer thermo-mechanischen Eigenschaften untersucht.

Bezüglich der OTM wurden Materialien mit Perowskitstruktur $Ba_{0.5}Sr_{0.5}(Co_{0.8}Fe_{0.2})_{1-x}Zr_xO_{3-\delta}$ (BSCF·Z100x), mit x = 0,01, 0,03, 0,05 und 0,1, als auch $SrTi_{1-x}Fe_xO_{3-\delta}$ (ST·F100x) mit x= 0.03, 0.05 und 0.07 untersucht. Bezüglich der HTM wurden Materialien mit Flouritstruktur $La_{5.4}WO_{12-\delta}$ (LWO54) und $Nd_{5.5}WO_{12-\delta}$ (NWO55) untersucht.

Für alle Materialien wurden Kriechversuche in verschiedenen Temperatur- und Spannungsbereichen in Luft, Vakuum oder Ar / 4% H_2 2,5% H_2O-Atmosphäre durchgeführt. Die beobachteten Aktivierungsenergien und Spannungsexponenten weisen auf Diffusionskriechen als vorherrschenden Kriechmechanismus hin.

Bei BSCF·Z100x Keramiken wird dieses durch die Tatsache unterstützt, dass die auf die Korngröße normalisierte stationäre Kriechrate für die verschiedenen BSCF·Z100x Zusammensetzungen wenig variiert. Es konnte bestätigt werden, dass eine Zr-Dotierung nicht signifikant die thermische Hysterese des Kriechverhaltens verändert, wie man es bei reinem BSCF beobachtet. Die ST·F100X und LWO54 Materialien behielten ihre Hauptphase nach den Versuchen bei.

Für die HTM-Materialien wird als Kriechmechanismus für LWO54 die Kationen-gestützte Diffusion mit einer gemeinsamen Wanderung von La^{3+}/W^{6+} entlang der Korngrenzen / durch die Gitter vorgeschlagen. ST·F100x, LWO54 und NWO55 sind vielversprechende Membranmaterialien in Bezug auf den Kriechwiderstand.

Für dichte und poröse foliengegossene LWO54-Proben wurden die Elastizitäts- und Brucheigenschaften ermittelt. Der über Härteeindruck-, Doppelringtest- und Impulserregungsversuchen ermittelte Elastizitätsmodul verringert sich um ca. 20 % bei einer Änderung der Temperatur von Raumtemperatur bis 1000°C in Luft und Ar / 4% H_2 Atmosphäre. Die Festigkeit von dichten Materialien nimmt bei einer Erhöhung der Temperatur auf 1000°C in Luftatmosphäre um ~ 30% ab, während sie bei Raumtemperatur um den Faktor ~ 2 bei homogenen Mikrostrukturen ansteigt. Nachfolgende fraktographische Analysen zeigen Agglomerate von großen unregelmäßigen Poren als Bruchquelle. Bei den porösen LWO54-Materialien nimmt die Festigkeit mit der Porosität und bei Vorhandensein der sekundären Phase $La_6W_2O_{15}$ ab. Mikro-mechanische Eigenschaften bei Raumtemperatur werden durch Vickers-Härteeindrucktests ermittelt.

Acknowledgements

This work was carried out in Institute of Energy and Climate Research, Microstructures and Properties (IEK-2), Forschungszentrum Jülich GmbH during the years 2012-2015.

I would like to express my special appreciation and thanks to the people who helped making this thesis possible.

First and foremost I would like to thank my Doktorvater Univ.-Prof. Dr.-Ing. L. Singheiser for providing excellent conditions during my PhD study at the IEK-2 Institute. I would also like to thank the members of my committee Univ.-Prof. Dr.-Ing. T. Beck who also gave me the opportunity to start this PhD and Univ. –Prof. Dr. – Ing. R. Kneer.

I would also like to thank my supervisor Dr. J. Malzbender for his valuable scientific support and guidance during my PhD.

Financial support from the Helmholtz Association of German Research Centers (Initiative and Networking Fund) through the Portfolio-topic MEM-BRAIN is gratefully acknowledged.

Furthermore, I would like to thank all partners from the Portfolio Membrain project for the sample supply as well as an encouraging and motivating project work, especially Dr. W.A. Meulenberg for the project guidance, and Dr. S. Baumann, Prof Dr. H.J.M. Bouwmeester, S.F.P. ten Donkelaar and Dr. J.M. Serra for their excellent collaboration. Special thanks to the colleagues Clemens Krautgasser and Dr. R. Bermejo, from Montan University, Leoben, Austria for all their help regarding the ball-on-3-balls testing method.

T. Osipova, J. Mönch and R. Küppers are kindly acknowledged for their excellent experimental support, Dr. E. Wessel and Dr. D. Grüner for SEM studies, M. Zigner for XRD studies, J. Bartsch, and V. Gutzeit for their assistance in metallographic preparations, and Mrs. M. Felden and P. Joecken for their technical support.

The members of my group have contributed immensely to my personal and professional time in Forschungszentrum Jülich GmbH. During my years in Forschungszentrum Jülich GmbH I had the chance to meet wonderful people and motivating scientists who became my friends and part of my life. Many thanks to my colleagues and friends from the working as well as the membrane group for fruitful discussions, valuable help and priceless motivation that made easier the scientific life: Dr. G. Pećanac, Dr. B. Rutkowski, Dr. M. Lipińska-Chwałek, Dr. O. Tokariev, Dr. A. Böhm, Dr. B.X Huang, Dr. V. Vasechko, JP. Wei and Y. Zou, Dr. C. Chatzicharalampous, Dr. M. Balaguer-Ramírez, M. Ramasamy, Dr. E. Forster, Dr. M. Benito - Abascal, Dr. S. Stille, R. Silva, Dr. B. Wendland.

Last but not least I want to thank my family for raising me with a love for science and faithfully support and encouraged me all these years.

1 Contents

2 Introduction

The continuous increase of population has led to increased energy demand; therefore, the CO_2 emissions have become the major contributor to global warming. Despite the development of renewable energies in the last decades, the lack of large scale energy storage will ultimately maintain the fossil fuel a main energy source. Developing Carbon Capture Technology is an intermediate step before the complete sustainable energy supply is realized. In that case CO_2 is separated from other gases before it is released into the air, and can be further utilized [1,2].

Three main technological implementations for carbon capture based on inorganic membranes are briefly described below [3,4,5,6].

Post-combustion: CO_2 is separated from the exhaust gases after the combustion process via membrane technology. The decisive advantage of post-combustion over other capture methods is that it can be easily retrofitted onto existing power plants.

Pre-combustion: In this process, the fuel is converted into a gaseous mix of CO_2 and H_2 as illustrated in Figure 2-1. Prior to combustion, the fuel is partially oxidized in pure oxygen and hence, CO is obtained as an intermediate product. The partially oxidized fuel reacts with water vapor (CO-shift reaction) to form a mixture of H_2 and CO_2. Finally, H_2 is extracted using either proton conducting dense ceramic membranes or polymeric H_2 or CO_2 selective membranes. This extracted H_2 is used as fuel, while CO_2 is captured and stored. The concentration of CO_2 in this mixture ranges from 15 - 50%. In comparison to the post-combustion process, the pre-combustion process is more efficient, since the gas separation takes place at high pressure and high concentrated CO_2 gas mixture. But the fuel conversion steps required for pre-combustion are more complex than those in post-combustion, making the technology more difficult to apply to existing power plants at increased capital cost [7].

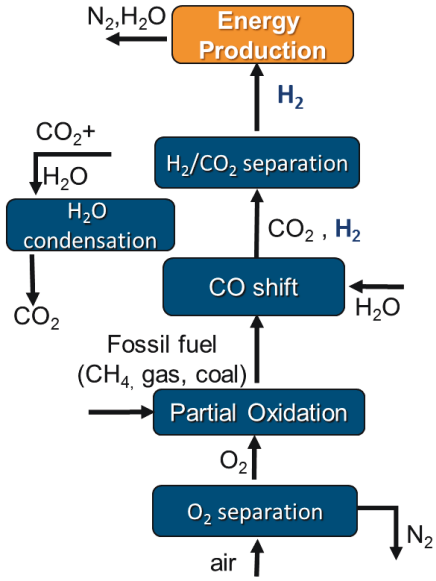

Figure 2-1 The pre-combustion carbon capture process.

OXYFUEL: This process uses oxygen rather than air for combustion of fuel. Therefore, the produced exhaust gas mainly consists of CO_2 and water vapor that can be easily removed by condensation. The CO_2 concentration in this process is more than 80% per volume. Mixed ionic electronic conducting (MIEC) dense ceramic membranes are applied for the O_2/N_2 separation. OXYFUEL combustion represents an opportunity to improve the economics of CO_2 capture since it exhibits small efficiency loss (5% points) in the power plant compared to conventional cryogenic process (8.6 %) [7,8,9,10]. The principle of OXYFUEL process is schematically illustrated in Figure 2-2:

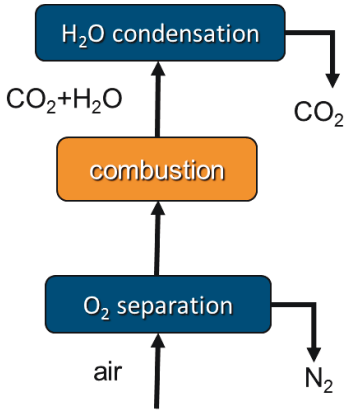

Figure 2-2 The OXYFUEL carbon capture process.

Gas separation processes require membranes with high selectivity, permeability and mechanical integrity as key properties. Such membrane materials allow the preferential passage of hydrogen (Hydrogen transport membranes HTM) or oxygen (Oxygen transport membranes OTM) in the form of ions. The advantage of both, ceramic oxygen/proton conducting membranes is that the oxygen/hydrogen separation is driven by the chemical potential gradient across the membrane due to the ambi-polar diffusion of oxygen/protons and electrons at high temperatures [11]. Hence the application of an electrical field or external current is not required.

Other potential applications of mixed ionic electron conducting ceramic materials are solid oxide fuel cells, gasification systems of fossil fuel for energy generation (IGCC), petrochemical products, gas-to-liquid (GTL) processes, where natural gas is converted to liquid hydrocarbons as well as the generation of pure oxygen itself [12,13].

The present work was carried out within the framework of the “Portfolio Membrain Project” supported by the Helmholtz Association. Due to their favorable permeation properties, several promising membrane materials were investigated: $Ba_{0.5}Sr_{0.5}(Co_{0.8}Fe_{0.2})_{1-x}Zr_xO_{3-\delta}$ with x = 0.01, 0.03, 0.05, 0.1 (BSCF·Z100x) and $SrTi_{(1-x)}Fe_xO_{3-\delta}$ with x = 0.03, 0.05, 0.07 (ST·F100x) were chosen as candidates for oxygen transport membrane, while $La_{5.4}WO_{12-\delta}$ (LWO54) and $Nd_{5.5}WO_{12-\delta}$ were selected as hydrogen transport membrane.

During operation, these materials can be exposed to mechanical stresses induced by pressure gradients, chemical expansion and differences in thermal expansion with respect to sealant and housing materials. These operation conditions are different depending on the process. Oxygen transport membranes work under either oxidizing or reducing conditions (e.g. air versus methane) or oxidizing conditions on both sides of the membrane (OXYFUEL Process). The hydrogen transport membranes usually work under reducing conditions on both sides (Pre-Combustion Process). In addition, both types of membranes operate at high temperature (namely 850 °C for OXYFUEL and 600-800 °C for the pre-combustion process) [14]. Besides the chemical stability, the mechanical properties are thus very important, and therefore, their extended characterization is necessary. This characterization includes elastic and fracture tests and, due to the envisaged operation at elevated temperatures, the extensive study of creep behavior.

With respect to the membrane materials, mostly perovskites are used due to their favorable mixed conductivity. In case of OTM, where mixed ionic and electronic conductivity is required, the perovskite with excellent oxygen permeability is $Ba_{0.5}Sr_{0.5}Co_{0.8}Fe_{0.2}O_{3-\delta}$ (BSCF5582) [15]. However, this material suffers from a crystal phase transition at operation temperatures that depletes the oxygen transport through the lattice. Addition of other dopants, like ZrO_2 may stabilize the crystalline phase, which usually comes along with a drop in the permeation. Therefore, a compromise between stability and permeability should be accomplished.

The current study mainly concentrates on the thermo-mechanical characterization of the selected materials mentioned above. Hence, the effect of Zr doping for BSCF·Z100x perovskite materials were initially investigated. The Zr doping was believed to stabilize the structure at the phase transition temperature range of the high flux material BSCF5582. On the other hand, based on Fe doping of the stable $SrTiO_3$ in order to increase its permeability, the STF·100x class of materials was investigated as an alternative solution to BSCF5582. Both materials development routes aimed for chemically stable high flux materials. Since BSCF·Z100x and ST·F100x materials were still in an initial development stage, only small number of specimens for creep testing could be made available. Hence, this part of the work focused on the determination of the creep mechanism and its correlation to the microstructural properties of the materials, considering the requirements of the

OXYFUEL process. The creep behavior has been determined based on compressive tests.

Regarding hydrogen transport membranes for the Pre-Combustion capture technology, the investigations were focused on the mechanical behavior of $La_{5.4}WO_{12-\delta}$ (LWO54), a novel fluorite-structured material that shows good ambi-polar protonic-electronic conductivity. Dense and porous LWO54 have been characterized. Whereas the dense material was investigated to gain basic understanding of the materials behavior, the porous LWO54 was characterized to gain understanding of the relationship between mechanical properties, manufacturing process and optimization possibilities.

More specifically, regarding the dense material, elastic and fracture properties as well as the compressive creep behavior and elastic and fracture properties were characterized for LWO54. Tests were performed at room temperature as well as in operation related temperatures. In addition, the creep behavior of the alternative proton conductor $Nd_{5.5}WO_{12-\delta}$ was investigated.

The planar asymmetric membrane design concept should be applied for HTM. In this case the substrate will have to provide the mechanical stability. For the substrate, a porosity from 20 to 40 % is required in order to enable the gas permeation. Since porosity leads to reduced mechanical properties, a compromise should be achieved for the porosity regarding permeation and mechanical properties. Therefore, porous tape casted material with different porosity range related to operation was prepared and tested with ball-on-3-balls method. Literature on the mechanical properties of these materials is limited; hence, the results of the current study will be of high interest for materials and system design.

3 Fundamentals

A gas transport membrane can be described as a barrier between two enclosures which preferentially allows ions to permeate using pressure or an electrical potential gradient as a driving force [16]. The working principle of dense ceramic membranes for oxygen and hydrogen separation is described below and the theoretical basis for the transport properties in dense oxides regarding flux of the gases is addressed. In this respect, the materials that exhibit the required highest fluxes are also discussed in detail.

3.1 Oxygen Transport Membranes

Figure 3-1 depicts the working principle of oxygen permeation through a MIEC membrane. The driving force for oxygen transport is the gradient of oxygen partial pressure existing across the membrane. Permeation takes place from the high oxygen partial pressure side $pO_{2\ (1)}$ (feed side) to the low oxygen partial pressure side $pO_{2\ (2)}$ (permeate or sweep gas side). It is divided into three zones: 1) an interfacial zone on the high partial pressure, 2) a central bulk zone and 3) an interfacial zone on the low oxygen partial pressure or sweep gas side. Since the MIEC membrane is dense and gas-tight, the direct passage of oxygen molecules is not possible, but oxygen migrates through the membrane selectively in the form of ions O^{2-} from the $pO_{2\ (1)}$ to the $pO_{2\ (2)}$ part. The overall charge neutrality is maintained by a counterbalancing flux of electrons as shown in Figure 3-2. Thus, the electronic conductivity itself creates a short circuit and the air separation through this process leads to high purity oxygen. After O^{2-} cations are transported to the low pressure side, they recombine to form molecules that are released into the permeate stream [16]. The oxygen transport in the crystal lattice at such membranes is described with the Kröger - Vink notation as follow:

$$\frac{1}{2}O_2 + V_O^{\cdot\cdot} + 2e' = O_O^x \qquad \text{Equation 3-1}$$

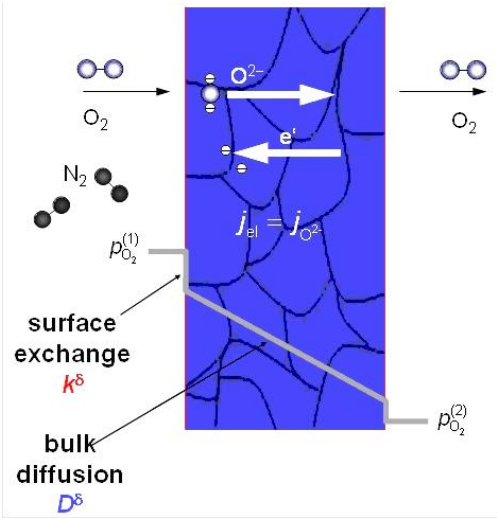

Figure 3-1 Operation principle of a MIEC membrane for oxygen separation [17].

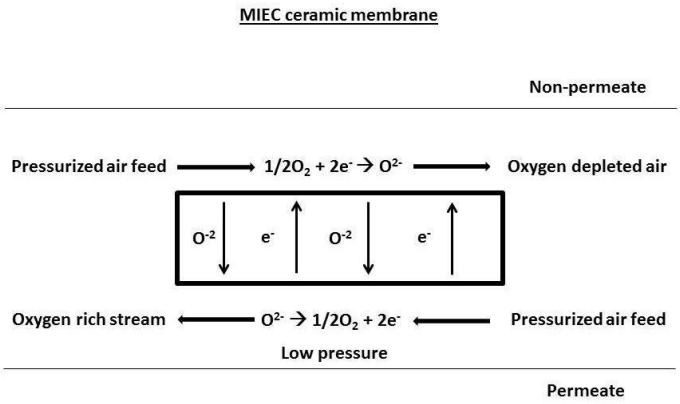

Figure 3-2 Dense ceramic membrane based on a mixed conducting mechanism [12].

The oxygen transport through a MIEC membrane can be described by Wagner's theory of diffusion in solid oxides [12,18,19]:

$$jO_2 = \frac{RT}{16\,F^2 L}\int_{p_{O_2}^2}^{p_{O_2}^1} \sigma_{amp}\, d\ln\left(p_{O_2}\right) \qquad \text{Equation 3-2}$$

With $\sigma_{amp} = \frac{\sigma_{el}\cdot\sigma_{ion}}{\sigma_{el}+\sigma_{ion}}$ Equation 3-3

Where jO_2 is the oxygen permeation flux in mol·m^{-2}·s^{-1}, R *the* universal gas constant, T the temperature, F the Faraday constant, *L* the membrane thickness, σ_{amp} the ambi-polar conductivity and the limits of integration $p_{O_2}^1$ and $p_{O_2}^2$are the oxygen partial pressures at the gas-phase boundaries.

From Wagner's equation it appears that the oxygen permeation flux depends on the process parameters (*T*, $p_{O_2}^1$ and $p_{O_2}^2$), the membrane architecture (*L*) and the material properties (σ_{amp}). *T*, $p_{O_2}^1$ and $p_{O_2}^2$ will be fixed by the process itself (chemical reaction, OXYFUEL, etc) [20,21]. A further increase in permeation can be achieved by membrane architecture design.

However, the oxygen flux increases only up to a characteristic thickness L_c, and further reduction does not lead to any further increase since surface exchange reactions dominate the transport. The rate of oxygen flux is thus controlled by two factors: i) solid state diffusion within the membrane and ii) interfacial oxygen exchange on both sides of the membrane. Bouwmeester et al. [16], introduced this limit into the Wagner equation yielding:

$$jO_2 = \frac{1}{\left(1+\frac{2L_c}{L}\right)} \frac{RT}{16\,F^2 L} \int_{p_{O_2}^2}^{p_{O_2}^1} \sigma_{amp}\, dln\left(p_{O_2}\right) \qquad \text{Equation 3-4}$$

Where $L_C = \frac{D}{k}$, D is the oxygen diffusion coefficient and k the surface exchange coefficient. Typical values for Lc were determined to be in the range from µm to cm, depending on material and environmental parameters [16]. For BSCF the membrane thickness should be < 100 µm, hence, the aim is a thin membrane layer supported by a porous substrate that provides the mechanical strength [15].

Finally, the permeation rates can be further improved by increasing the σ_{amp} of the membrane material. However, there is a tradeoff between stability and transport properties for the membrane materials. Among ceramic oxide membranes with mixed ionic electronic conducting characteristics, perovskite-type and fluorite-type are the best compounds in terms of oxygen permeation properties [22,23,24]. State of the art materials used as MIEC membranes are the perovskites, with the chemical formula ABO_3. The ideal perovskite structure is represented in Figure 3-3 where A cations are

located at the corners of the tube and the B cations at the center, while the oxygen anions are positioned in the center of the cube edges.

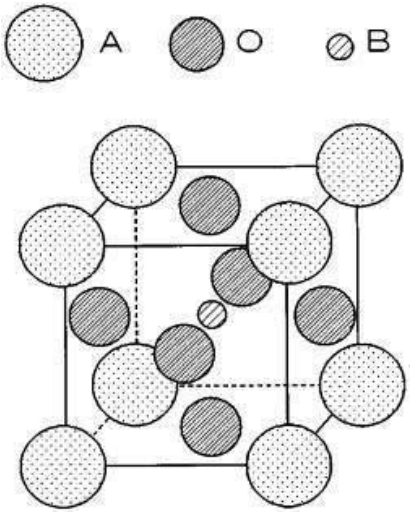

Figure 3-3 Perovskite structure ABO_3 [16]

The ideal perovskite structure illustrated in Figure 3-3 has no capability of conducting oxide ions. For diffusion or conduction to occur, defects have to be introduced in the structure via nonstoichiometry [12]. Therefore, doping strategies have been widely adapted to improve the permeation of the perovskite oxides. The perovskite structure is able to tolerate cations with different valence and ionic radii to achieve high concentrations of oxygen vacancies and ionic conductivity. Since these modifications affect the crystal stability, the tolerance limits of the cation's radii in A and B sites of the perovskites are calculated by the Goldschmidt factor:

$$t = \frac{r_A + r_0}{\sqrt{2}(r_B + r_0)}$$ Equation 3-5

Where r_A, r_B and r_0 are the radii of the respective ions. Nominally, the perovskite structure is expected to be stable for $0.75 < t < 1.0$. If the distortion exceeds these limits, other crystal symmetries appear like orthorhombic and rhombohedral, while $t \sim 1$ corresponds to ideal cubic perovskite lattice [25].

The concentration of defects in non-stoichiometric oxides is a function of temperature and pressure of their components, mainly oxygen in the oxides. The dopant choice

and levels have a significant effect on several parameters such as lattice structure, electrical conductivity, sintering behavior and the oxygen permeation flux [26, 27, 28, 29]. The stability of the perovskite structure is generally improved by B-site doping with a more stable cation to produce $AB_{1-x}M_xO_{3-\delta}$ where δ is denoted by the amount of vacancies or defects. In the formula $AB_{1-x}M_xO_{3-\delta}$, *A* = Ca, Sr or Ba; *B* element = Ce, Tb, Zr or Tl; and *M* = Ti, Tm, Cr, Mn, Co, Ni, Cu, Al, Ga, Y, Yb, In or Sn. x is less than the upper limit of solid solution formation range (normally less than 0.2) and δ is the oxygen deficiency per unit cell. In general, the higher the amount of vacancies, the higher the oxygen flux [30,31,32,33] The perovskite structure is also formed with substitutions for either A or B cations or of both A and B cations in order to produce $A_xA'_{1-x}B_yB'_{1-y}O_{3-\delta}$.

3.2 Materials

The criteria for the selection of a material as a dense ceramic membrane are summarized as follows [16,34]:

a) high mixed ambipolar conductivity (ionic / electronic for OTM, protonic / electronic for HTM)
b) high catalytic activity regarding oxygen reduction
c) chemical and structural integrity in the application relevant temperature and oxygen partial pressure range, as well as the respective working atmosphere
d) compatibility with the other cell components (no chemical interaction & same thermal expansion coefficient TEC)
e) low volatility at operating temperatures
f) capability to be fabricated as thin films
g) mechanical integrity
h) low cost of material and fabrication

It is obviously difficult to fulfill all these requirements. Nevertheless, the materials in the following sections were chosen for investigation in the frame of the project where their development and properties are introduced.

3.2.1 BSCF·Z100x

The pioneer work of Teraoka et al. [35,36,37] introduced a very challenging research area for the development of perovskites as high conducting oxygen permeation

membranes. Teraoka et al. investigated the influence of A and B site substitution on oxygen permeation through $La_{0.6}A_{0.4}Co_{0.8}Fe_{0.2}O_{3-\delta}$ (A = La, Na, Ca, Sr, Ba) and $La_{0.6}Sr_{0.4}Co_{0.8}B_{0.2}O_{3-\delta}$ (B = Fe, Co, Ni, Cu). It was shown that among the family of $La_{1-x}Sr_xCo_{1-y}Fe_yO_{3-\delta}$, the $SrCo_{0.8}Fe_{0.2}O_{3-\delta}$ composition possesses the highest permeation at 850°C due to the high concentration of oxygen vacancies in the lattice caused by A-site substitution.

However, it was reported that this perovskite compound is rather unstable and cannot maintain the cubic perovskite structure [38]. In case of original structure $SrCoO_{3-\delta}$, a significant drop in permeability was observed due to cubic-to-brownmillerite phase transformation below 1000 °C [39]. To overcome this problem, partial substitution of Co and Fe was performed to form the material $SrCo_{0.8}Fe_{0.2}O_{3-\delta}$. It was found that the B-site doping by 20% Fe improved the perovskite phase stability to 790°C [40]. Shao et al. [41] introduced $Ba_{0.5}Sr_{0.5}Co_{0.8}Fe_{0.2}O_{3-\delta}$ (BSCF5582) material where Sr^{2+} was substituted by Ba^{2+}, with same valence state but higher ionic radii as the most promising composition for high oxygen permeation rates.

Based on these studies, the perovskite-type oxide BSCF5582 has been intensively investigated for its potential use as OTM. Thin film asymmetric (supported) membranes prepared from BSCF5582 have been found to exhibit unprecedented high oxygen fluxes [15,42]. However, the material suffered from stability issues related to its decomposition at moderate temperatures (below ~ 850 °C) [43] that not only affect the permeation properties [42,44], but also the mechanical stability [45]. Overall, these stability issues could have detrimental effects on the long-term reliability and performance of the membrane [46,47].

The phase instability of BSCF5582 below the critical temperature of ~850 °C as well as its detrimental effect on oxygen transport properties have been studied by different researchers [48,49,50,51]. In general, the results confirm that grain boundaries and/or imperfections, such as cobalt oxide precipitates, serve as sites for nucleation and growth of secondary phases. Using transmission electron microscopy (TEM) techniques, Mueller et al. [51] observed decomposition of BSCF into hexagonal 2H-$Ba_{0.5+x}Sr_{0.5-x}CoO_{3-\delta}$, and a (compared to pure BSCF) Ba- and Co-depleted cubic perovskite-type phase $Ba_{0.5-x}Sr_{0.5+x}Co_{0.6}Fe_{0.4}O_{3-\delta}$. Efimov et al. [52] suggested hexagonal 2H-$Ba_{0.6}Sr_{0.4}CoO_{3-\delta}$ and a lamellar, non-cubic phase

$Ba_{1-x}Sr_xCo_{2-y}Fe_yO_{5-\delta}$ as main decomposition products. Extensive investigations by Müller et al. [53] identified the latter phase as an intergrowth compound, $Ba_{m+1}Co_mO_{3m+3}$ (Co_8O_8), m ≥ 2 (denoted by BCO), consisting of CdI_2-type CoO_2 and perovskite layers. Regions with a plate-like morphology were identified consisting of a random arrangement of cubic (with a small departure of the original BSCF composition), hexagonal, and BCO-type phases as illustrated in Figure 3-4.

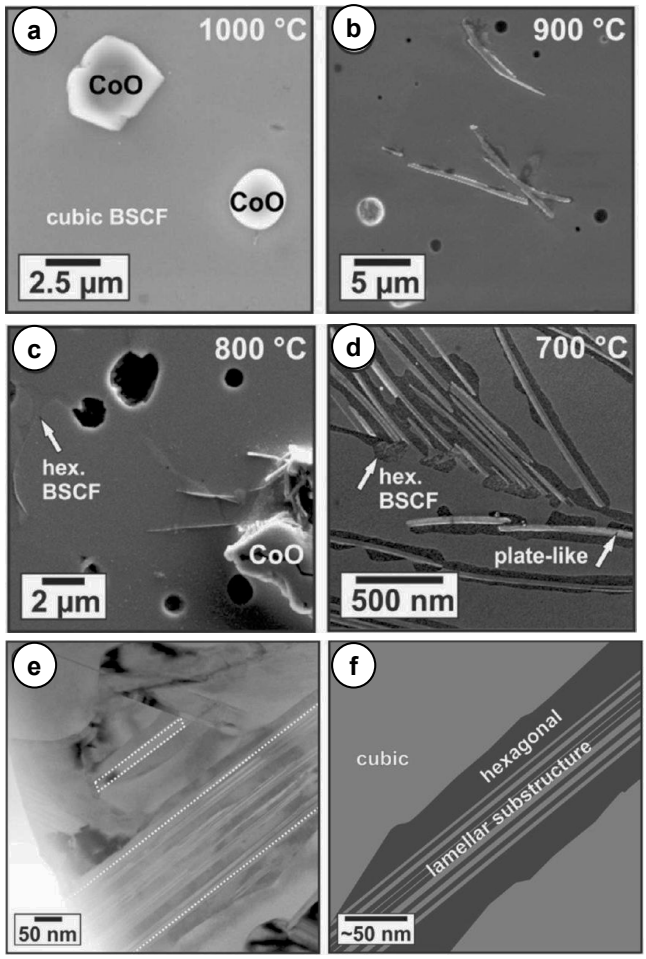

Figure 3-4 a-d) SEM Images that illustrate the formation of the secondary phases in BSCF after annealing for 100 hours in ambient air , 1000, 900, 800, 700°C respectively e) bright-field TEM image of a sample after annealing at 700 °C, f) scheme of the microstructure of plate-like regions [53].

Another issue for BSCF is its chemical instability towards CO_2 containing environments which leads to decrease of oxygen permeation [54,55,56].

Several groups have demonstrated that the undesired phase decomposition of BSCF below ~ 850 - 900 °C can be avoided by partial substitution of (Co, Fe) by redox-stable cations such as Nb, Y, and Zr, albeit at the expense of reduced oxygen flux [57,58,59,60,61]. The reason behind these substitutions is Goldschmidt's theory on the relative stability of cubic and hexagonal perovskite structures [50], and to avoid an excessive increase in the oxygen stoichiometry. Hence, by keeping the average oxidation state lower and the ionic radii matching the host radii even upon lowering the temperature or increasing the ambient oxygen partial pressure, it is possible to improve the structural stability. Recently, Yakovlev et al. [60], suggested that the introduction of 3 mol% ZrO_2 is sufficient to prevent decomposition of BSCF5582, while $Ba_{0.5}Sr_{0.5}(Co_{0.8}Fe_{0.2})_{0.97}Zr_{0.03}O_{3-\delta}$ possesses similar high permeation rates but improved stability compared to BSCF5582. No sign of performance degradation were found in electrical conductivity data and conductivity relaxation curves recorded at 800 °C, pO_2 of 1 atm over 260 hours [60]. A follow-up study conducted by Ravkina et al. [61] however, demonstrated oxygen permeation fluxes to decline with time for oxygen permeation measurements performed at 750 °C.

Finally, it should be remarked, to emphasize the importance of the main focus of the study, that the effect of the phase transformation on the mechanical performance of the perovskite materials was first reported by Pei et al. [62] who observed two different fracture types in tubular membranes of $SrCo_{0.8}Fe_{0.2}O_{3-\delta}$ during the syngas generation process. The first fracture type took place within the first hour of operation at 800°C as a result of the pO_2 gradient across the membrane, the arising strain due to the lattice mismatch as well as the brownmillerite-perovskite phase transition. The second fracture type was observed after prolonged exposure to reducing environment due to the decomposition of $SrCoO_3$.

3.2.2 ST·F100x

As an alternative option to replace the unstable BSCF, solid solutions of $SrTi_{1-x}Fe_xO_{3-\delta}$ (ST·F100x) were investigated due to their high stability of the strontium titanate host lattice [66]. The oxide materials based on perovskite titanates $ATiO_{3-\delta}$ (A=Ca, Sr, Ba) exhibit advantageous transport properties such as mixed oxygen ionic and electronic conductivity, stability in both reducing and oxidizing environments, a significant protonic conduction in hydrogen-containing atmospheres and a relatively

low chemical expansion [63]. Hence, such perovskite titanates are suitable for high temperature electrochemical applications such as sensors, electrodes of SOFCs, sensors and ceramic membranes for oxygen separation and partial oxidation of hydrocarbons [63].

The almost oxygen impermeable $SrTiO_{3-\delta}$, which has a high chemical stability was doped with Fe to introduce a mixed ionic and electronic conductivity materials class $SrTi_{1-x}Fe_xO_{3-d}$ (ST·F100x) [66]. Studies had shown that the incorporation of lower valence ions like Co and Fe into the B sublattice of ABO_3 perovskite titanate structure increases the oxygen vacancy concentration and hence the ionic conductivity [63,64], while the presence of Ti in the B site enhances the thermodynamic and dimensional stability under high oxygen chemical potential gradients [65]. Regarding their potential application as oxygen transport membrane material, the $SrTi_{1-x}Fe_xO_{3-d}$ was investigated by Schulze-Küppers et al [66]. Focusing on the membrane structural and functional properties such as sintering behavior, oxygen permeation rates, chemical/ thermal expansion as well as the stability in CO_2 and Ar / 4% H_2 environments. They concluded that a good compromise between structural and functional properties was obtained for compositions up to ST·F35. These compositions yielded higher oxygen permeation comparing to the standard material $La_{0.6}Sr_{0.4}Co_{0.2}Fe_{0.8}O_{3-\delta}$ (LSCF). Moreover, the stability of ST·F35 was found to be improved in comparison to LSCF. Additionally, the thermal expansion coefficients reported for compositions with low Fe content, up to ST·F35, (11.3-16.2x10^{-6} K^{-1}) much very well with the ones of the adjacent metallic components such as austenitic stainless steels (16-18x10^{-6} K^{-1}) and Ni-based alloys (12-16 10^{-6} K^{-1}) [66]. It is very important that the expansion behavior of the membrane and the adjacent materials is similar so that thermally induced stresses are avoided. Therefore, it seems that the compositions up to ST·F35 fulfill the membrane materials requirements.

3.3 Hydrogen Transport Membranes

Hydrogen has a high potential for usage in future energy systems. Hence, proton conducting materials have attracted increasing interest [78]. One of the possible applications for mixed proton-electron conducting membrane materials is hydrogen separation at elevated temperature in fossil fuel fired power plants that engage gasification and pre-combustion strategies [67,68]. Some other potential applications

include electrolytes in hydrogen sensors, electrolytes in hydrogen fuel cells, solid electrolytes in a steam electrolyzer and hydrogen pump for hydrogen extraction from various gas mixtures [69,70,71,72].

The working principle of a hydrogen transport membrane is shown in the following figure:

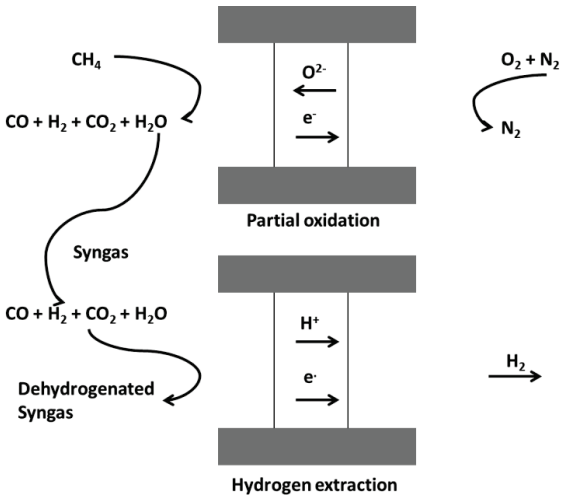

Figure 3-5 Schematic representation of a MIEC for oxygen separation with direct reforming of methane, followed by hydrogen extraction from the resulting syngas with the use of proton-electron (MPEC). Products are pure H_2 and synthesis gas with reduced hydrogen content [73].

In this case, the H_2 separation is accomplished similar to OTM in a nongalvanic mode, H^+ ions are transported through the membrane, while the counter flow of electrons eliminates the need for an external power supply [72]. The hydrogen partial pressure gradient is the driving force of the flux. Therefore, the membrane will work in a hydrostatic pressure difference of hydrogen and only under reducing conditions for both sides [109].

The nature of the mixed conducting oxides can be defined by the transport equations for each material as fully described by the chemical defect model for the dissolution of protons for all possible cases of charge carriers in acceptor-doped materials by Fontaine et al. [74] This work focuses on candidate materials for hydrogen gas separation membranes in fossil-fuel power plants for the separation of H_2 from CO_2, hence ambipolar proton and n-type electronic conductivity is the materials' prerequisite for enhanced hydrogen permeability [78]. Hydrogen dissolves in the

oxide in equilibrium with a source gas like hydrogen or water vapor, depending on the dominant conducting species in the intrinsically non-proton conducting state. Hydrogen is the donor that is fully ionized under most practical conditions as the electron potential is expected to be low. Thus, the simplest possible reaction that describes dissolution of protons is:

$$H_2(g) + 2O_O^x = 2OH_O^{\cdot} + 2e' \qquad \text{Equation 3-6}$$

$$O_O^x + \frac{1}{2}H_2 \Leftrightarrow OH_O^{\cdot} + e' \qquad \text{Equation 3-7}$$

As the proton defect is effectively positive, its concentration is enhanced by acceptor doping. Most scientific studies and application-oriented work on proton-conducting oxides have been done on acceptor-doped oxides. In such oxides the acceptors are compensated by oxygen vacancies in a dry state, so that they are oxygen ion conductors. When equilibrated in water vapor, the oxide dissolves protons and fills the vacancies according to the following equation:

$$H_2O\ (g) + v_O^{\cdot\cdot} + O_O^x = 2OH_O^{\cdot} \qquad \text{Equation 3-8}$$

Using the equilibrium expression between vacancies and water vapor to form protons, the concentration of protons and their pH_2O dependency can be estimated. The proton transport in oxides has been demonstrated to take place by the free proton transport mechanism or proton migration (Grotthuss type) mechanism [75,76,77]. In this mechanism, the protons are considered to migrate through jumps between stationary oxygen ions. The enthalpy of the hydration reaction varies considerably when correlated to materials properties.

Theoretical models for H_2 permeation through proton conducting ceramic membranes can be used to understand the underlying phenomena as well as to support the design and optimizing processes of utilizing these membranes. Similar to oxygen transport, the Wagner equation is the starting point of describing the H_2 flux assuming that the transport number of oxygen ions t_O is zero [78]:

$$j_{H_2} = \frac{1}{2L}\frac{RT}{F^2}\int_{P_{H_2}}^{P_{H_2}''} t_{H^+} t_e d\ln P_{H_2}$$ Equation 3-9

Here the charge carriers include protons (H^+) and electrons (e^-). It is assumed that the H_2 dissociation rate at the surface of the membranes is much higher than the bulk diffusivity of the charge carriers.

Similar to the OTM, the Wagner equation emphasizes for HTM that parameters such as temperature, membrane thickness and oxygen partial pressure play a significant role in the transport analysis and membrane design to optimize the H_2 flux [78]. For the effect of surface exchange and the criteria for the selection of a material as a dense ceramic membrane see also chapter 3.1.

The prerequisite for ceramic proton conductors is the high ambipolar proton-electron conductivity. In some cases, the improvement of low electron conductivity that limits the H_2 flux of the proton-conducting ceramic membrane to a sustainable level is a remaining challenge [79]. Other limiting factors for the sustainability of the membrane are the long term chemical stability under the presence of various gases such as CO_2, H_2O and SO_3 and also the mechanical integrity [78,80].

3.4 Materials

In the following section a literature overview of ceramic proton- electron conducting materials is presented. It is evident from the information given in the previous sections that the requirements to be fulfilled by the membrane candidate material are quite challenging and severe. In the following sections, the potential HTM candidate materials that exhibit the desired type of mixed conductivity (proton- n-type electron) are introduced and compared.

3.4.1 Perovskite-type oxides

Several perovskite type oxides have been identified to have good characteristics as proton conductors. The first proton conducting material $SrCe_{0.95}Yb_{0.05}O_{3-\delta}$ has been reported by Iwahara [72]. Later, several other perovskite materials have been studied such as doped $BaCeO_3$ [81], $BaZrO_3$ [82,83], $BPrO_3$ [84], $SrZrO_3$, $CaZrO_3$ [85,86,87] and $SrTiO_3$ [88].

The proton conductivities of these perovskites in a hydrogen atmosphere are of the order of 10^{-3}-10^{-2} S cm^{-1} at 600 - 1000°C and can be further improved by appropriate doping [89,90]. $BaCeO_3$ based oxides show the highest conductivity, but oxygen ions also contribute to the conductivity with increasing temperature, resulting in a decreasing transport number of protons [91].

The perovskite materials $SrCeO_3$ and $BaCeO_3$ have high proton conductivities due to the basic nature of the A- and B-site cations, but this makes them vulnerable to the attack of acidic gases such as CO_2, H_2O and SO_3. They quickly form carbonates or sulfur-containing compounds once exposed to carbon- or sulfur- containing gas streams that further lead to deterioration of their conductivity and also to an overall loss of mechanical strength and efficiency. The zirconate based oxides such as $SrZrO_3$ or $CaZrO_3$ show good chemical stability and good mechanical strength. They are more stable against CO_2 compared to cerates [92], but the conductivity of zirconates is lower [93] due to the high grain boundary resistances [94]. The perovskite with the highest reported conductivity 1- 5 × 10^{-3} S cm^{-1} at 600°C and high CO_2 resistivity, is the acceptor-doped $LaScO_3$ [95].

3.4.2 Non-perovskite-type oxides

In order to overcome the stability problems in reducing atmospheres, investigations have also been focused on novel materials with other structures than perovskites. One class of doped non-perovskite structured oxides that combine proton conductivity with CO_2 stability are the rare earth sesquioxides Ln_2O_3 [96,97,98]. Terbium sesquioxide Tb_2O_3 has also been reported to exhibit both electronic (p-type) and proton conductivity in hydrogen atmosphere at high temperatures (proton conductivity 5 × 10^{-5} S cm^{-1} at 900 °C) [109].

Oxides with fluorite structures such as Y_2O_3 and CeO_2 exhibit proton conductivity in H_2 / H_2O atmosphere and at high temperatures [99,100]. Although the hydrogen permeability of those materials is rather low, their chemical and thermodynamic stabilities are very good. By adapting a proper dopant strategy, their hydrogen permeability can be greatly improved [101]. Other non-perovskite oxides that have been reported to exhibit rather low proton conductivities at high temperature are the pyrochlores $Ln_2Zr_2O_7$ and $LaPO_4$ [102,103].

Recent developments led to a novel class of ceramic materials, lanthanide tungstate compounds $Ln_xWO_{3+1.5x}$ x≈6 (LnWO) with ordered defect fluorite structure or disordered pyrochlore structure [104,105]. These structures exhibit sufficient electron-proton conductivity in hydrogen containing atmospheres at high temperatures [106,107] and acceptable stability in CO_2 containing atmospheres [108]. Norby et al. stated that the total conductivity derived from both, protonic and electronic conductivities must be at least 0.1 S cm^{-1}, which however, also depends on the membrane thickness and other factors [109]. These two properties make LnWO a class of promising candidate materials for hydrogen separation membranes, in catalytic membrane reactors for selective hydrocarbon conversion.

More specifically, an early study by Yoshimura et al. [110] reported the electrical conductivities in the temperature range 500 to 1500 °C of solid solutions for the system CeO_2-La_6WO_{12}. It exhibits predominant electronic conductivity at high temperatures and ionic conductivity at low temperatures. Proton conductivity was not considered in this study, but later Shimura et al. [111] demonstrated that $La_xWO_{3+1.5x}$ (x~6) (LWO) exhibits considerable proton conductivity under hydrogen containing atmospheres. They have also shown that the LWO material with stoichiometry of $La_{5.8}WO_{11.7}$ demonstrates an ionic conductivity of about 5 × 10^{-3} S·cm^{-1} at 900°C in wet H_2 with limited p-type contribution, but enhanced n-type conductivity resulting from W^{6+} reduction. Mixed proton-electron conductivity of both, stoichiometric and partially substituted LnWO where Ln = La, Nd, Gd, Er was further demonstrated [112]. A comparison with $SrCeO_3$ doped with 5% Yb regarding the ambipolar conductivities led to the conclusion that LWO was a promising candidate for membrane applications [113]. Several other research groups have also studied the structural model of LWO, its synthesis optimization for deriving single phase material and its transport properties [108,116,120]. Mixed protonic-electronic conductivity was experimentally determined by Hausgraud et al. [107,113] for LnWO (Ln=Nd, La, Gd, Er) materials yielding values similar to the state-of-the-art 5% Yb doped $SrCeO_3$ thus, establishing LnWO class as promising candidate membrane materials.

Two phase diagrams have been published for the system La_2O_3-WO_3 since 1970's. In the first one by Ivanova et al. [114] the La_6WO_{12} phase which exists up to 1250°C, has been reported while Yoshimura et al. [115] stated that $La_{10}W_2O_{21}$ exists up to ~1740°C along with the La_6WO_{12} phase which is formed from ~1740°C up to 1960°C

(Figure 3-6). Nevertheless, single phase material has been successfully synthesized with several methods by effectively controlling the deviation from the equilibrium by W-over-stoichiometry with nominal compositional ratios for obtaining single phase material varying between $5.2 \leq x \leq 5.7$ after firing at 1500 °C [116,117,118]. But if the equilibrium shifts to the W-rich region, the formation of the secondary phase $La_6W_2O_{15}$ takes place. In case of equilibrium shift to the La-rich region, segregation of La_2O_3 is observed. Both secondary phases have been proven to be critical for membrane operation since La_2O_3 is highly hygroscopic and forms $La(OH)_3$ when exposed to moisture. $La_6W_2O_{15}$ structural transformations at ~ 630 °C and ~ 930 °C [119] accompanied by pronounced thermal expansion anisotropy of the unit cell, leading to crack formation due to induced tension stresses and thus disintegration of the membrane [120]. Therefore, synthesis of single phase material is of high importance for the effective membrane fabrication.

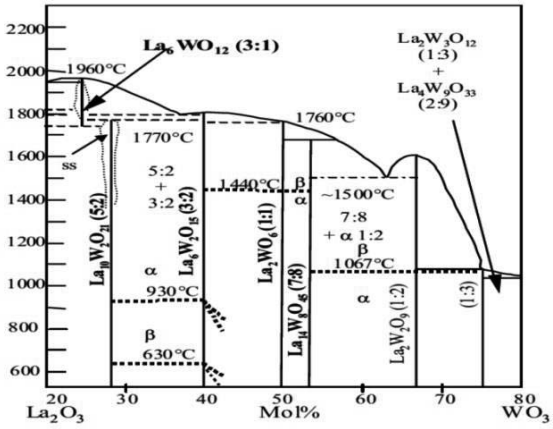

Figure 3-6 Phase diagram of La_2O_3 – WO_3 after [115].

The crystal structure of $La_{6-x}WO_{12-y}$ ($y=1.5x+\delta$) according to Sherb et al. [121] is represented in Figure 3-7:

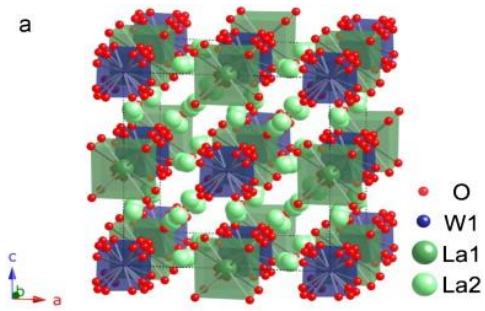

Figure 3-7 Model for the average crystal structure for $La_{5.5}WO_{11.1-\delta}$ in space group $Fm\bar{3}m$ with split oxygen and split lanthanum sites refined from high-resolution synchrotron X-ray and neutron diffraction data [122].

Another structure has been proposed by Magrasó et al. [123] giving a good explanation why only compositions with off-stoichiometric La/W ratios below 6 are stable. It also clarifies the transport, doping and hydration behavior related to filling the oxygen sublattice, so that the vacancies tend to stabilize due to entropy contributions. The proposed structure can be written as $La_{28-x}W_{4+x}O_{54+\delta}v_{2-\delta}$, where v represents empty oxygen sites. The final model is quite similar to the one developed by Sherb et al. [122].

The Wagner equation for the H_2 flux (Equation 3-9) can be applied to investigate feasibility of rare earth tungstates as potential membrane materials. Assuming bulk diffusion, the calculation yields a hydrogen permeation value of 2 ml·min^{-1}·cm^{-2} at 800 °C for a membrane thickness 10 µm and $pH_2 \approx 10$ atm at the feed-side [124]. H_2 flux was obtained experimentally by Escolástico et al. for LnWO-based bulk membranes and was found to vary between $5 \cdot 10^{-3}$ - $5 \cdot 10^{-2}$ ml·min^{-1}·cm^{-2} for $Nd_{5.5}WO_{12-\delta}$ and flux up to 0.1 ml·min^{-1}·cm^{-2} for $La_{5.5}WO_{12-\delta}$ at 1000 °C [125,126]. Higher flux values are obtained by doping these materials with transition metals [108,125,126].

Furthermore, promising indications regarding chemical stability of $La_{5.4}WO_{11.7}$ and $Nd_{5.5}WO_{12-\delta}$, have been reported through conductivity studies in the temperature range 600 to 1000 °C and after long term exposure to gas flow containing CO_2, and CH_4 [108,127]. $Nd_{5.5}WO_{12-\delta}$ was also tested regarding stability under different environments including H_2S, CO_2, CO, H_2 at 500 °C and the material remained unchanged [108,125,126]. Therefore, these materials were chosen to be studied in

the frame of the present study. $La_{5.5}WO_{11.7}$ has also been prepared effectively with tape casting technique that will be adapted for the manufacturing of asymmetric membranes, thus fulfilling the material requirement for effective thin film membrane preparation [128].

3.5 Membrane Module Design

There are different possible designs for membranes as gas separators. The most appropriate should fulfill different requirements such as high active surface area, mechanical integrity etc. More specifically, the permeation rates could be further improved by the optimization of membrane architecture [129]:

Regarding OTM, the tubular design concept has been suggested as optimal choice for air separation units in terms of specific surface area and manufacturing aspects like manifolding and sealing [130,284].

As outlined above, membranes should be as thin as possible in order to maximize the flux through the membrane. Consequently, these thin membranes have to be supported by a macro-porous support. For the development of such asymmetric membranes, defect-free thin films on highly porous support are essential.

This design also requires different porous interlayers and catalytic layers, which in turn requires sophisticated manufacturing [131]. A general evaluation of membrane module concepts was performed by Vente et al. [132] where every concept was proved to have advantages and disadvantages. Therefore, every architecture concept should be considered individually for each application and the boundary conditions related to the available manufacturing technology [131]. In the following paragraphs the main concepts are presented

Honeycomb structures

The honeycomb structure offers high membrane area per volume. This design concept includes many advantages such as high surface area and robustness despite its relative thin walls [133]. It is illustrated in Figure 3-8. The monoliths can be manufactured by extrusion which allows mass production. Unfortunately, this architecture cannot be technically realized due to lack of appropriate manifolds of the required gas streams.

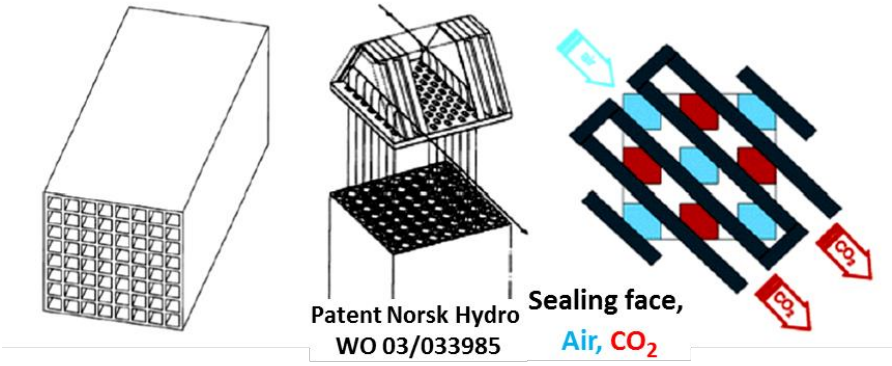

Figure 3-8 Honeycomb structure (left) and design of manifold (middle and right) [133].

Tubular Design

The majority of membranes are tubular, especially if they are applied in filtration processes. Therefore, this concept is investigated by several research groups. The Fraunhofer Institute of Ceramic Technologies and Systems (IKTS) developed a transportable demonstration unit based on extruded BSCF tubes with wall thickness of 0.5 - 1 mm, within the MEM-BRAIN consortium. The concept is based on a parallel configuration of BSCF tubes that are closed at one end and loaded with ambient air flow the other end as it is shown in Figure 3-9. This design enables easy transportation while it avoids large pressure vessels and compressors. The oxygen is pumped from the tubes at a pressure of 20 – 100 mbar. An improved design (Figure 3-9) was realized by RWTH Aachen University in the frame of OXYCOAL-AC project that can operate at a permeate pressure of 0.5-1 bar resulting in an O_2 flow of 0.5 ton/day while the pressure vessel can withstand pressures up to 20 bar [131]. It was shown by Vente et al. [130] that this concept is currently the optimal choice, compared to other possibilities such as hollow fibre, multi-channel monolith, tube and plate concepts since it offers larger membrane areas.

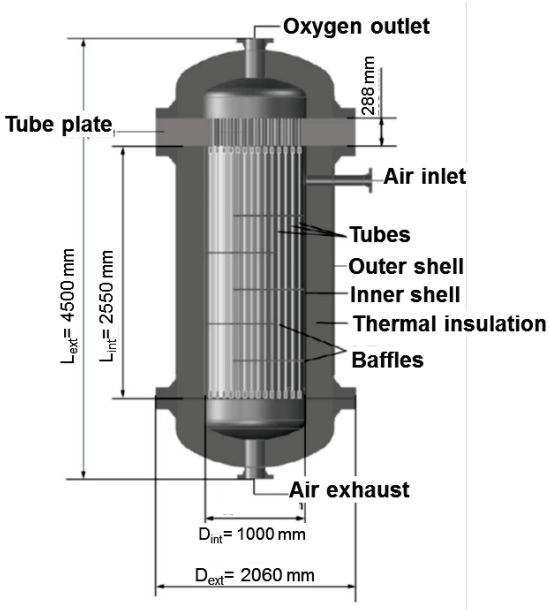

Figure 3-9 Full scale module for the tubular membrane concept with membrane area 157.3 m^2. The tubes are fixed on the top of the module and centered in the bottom due to the different thermal expansion of the materials used [130].

Planar Design

The most beneficial manufacturing method for the planar design is the tape casting technique since it provides maximum flexibility in terms of sizing, tailoring of flat ceramic components and mass production [134]. Air Products components have developed and scaled-up a system based on tape-casted asymmetric membranes realizing a 5 tons/ day oxygen generation, while a plant with capability of 150 tons/ day is currently constructed with the frame of a consortium in US [135]. The main benefit of this design is that offers large surface area as well as the ability to scale-up. Moreover, the symmetric assembly (Figure 3-10) where the membrane layers are outside and supported by the porous structures can withstand the mechanical stresses from the compressed air at the feed side [131].

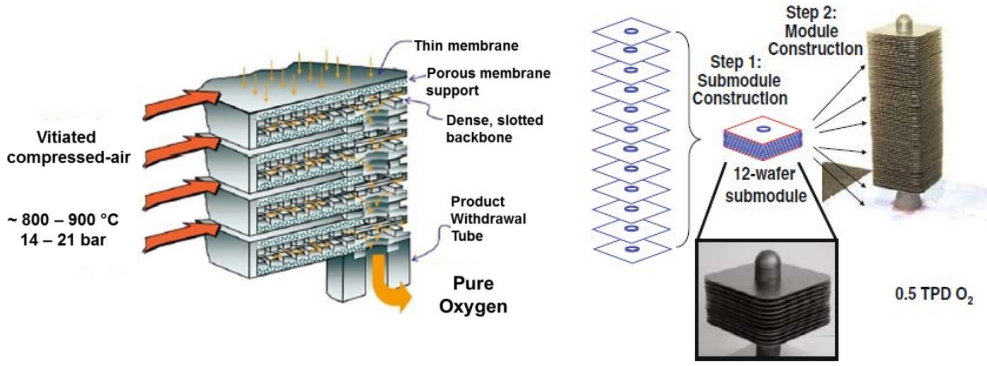

Figure 3-10 Oxygen Module Architecture (left) and a commercial module (right)– Planar Wafer Stack Design [136].

4 Mechanical Properties

From the previous chapters, it becomes clear that oxygen/hydrogen membrane components need to be operated at intermediate to high temperatures (800 - 900 °C/ 600 - 800 °C, respectively) and under large pressure gradients [34,137,138]. Realization of the technology therefore depends on the mechanical reliability of the components, which are subjected to stresses that mainly arise from oxygen stoichiometry gradients and external pressure during operation [279,284]. Other phenomena that might generate stresses during fabrication and subsequent use are shrinkage and thermal expansion mismatches between the coating and the substrate or among the cell components [139]. In order to warrant the robustness of the membrane modules over long operation periods, risks of mechanical failure need to be estimated and reduced to tolerable levels. Moreover, creep at the operational temperatures seems to be critical for application [184,140]. Therefore, knowledge of the mechanical properties in application relevant temperature ranges and environments is essential. The mechanical characterization of the membrane materials in the current work was focused on the determination of Young's Modulus (E), fracture strength (σ_f), fracture toughness (K_{Ic}), creep rates ($\dot{\varepsilon}$), which are all critical parameters for the system's reliable operation.

4.1 Young's Modulus

Most solid materials respond to small stresses by elastic deformation which is proportional to the applied stress, as described by Hooke's law [141]:

$$\sigma = E \cdot \varepsilon \qquad \text{Equation 4-1}$$

where E is Young's or elastic modulus, ε is the strain of the material defined as:

$$\varepsilon = \frac{l - l_0}{l_0} \qquad \text{Equation 4-2}$$

with l length under the applied stress, l_0 original length.

If the stress is increased above the reversible elastic strain limit either direct fracture without significant plastic deformation or plastic deformation and then fracture follows [182].

Elastic moduli can be determined with different static or dynamic methods. In static methods the deformation of a specimen under known load is measured and the elastic modulus is then calculated from stress and strain. The characterization techniques will be discussed on the basis of American Society for Testing and Materials (ASTM) standards that were developed to assure repeatability and reliability of testing. Tensile testing specimens are typically difficult to be fabricated from ceramics and strains are usually small and difficult to measure in compression, thus biaxial bending tests are most common for brittle materials [142].

- The biaxial ring-on-ring test is a common test method for analyzing materials' behavior. A benefit of this method is easy test piece preparation, thin sheet materials can also be tested and testing of specimens is not influenced by their cutting edges; a known problem for the most common three-point bending test [143,144,236].

- Micro-indentation is also an extensively used test for the determination of Young's modulus due to its simplicity and easy sample preparation. Another benefit of this test is the possibility to test small specimens that furthermore remain macroscopically undamaged. The test can engage various indentation tips, mostly a Vickers indenter with a diagonal of the diamond pyramidal tip with angle of 136° is used [229,181].

- Impulse Excitation technique (IET) is a non-destructive dynamic mechanical test for the investigation of Young's modulus. It is based on the eigen frequency of the tested specimens. This technique gives the possibility of E measurement over temperature and under various atmospheres [145].

Young's moduli of different oxygen transport membrane materials considered as membrane candidates are given in the following table:

Table 4-1 Young's moduli E of selected oxygen transport membrane materials

Structure	Material	E (GPa)	T (°C)	Testing method	Ref
Perovskites	BSCF5582	~ 62	RT	Indentation, Ring-on-ring	146, 147
	BSCF5582 (38% porosity)	33	RT	Ring-on-ring	148
	LSCF	70/ 115	RT	Resonant ultrasound spectroscopy/ Ring-on-ring	149, 153
	$SrTiO_3$	162	RT	Sound velocity	150
Fluorites	$Ce_{0.9}Gd_{0.1}O_2$	~180	RT	4-point bending Ring-on-ring	151, 152

For most materials, E has the tendency to decrease with increasing temperature [149]. However, BSCF5582 shows an abnormal evolution of E with temperature has been reported. From E ~ 63 GPa at RT, *E* reaches a minimum value of ~ 45 GPa at 200 °C, then it increases again to reach a maximum value of ~ 52 GPa at 400 °C and subsequently decreases to 48 GPa at 800 °C [146,148]. The minimum E at 200°C has been attributed to spin transition of Co atoms [146]. Extensive studies of mechanical properties of LSCF and BSCF and literature comparison to other perovskite structures were performed by Huang and Rutkowski [153,249].

Young's moduli of different proton transport membrane materials are given in the next table. Note, that temperature dependencies have not been published for this materials class.

Table 4-2 Young's moduli E of hydrogen transport membrane materials candidate materials

Structure	Material	E (GPa)	T (°C)	Testing Method	Ref
Perovskites	$BaZrO_3$	240	RT	Ultrasonic	154
	$BaCeO_3$	154	RT	Ultrasonic	155
Fluorites	LWO54	122 ± 5	RT	Micro-indentation	156
Ortho-niobates	$LaNbO_4$	95 ± 10	RT	Resonance Vibration	157

Young's modulus of polycrystalline ceramics, without grain boundary softening, is expected to decrease about 1 % per hundred Kelvins [278], which agrees with the temperature dependence of Young's modulus generally described by Hillig [158]:

$$\frac{E}{E_0} = 1 - \left(\frac{T}{T_m}\right)^3$$ Equation 4-3

Where E_0 is the Young's modulus at room temperature, and T_m the melting temperature of the material.

4.2 Fracture strength

Most polycrystalline ceramics are fabricated by either solid- or liquid-phase sintering which leads to inevitable flaws. Therefore, ceramic materials usually exhibit large statistical variation in fracture stress given that the failure is initiated by strength limiting flaws. These flaws can be randomly distributed throughout the volume of the sample or located on the surface or edges of the specimen due to machining effects. Fracture stress of ceramics depends on the size and location of flaws. Strength is statistically analyzed and connected to a certain failure probability as well as to a specific effectively deformed area or volume [182].

Regarding bending tests, where the maximum tensile stress occurs at one of the surfaces, the probability of failure due to flaws close to the tensile surface will be the highest. The fracture stresses can be assessed statistically by the Weibull distribution that yields a characteristic fracture strength, where 63% of the specimens will fail. Using the Weibull modulus and this characteristic strength, the fracture stress for any acceptable failure probability and component size can then be calculated. The Weibull distribution parameters for advanced ceramics are standardized in ASTM C1239-07 [159].

More precisely, the two-parameter Weibull distribution describes the failure probability as [160]:

$$P_f(V_0) = 1 - exp\left[-\left(\frac{\sigma}{\sigma_0}\right)^w\right]$$ Equation 4-4

Where σ_0 and w are constants, referred as characteristic strength and Weibull modulus, respectively. If $\sigma = \sigma_0$ then $P_f(V_0)$ equals 0.632, hence the characteristic strength σ_0 corresponds to the stress where 63.2% of the samples will fail. The Weibull modulus *w* links the dependence of fracture stress and failure probability [161].

One of the great advantages of the Weibull distribution is that it can be applied to predict the specimen / component size effect on strength. Since the failure probability depends on the tested effective volume or area (if the failure relevant defects are in the volume or at the surface respectively), it is expected that larger components will be weaker since statistically they contain more and larger flaws. This means that a large component used in application will have a lower strength than a small test specimen for the same failure probability[162]. This correlation can be described by

$$\frac{\sigma_2}{\sigma_1} = \left(\frac{V_1}{V_2}\right)^{\frac{1}{w}} \qquad \text{Equation 4-5}$$

Where V_1 and V_2 refer to the effective volume of specimen and component respectively.

According to ISO 20501:2003 (E), determined Weibull parameters are corrected for the specific number of specimens. The Weibull modulus is generally biased by the number of specimens, so according to the ISO, an unbiased estimation is obtained by multiplying the calculated *w* by a correction factor. While *w* is significantly influenced by the statistical bias, the bias associated with the characteristic strength can be neglected.

The standard deviation of Weibull modulus s_m and characteristic strength $s_{\sigma 0}$ is estimated again in correlation with the samples' number N as following:

$$s_w = \frac{w}{\sqrt{N}} \qquad \text{Equation 4-6}$$

$$s_{\sigma_0} = \frac{\sigma_0}{w\sqrt{N}} \qquad \text{Equation 4-7}$$

Characteristic fracture strengths were reported for membrane materials similar to the case of E. Unfortunately, direct comparison of values is not possible, since the dependence on several experimental parameters like test method, effective stress volume, sample geometry and porosity lead to misleading conclusions.

Table 4-3 Fracture strength of oxygen transport candidate materials

Structure	Material	σ_0 (MPa)	T (°C)	Testing method	Ref
Perovskites	BSCF5582	98 ± 8	RT	Ring-on-ring	153
	BSCF5582 (38% porosity)	31 ± 1	RT	Ring-on-ring	152
	LSCF	73 ± 2	RT	Ring-on-ring	152
Fluorites	$Ce_{0.9}Gd_{0.1}O_2$	55 ± 3	RT	4-point bending	152

It was found for BSCF55882, that temperature dependent fracture strength exhibits a similar behavior compared to *E.* Strength shows a minimum value at ~400 °C and increases at higher temperatures. This effect was noticed for dense and porous materials [146,148]. An analogous behavior was also observed for $La_{0.58}Sr_{0.4}Co_{0.2}Fe_{0.8}O_{3-\delta}$ and the origin was again attributed to Co spin transitions [163].

Table 4-4 Fracture strength of hydrogen transport candidate materials and substrates

Structure	Material	σ_0 (MPa)	T (°C)	Ref
Fluorites	LWO54	50-120	RT	Current work
Ortho-niobates	$LaNbO_4$	35 ± 10	RT	157
Cubic	MgO	38 - 48	RT	164

Some ceramic materials are prone to subcritical crack growth (SCG) where cracks are propagated by mechanical loading or / and by chemical interaction of the material with the environment such as moisture or corrosive atmosphere [165]. The subcritical crack growth rate v is connected to the following power-law crack velocity according to ASTM C1465 [166]:

$$v = A\left(\frac{K_I}{K_{IC}}\right)^n \qquad \text{Equation 4-8}$$

Where A is a constant, K_I is mode I stress intensity factor, K_{IC} is fracture toughness under mode I condition, and n is the subcritical crack growth exponent.

In case of testing under constant stress rate, the characteristic strength σ_0 is connected to the stress rate $\dot{\sigma}$:

$$log\ \sigma_0 = \frac{1}{n+1} log\ \dot{\sigma} + log\ D$$ Equation 4-9

Where D is the SCG constant. Consequently, the characteristic fracture strength depends on the stress rate for materials prone to SCG. The experimental approach for the determination of SCG is via bending tests, where different stress rates are applied [168,167]. Subcritical crack growth phenomena are common in glass but are also observed in ceramic oxides. Systematic studies of SCG for oxygen transport membrane materials were performed by Pećanac [152].

4.3 Fracture toughness

Fracture toughness is measured to describe the resistance of a material to unstable crack propagation and fracture. Vickers indentation has become popular for the evaluation of K_{IC} [168]. In this method, a diamond indenter is applied to the surface of the specimen to be tested as described in the chapters for hardness and elastic modulus testing. After removal, the sizes of the cracks that originate from the edges of the indent above a critical load are measured.

Cross-sectional views of indents are shown in Figure 4-1. At low loads, Palmqvist cracks are more likely, while at high loads fully developed median cracks (radial or half penny) typically form [168].

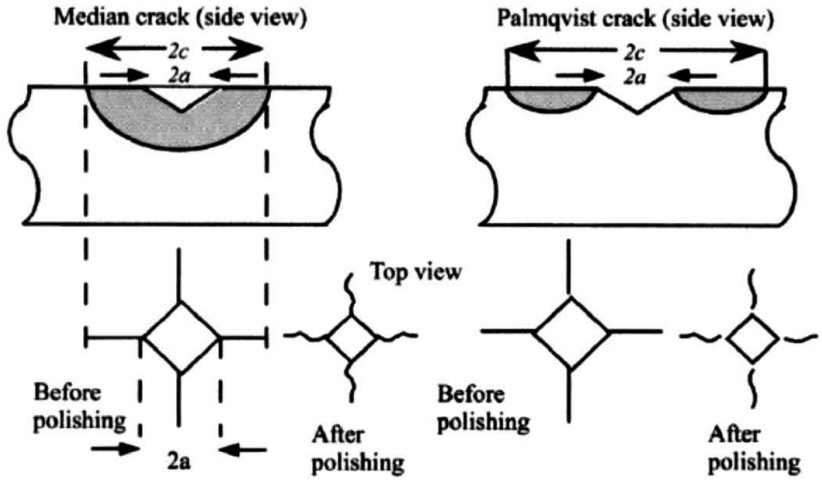

Figure 4-1 Crack systems developed from the Vickers indents, (left) median or radial crack, (right) Palmqvist crack [168]

Fracture toughness values for the different candidate membrane materials are summarized in the following tables:

Table 4-5 Fracture Toughness of oxygen transport membrane materials at RT

Structure	Material	K_{1c} $(MPa \cdot \sqrt{m})$	Reference
Perovskites	$SrTiO_3$	0.89	169
	BSCF5582	0.74 ± 0.024	249
	LSCF	1.2	149
Fluorites	$Ce_{0.9}Gd_{0.1}O_2$	1.3	170

Table 4-6 Fracture Toughness of hydrogen transport membrane materials at RT

Structure	Material	K_{1c} $(MPa \cdot \sqrt{m})$	Reference
Perovskites	$BaZrO_3$	1.5 ± 0.4	171
Fluorites	LWO54	2.1 ± 0.2	156
Ortho-niobates	$LaNbO_4$	0.7	172

Overall, reported room temperature fracture toughness data of oxygen transport membrane materials are similar. The indentation fracture toughness of BSCF5582

was investigated from RT up to 350 °C and it was found that it decreases from 1 to 0.4 $\boldsymbol{MPa} \cdot \sqrt{m}$ between RT to 100 °C and then remains rather constant up to 350 °C [146]. Further investigations using the indentation strength method showed that fracture toughness was still increasing for temperatures above 400 °C until it reaches 80% of the room temperature value at 800°C following similar behavior as reported for the fracture stress [173]. In the current work fracture toughness values were only obtained at room temperature.

Most reported fracture toughness values of hydrogen transport materials appear to be higher than for oxygen transport materials (Table 4-5 and Table 4-6). Roa et al. [174] reported the hardness and elastic properties at room temperature for $La_{6-x}WO_{12-\delta}$ determined via micro-indentation for the nominal composition range LWO48-LWO64 for different sintering temperatures. They concluded that both hardness and Young's Modulus did not show a significant variation with either composition or sintering temperature. Elevated temperature data were not reported.

4.4 Fracture Energy Criterion

The original idea of Griffith's fracture energy criterion is that the energy consumed in forming new surface as a crack propagates is balanced by the released elastic energy. In this case, the critical condition for fracture arises once the rate at which energy is released is greater than the rate at which it is consumed [168]. Pre-existing flaws will be responsible for failure under tensile stresses. Hence, the fracture toughness can be estimated by identifying these flaws and estimating their size. Fractography is applied for these investigations of samples broken by bending tests. The most common flaws in ceramics are large pores, large grains, inclusions, microstructural inhomogeneities as well as machining induced flaws [175,176].

According to Griffith's criterion fracture occurs from preexisting flaws when a critical applied stress is exceeded. Then the stress intensity factor exceeds the fracture toughness and unstable crack growth occurs [177,178,179]. The fracture toughness is estimated from the following equation:

$$K_{IC} = \left(\frac{Y}{Z}\right) \cdot \sigma \cdot \sqrt{c}$$ Equation 4-10

Where *Y* is the geometry factor dependent on the loading conditions and the shape of specimen, as well as the shape of the defect. In a uniform stress field, Y is independent of c and equals to $Y = \sqrt{\pi}$ for volume flaws and $Y = 1.12\sqrt{\pi}$ for surface flaws. Shape factor Z is unity in the case of linear crack front defect and $Z = \pi/2$ for circular or penny-shaped flaw [180].

4.5 Creep

4.5.1 Fundamental aspects

One of the critical high temperature deformation / damage mechanisms is creep as it leads to tensile failure already under low stress. In general, creep behavior is affected by extrinsic and intrinsic parameters, such as stress, temperature and grain size.

Creep is a plastic deformation of a solid that typically occurs at high temperatures (T). For ceramics it is typically $T > 0.4\text{-}0.5 \cdot T_m$, where T_m is the melting point of the tested material in Kelvins [168]. It is an important deformation mode that affects the integrity of materials at elevated temperatures, even for brittle materials that normally exhibit extremely limited or no plasticity at room temperature [181,182].

For the design process, the amount of creep strain must usually be kept below a particular value to warrant structural stability. The strain-time behavior associated with creep under constant stress is illustrated in the Figure 4-2.

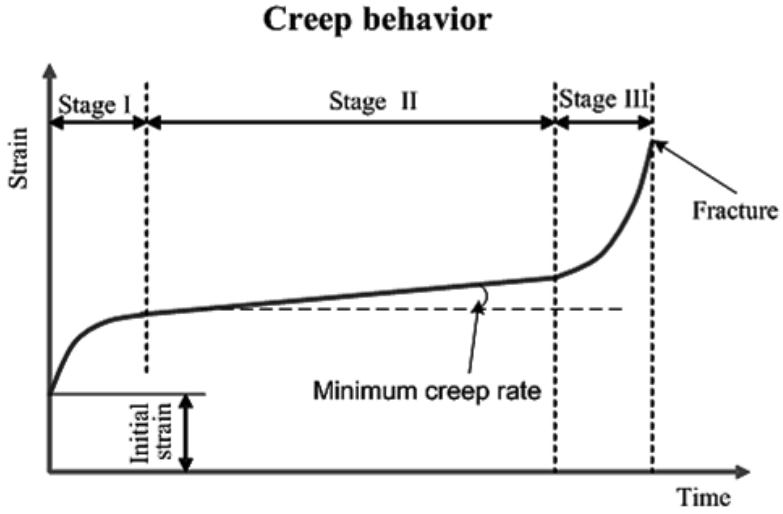

Figure 4-2 The three stages of creep deformation I. primary II, secondary III and tertiary.

Typically, the creep response of a solid is determined by measuring the strain rate as a function of applied stress. This is done, simply by applying a load to the sample at elevated temperatures, and measuring its deformation as function of time. The creep behavior can usually be divided in three stages:

Stage I: Primary creep. In this stage the strain rate decreases with increasing time

Stage II: Secondary, steady-state or minimum creep. Here, strain rate is constant and creep is considered to be the result of the deformation of a stable microstructure, thus the creep rate $\dot{\varepsilon}$ is evaluated in this regime [183].

Stage III: In tertiary creep, the strain rate accelerates just prior to specimen failure. Formation of cracks or nucleation and growth of cavities is observed in microstructure. In ceramics, the tertiary creep stage is often very short or entirely missing [182].

Creep depends in a complex way on stress, time, temperature, grain size, grain shape, microstructure, volume fraction and dislocation mobility.

Since the first and the third stages happen very fast in most cases, the secondary creep stage is of major concern from an engineering point of view and for lifetime

predictions. The secondary or minimum creep rate dependence of materials, where the microstructure, stress as well as the environment plays an important role is described mathematically by the following general expression [184]:

$$\dot{\varepsilon} = A \cdot \left(\frac{1}{d}\right)^{p} \cdot (pO_2)^{m} \cdot \sigma^{n} \cdot exp\left(-\frac{Qa}{RT}\right) \qquad \text{Equation 4-11}$$

Where A is a dimensionless constant, p the grain size exponent, m the oxygen partial pressure exponent, n is the stress exponent, Qa the activation energy, R the universal gas constant. The oxygen partial pressure $pO2$, the applied stress σ, grain size d and temperature T are the experimental input parameters.

The creep behavior of a material can be analyzed in terms of experimental results with multi-linear fitting routines in order to obtain the creep parameters as illustrated in Figure 4-3.

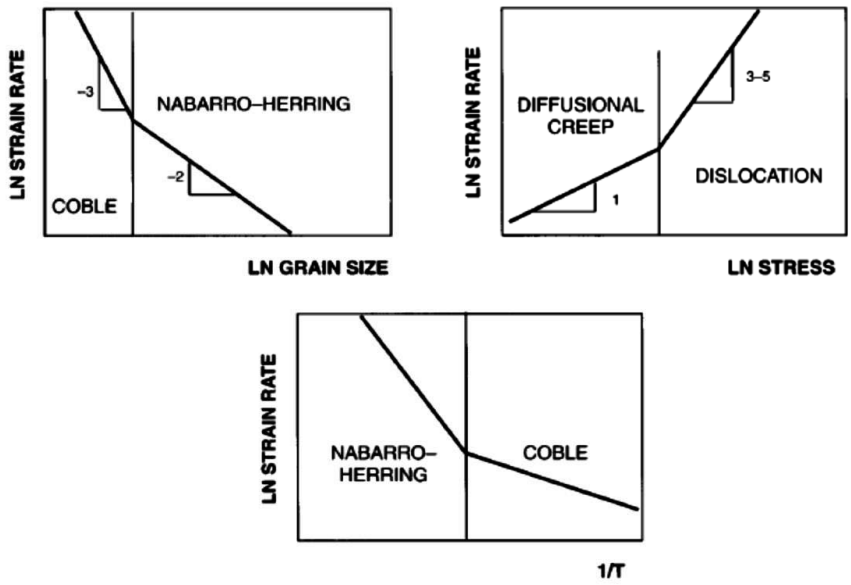

Figure 4-3 Experimental approaches to determine creep mechanisms [182].

The various creep mechanisms give rise to different *p* and *n* values and some of these are summarized along with associated mechanism and diffusion path in Table 4-7. Since from the analysis of creep data, values of *p* and *n* can be obtained and

thus, in principle, one can identify the predominant mechanism on the basis of Table 4-7:

Table 4-7 Creep equation exponents and diffusion paths for various creep mechanism [182]

Creep mechanism	p	n	Diffusion path
Dislocation creep mechanisms			
Dislocation glide climb, climb controlled	0	4-5	Lattice
Dislocation glide climb, glide controlled	0	3	Lattice
Dissolution of dislocation loops	0	4	Lattice
Dislocation climb without glide	0	3	Lattice
Dislocation climb by pipe diffusion	0	5	Dislocation core
Diffusional creep mechanisms			
Vacancy flow through grains (Nabarro-Herring)	2	1	Lattice
Vacancy flow along grain boundaries (Coble)	2	1	Grain boundary
Interface reaction control	1	2	Lattice/grain boundary
Grain boundary sliding mechanisms			
Sliding with liquid	3	1	Liquid
Sliding without liquid (diffusion control)	2-3	1	Lattice/grain boundary

In general, three main mechanisms are governing steady state creep behavior: diffusion, dislocation movement and grain-boundary sliding [182]:

Diffusional creep is driven by the movement of single atoms or ions either by lattice diffusion (Nabaro-Herring creep) [185,186] or by grain-boundary diffusion (Coble creep [187]).

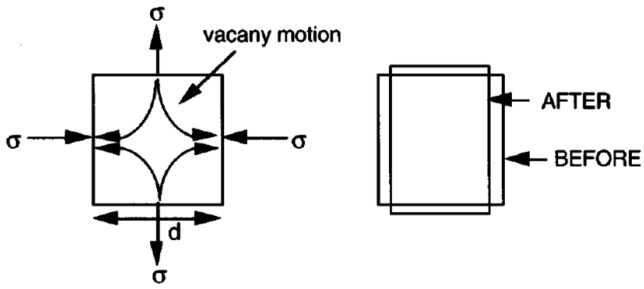

Figure 4-4 Lattice diffusion induced by stress in tensile and compression where a) illustrates the arrows in the crystal show possible directions of vacancy motion and b) how diffusion leads to permanent deformation [182].

Hence, the Nabarro-Herring creep is controlled by the lattice diffusivity D_L and Coble creep by the grain boundary diffusivity D_G. In this context the grain boundary width d_G is important, since for Coble model, the creep rate depends on grain size d^{-3}. The higher sensitivity to grain sizes allows Coble creep to dominate over Nabarro-Herring creep at lower temperatures. For both creep mechanisms, it is assumed that the grain boundaries are perfect sources or sinks for vacancies. The diffusion process involves more than one ionic species, thus the creep rate depends on the diffusion rate of the slowest ion moving along the shortest diffusion path [161]. Figure 4-5 illustrates the different creep mechanisms [185].

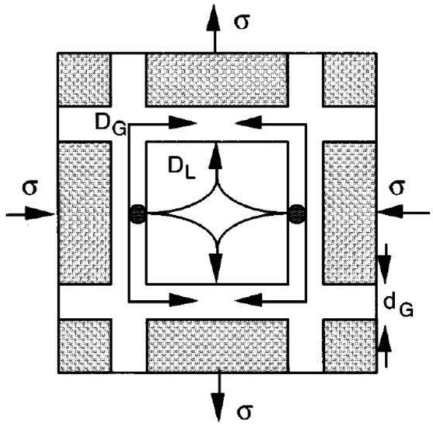

Figure 4-5 Possible atom diffusion paths (indicated by arrows) after inducing stress in polycrystalline material. Diffusional creep can occur either through the grains (D_L) or along the grain boundaries (D_G) [182].

Dislocation creep is a mechanism involving motion of dislocations. Dislocations can move by gliding in a slip plane, a process requiring little thermal activation. Dislocation creep is not influenced by the grain size and usually occurs in metals at relatively low temperature and high stress [188]. For polycrystalline ceramic oxides dislocation creep has only been reported for some materials as depicted in Figure 4-6 [189].

A third group of creep mechanisms are those that involve grain boundary sliding (GBS). Some ceramics possess a grain boundary glassy phase that aids densification in the fabrication process. The softening of such a phase at high temperatures allows creep to occur by grain boundary sliding [182].

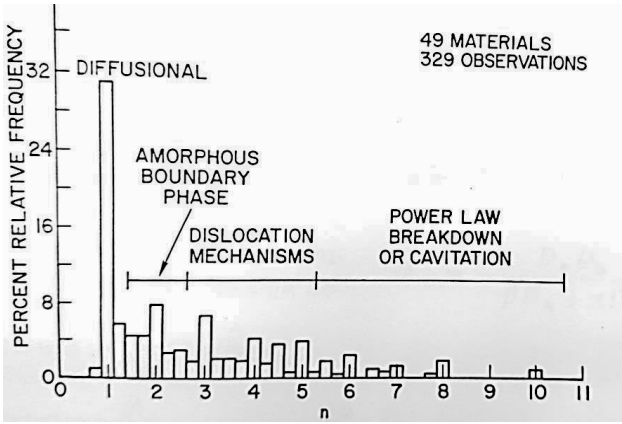

Figure 4-6 Frequency histogram of stress exponents for ceramic polycrystals [190].

The histogram of polycrystalline ceramics show that the most frequently observed stress exponent is close to 1, which indicates the importance of the diffusion mechanisms. Diffusional mechanisms are so common in these materials due to the fact that the inherent resistance to dislocation glide is maintained even at higher temperatures. Thus, mechanisms involving dislocation glide are suppressed compared to metals. Moreover, the polycrystalline ceramic usually have very small grains sizes, so diffusional mechanisms are enhanced [191].

The complexity of the nature of ceramic materials enhances the difficulty of clearly assigning the obtained creep parameters to one of the creep models mentioned above. Many of the models predict similar or identical values of stress exponent, activation energy and grain size exponent. Additionally, mechanisms can also act

simultaneously giving rise to values that are not characteristic of any single mechanism. Therefore, additional microstructural studies of the samples before and after the test may give evidence of prevailing mechanism. Features like cavity formation and cracking, changes in grain shape or size or dislocation density as well as grain boundary sliding may be observed. Nevertheless, these methods will not yield information about the kinetics, but only provide direct evidence that a mechanism has operated during creep [192].

Data on the creep properties of various membrane candidate materials are summarized in Table 4-8 and Table 4-9:

Table 4-8 Creep parameters for OTM candidate materials

Structure	Material	Qa	N	Mechanism	Testing conditions	Grain size (µm)	Ref
Perovskites	BSCF5582	340±40	1.7±0.2	Cation diffusion	850–950 °C 30-63 MPa	29±12	249
	LSCF38	350±50	2.6-2.9	Dislocation	750–950 °C 20-50 MPa	1.4±0.7	193
	$La_{0.5}Sr_{0.5}CoO_{3-\delta}$	619±56	1.2±0.1		900–1050 °C 5-28 MPa	~ 2	281
Fluorites	$Ce_{0.8}Gd_{0.2}O_{1.9-\delta}$	100±30	1.8±0.6	Diffusion / Dislocation	800-900 °C 30-120 MPa	4±1	193

Table 4-9 Creep parameters for HTM and substrate candidate materials

Structure	Material	Q_a	n	Mechanism	Testing conditions	Grain size (µm)	Ref
Perovskites	$BaZrO_3$	460±30	0.9±0.1	Diffusion/ GBS	1300-1400 °C 10-100 MPa	~4	194
	$BaCe_{0.98}Y_{0.2}O_{3-\delta}$	343±30	1.1±0.1	Diffusion	1200-1450 °C 1-150 MPa	~9	195
Fluorites	CeO2	160±60	2.3±1.1	Diffusion/ Dislocation	800-900 °C 60-120 MPa	16±6	193
Cubic	MgO	385±15	4.3-4.9	Dislocation	800-1200 °C 30-100 MPa	15±10	193

4.5.2 Literature overview on creep properties of perovskites

Another topic of focus is the effect of doping on the creep behavior of perovskites. Usually, minor amounts of additives tend to concentrate at the grain boundaries and / or in the portion of the grain adjacent to the grain boundaries. In case those additions exceed the solubility limits, films or secondary phases can be formed along the grain

boundaries. Impurities of certain kinds affect the material in different ways like affecting the cohesive strength, the diffusivity along the grain boundaries as well as the migration ability during mechanical testing. Impurities might also have an influence on GBS [196].

It has been demonstrated that addition of trace amounts (≤ 1000 p.p.m.) of rare-earth dopants such as yttrium, lanthanum or neodymium can reduce the creep rate of fine grained (around 1-2 µm grain size) by several orders of magnitude [197,198,199]. The benefit of Y-doping of magnesia-doped alumina was evidenced by a reduction in creep rates by a factor of 5 for 500 ppm and 15 for 360 ppm doping level, respectively [200,201]. Furthermore, a decrease in the creep rate by a factor of 15 was reported for alumina with 1000 ppm Zr doping [202]. One suggested explanation for this effect was that outsize ions segregate to more energetically favorable grain boundaries and improve creep resistance by blocking a few critical diffusive pathways [203].

The compressive creep behavior of BSCF has been investigated by Yi et al. [184] and Rutkowski et al. [140]. Both groups of authors have reported creep deformation of BSCF in the temperature range from 800 to 950 °C to be dominated by cation diffusion via the oxide lattice (bulk) and along grain boundaries. A profound increase of the creep rate is observed above ~850 °C. Below this temperature a sluggish decomposition of BSCF occurs into cubic and hexagonal polymorphs. Both cited groups of authors conclude that the presence of hexagonal polymorphs significantly enhances the material's creep resistance. The amount of secondary phases in BSCF is found to depend strongly on the thermal history of the material [140]. Since the cubic phase is the thermodynamically stable phase above 850 °C, thermal cycling gives rise to a pronounced hysteresis in the creep behavior of BSCF. Creep related data on these parameters give important information on the underlying creep mechanism, but also influence design criteria for OTM membranes. Mechanical characterization of this composition manufactured by extrusion regarding creep and strength revealed that the thermo-mechanical characteristics of BSCF and BSCF·Z3 (3 % Zr doping) mostly agree [45,254].

The following paragraphs are focused on creep studies on the end members of STF materials as well as $Sr(Fe/Co)O_{3-\delta}$ materials that show more complex behavior.

Initially, Klevelant et al. [204] investigated the compressive creep performance of strontium-deficient and strontium-excess $SrFeO_{3-\delta}$ materials (grain size < 5 µm, porosity ≤5%) in the temperature range of 800 – 1000 °C for a stress regime of 2.5 - 25 MPa. A stress exponent n ~ 1 for both materials and activation energy of 260 ± 30 kJ/mol were determined and a cation controlling creep mechanism was suggested. The creep rates were higher for the Sr deficient material than the Sr-excess material. But both materials contained secondary phases thus activation energies might have been biased since they are quite lower than similar perovskite materials. Majkic et al. [205] investigated the creep behavior of $SrCo_{0.8}Fe_{0.2}O_{3-\delta}$ (grain size 2.6 - 6.8 µm) in the temperature range 850 - 975°C for a stress range of 2 - 80 MPa. They observed a variety of responses. At lower temperatures, a stress exponent n ~ 1 and activation energy of 471 kJ/mol were determined, while at higher temperatures 925 – 975 °C, the apparent stress exponent increased from 2.2 to 2.9, whereas the activation energy decreased to 275 kJ/mol. A threshold stress according to the Ashby-Verall model was used to give an explanation for the increased stress exponent [206]. Regarding the change in activation energy with temperature a change in the cations that control the diffusion mechanism was suggested; either A or B site. However, in this study microstructural data were not correlated to the creep data.

Further creep studies on this group of ceramics by Arellano-Lopez et al. [207] in the temperature range 940 – 1000 °C for a stress range of 0.3 - 65 MPa revealed also different behavior for $Sr(FeCo)_{1.5}O_x$. While for the low stress regime, a stress exponent of ~ 1 and an activation energy of 110 - 135 kJ/mol (1.9 MPa) was observed, for higher stresses a transition took place, i.e. the stress exponent increased to ~2.4 - 3.1 along with the activation energy to 425-453 kJ/mol (23 MPa). The authors applied extensive microstructural studies on the un-deformed and deformed samples and in conclusion they suggested a diffusion controlled creep at lower stresses and dislocation glide at higher stresses. The transition stress seemed to be temperature dependent.

Regarding the end member of the ST·F100x group, $SrTiO_3$ was investigated in terms of creep resistance by Singh et al. [208] at temperatures of 1200 – 1345 °C and a stress range of 0.05 - 30 MPa, respectively. The tested material was dense with a grain size of ~ 6 µm. A temperature independent stress exponent of n~1 was determined, and an activation energy of 628 ± 24 kJ/mol, suggesting diffusion of

cations as the rate-controlling creep mechanism. The activation energy for the diffusion of Sr in polycrystalline $SrTiO_3$ has been reported to be 293 kJ/mol [209] for 1190 – 1215 °C. Since the determined activation energy was much higher, B-site Ti^{4+} cation was suggested as the deformation controlling species. Park et al. [210] also suggested B-site Ti^{4+} as the rate-controlling species in $BaTiO_3$. Moreover, studies on creep deformation by Wang et al. [211] also reported an activation energy of 620 kJ/ mol for the {1 0 0} <0 1 0> orientation of single crystal $SrTiO_3$. The stress exponent for this material was 3.5 and the suggested creep mechanism was diffusion-assisted-dislocation-climb independent of temperature. It is possible that in polycrystalline $SrTiO_3$ Ti^{4+} is the rate controlling species due to its 4+ valence state and octahedral coordination with oxygen ions, as proposed by theoretical defect studies as well as experimental measurements for Ti^{4+} diffusion in titanates [212,213].

In order to predict the long term performance of a membrane structure, a maximum tolerable creep deformation has to be determined. According to Thomson et al. [214], membrane materials should not creep in a compressive mode more that 1 % per year in order to warrant reliable long term operation. Schulz et al.[215] calculated the compressive stress exerted on a membrane during operation in a CO_2 operation system to be approximately 30 MPa, hence as a guideline for the analysis the creep should be less than 1 % / year for a stress of 30 MPa.

The membrane will work under a pressure gradient resulting from the different oxygen partial pressure on its two sides as described in chapter 3.1. For $Sr(FeCo)_{1.5}O_x$ ceramics where no dependence of the oxygen partial pressure on creep was observed at the following conditions: pO_2 10^{-4} - 1 bar, temperature 940 - 1000 °C, stress 50 - 100 MPa [207]. Nevertheless, in the extended study of Majkic et al [216] for $La_{0.2}Sr_{0.8}Fe_{0.8}Cr_{0.2}O_{3-\delta}$ over a broad range of pO_2 (~ 0.21 - 10^{-14} atm) it was demonstrated that the material shows two remarkably different behaviors at high and low pO_2 of the aforementioned range. At high pO_2 (0.21 – 10^{-5} atm), the partial oxygen exponent was m = 0.04 while for the low pO_2 (10^{-7} - 10^{-14} atm) m= -0.5, showing an increase in strain rate. Rutkowski [45] reported for BSCF5582 m = -0.14 ± 0.014 for pO_2 ~200-10^{-5} mbar, stress and temperature range 20 - 29 MPa and 850 - 950 °C respectively. If creep is controlled by diffusion, the parameter m reflects the defect chemistry of the rate-controlling species since the non-stoichiometry depends on the pO_2 [217,218,219]. In case that the m differs from zero

value, the creep deformation is non uniform and additional stresses will arise which might eventually lead to damage.

5 Experimental

Various mechanical tests, supported by microstructural investigations, were performed to aid the understanding of the thermo-mechanical behavior and microstructural stability of the membrane materials. More precisely, depth sensitive indentation was used to determine Young's modulus and micro-hardness at room temperature. Fracture toughness was evaluated from the measurement of the crack length of the indentation cracks.

Micro- and macro-mechanical properties are expected to differ due to the effect of microstructure inhomogeneity. Indentation is considered as local measurement and yields information on the effect of local inhomogeneities for E such as grain boundaries, precipitates, phase de-mixing or segregation effects, while bending tests are extensively used as global measurement that yields information of materials macroscopic behavior including i.e. integral effect of porosity. Therefore, the results are used as a basis to simulate the behavior of materials in membrane systems/ modules. Moreover, bending tests are used for the fracture stress characterization, a critical parameter for the assessment of the reliability of final component. Hence, *E* and fracture strength were determined from ring-on-ring bending tests. Fracture strength of porous material at room temperature was determined with ball-on-3-balls tests, since the thickness of the supplied material excluded the use of ring-on-ring testing.

Creep behavior of all dense materials was investigated by compression tests, carried out in different atmospheres. The aim was to characterize the materials in application relevant conditions but in case of non-significant deformation at typical application temperature, higher temperatures and stresses were applied.

5.1 Materials

5.1.1 BSCF·Z100x

BSCFZ materials were provided by the University of Twente. (Group Inorganic Membranes) $Ba_{0.5}Sr_{0.5}(Co_{0.8}Fe_{0.2})_{1-x}Zr_xO_{3-\delta}$ (BSCF·Z100x) powders with x = 0, 0.01, 0.03, 0.05, and 0.10 prepared using a spray pyrolysis technique were purchased from CerPoTech (Norway). The as-received powders were ball-milled in ethanol and calcined at 900 °C for 6 h in air. Green cylinders were obtained by uniaxial pressing

at 50 MPa followed by isostatic pressing at 400 MPa. They were then sintered at 1120 °C for 30 h in air yielding a relative density of more than 95 %. Only BSCF·Z3 was sintered at 1050 °C for 3 h in order to yield similar grain size to the other materials. Grain size analysis was performed for reference samples sintered with same sintering parameters, at 1150 °C for 30 hours, in order to investigate the effect of Zr doping on the microstructure regarding grain size, porosity and secondary phases. Extended creep tests were also carried out for the investigation of the doping effect on creep mechanism of BSCF·Z100x. More details for the testing conditions and sample geometry are described in the relevant chapters.

Creep tests in compression were also performed for these materials in air. Testing temperatures were 800 to 950 °C, applied loads 30 and 63 MPa.

5.1.2 ST·F100x

STF materials were also produced by the University of Twente. $SrTi_{1-x}Fe_xO_{3-\delta}$ (ST·F100x) powders with x = 0.3, 0.5 and 0.7 were synthesized by spray pyrolysis using precursor solution consisting of stoichiometric amounts of cations. The precursor solutions were pyrolysed in a continuous air flow at 860 °C. The raw powders were calcined at 950 °C for 12 h in stagnant air and ball-milled in ethanol for 24 h. Rectangular bars in green state were obtained by uniaxial pressing at 50 MPa followed by isostatic pressing at 400 MPa yielding a relative green density of approximately 60 %. ST·F30 and ST·F50 samples were sintered at 1300 °C and ST·F70 at a lower temperature of 1180 °C, after optimization of the sintering behavior since samples were prone to crack on the surface [66,220], all for 20 h under stagnant air to a relative density of more than 95 %.

Microstructural studies before and after creep by means of XRD and EBSD analysis were also performed in order to gain more information regarding the creep mechanism. In addition, High Temperature XRD (HT-XRD) was also performed under air and vacuum. For this material grain size analysis was performed by EBSD measurements simultaneously with the grain orientation mapping.

Micro-indentation tests at room temperature were performed for the ST·F100x class to yield the E_{IT}, H_{IT} and K_{IC} values. Creep tests were carried out for the determination of creep mechanism. ST·F100x materials were tested for creep in compression at a

temperature range from 800 °C to 1000 °C and stresses of 10 – 80 MPa in air and vacuum. More details of the testing conditions and sample geometry are described in the relevant chapters.

5.1.3 LWO54

LWO54 powders were produced by solid state reaction and spray pyrolysis. For synthesizing the LWO54 powder following the solid state approach in IEK-1, La_2O_3 and WO_3 were used as starting oxides. They were mixed in the corresponding stoichiometric ratio and heated to 1500 °C for 12 h to complete the solid state synthesis and phase formation. Afterwards the resulting powder was ball-milled and sieved to achieve a suitable grain size. The material is named IEK here after.

As a second type of powder, commercially available LWO54 (Cerpotech, Norway) was used, which was manufactured by spray pyrolysis and calcined at 1100 °C in IEK-1 for reducing its sintering activity to suitable level (named as CPT in the following).The powder characteristics are presented in Appendix C.

From these starting powders, LWO54 samples were manufactured by isostatic pressing and sintered at 1500 °C. The relevant conditions and sample labels are listed in Table 5-1. LWO samples manufactured from the in-house produced powders (solid state synthesis) were named IEK-S, while the samples obtained from the commercially available powder after calcination were labelled as CPT-D and CPT-P, respectively for dense and porous tape casted materials. The stoichiometry was $La_{5.4}WO_{12-\delta}$, as ascertained by the chemical analysis.

In order to investigate the effect of temperature and atmosphere on dense material, extended analysis of Young's modulus was performed with various tests. Namely these tests were indentation, impulse excitation and ring-on-ring. A comparison among these techniques is also discussed. Strength of LWO54 at RT up to 1000°C was estimated from ring-on-ring tests. Fractography was also applied to the broken tested pieces to characterize the failure origins according to ASTM C1322 [221].

Creep tests in compression were also performed for LWO54 in air and application related atmospheres. Testing temperatures were 700 to 1450 °C with applied loads ranging from 20 - 63 MPa, and atmospheres such as air, vacuum, Ar / 4 % H_2, Ar / 4

% H_2 2.5% H_2O. Detailed conditions are given in the next sessions for each characterization technique.

Table 5-1 List of LWO54 materials

	Powder synthesis	Manufacturing Method	Sintering conditions T_{sint} / dwell time (°C/ h)
Dense			
IEK-S1	Solid state	Pressing	1500 / 3
IEK-S2			1500 / 12
CPT-D1	Spray Pyrolysis		1500 / 15
CPT-D2			1500 / 15
Porous			
CPT-P-25	Spray Pyrolysis	Tape casting	1500 / 3
CPT-P-26			
CPT-P-29			

Porous LWO54 was manufactured by tape casting technique. Three batches of materials with different porosity that was achieved by varying the pore former (rice starch) amount in the slurry were tested. The aim of this set of experiments was to investigate the effect of porosity on strength at room temperature. Due to rather small thickness (average thickness was 330 μm in green state and ~260 μm after sintering) ball-on-3-balls test was found to be the most suitable test for the determination of biaxial strength. Since every technique requires different specimen geometry, details on samples are presented separately in the relevant sections.

Since solid state synthesis in laboratory scale cannot provide adequate material, for membrane manufacturing, it was decided in the frame of the Membrain Project that commercially available powder produced by spray pyrolysis (Cerpotech, Norway) would be used for the membrane support manufacturing by tape casting technique. Nevertheless, the powder produced by the optimized solid state reaction route which can derive high purity single phase material with the desired La-W ratio will be used as the coated membrane layer. For the mechanical characterization samples from both powder production routes were used. The parameter of major importance was the grain size and the porosity. For dense material produced by both powder types the elastic modulus was characterized by impulse excitation, indentation and ring-on-ring testing. Also these dense materials were assessed with respect to their creep behavior.

In case of porous material which will provide the mechanical properties as the membrane support, ball on 3 balls tests were applied for determination of the porosity effect on strength. The elastic modulus for porous material could not be measured using Ball on 3 ball measurement set-up, since deflections were not assessed because the specimens were too thin and very light.

5.1.4 NWO55

$Nd_{5.5}WO_{12-\delta}$ (NWO55) samples were provided by University of Valencia (Instituto de Tecnología Química). The synthesis and the bar manufacturing of $Nd_{5.5}WO_{12-\delta}$ samples are as follow:

The preparation method is based on the citrate-complexation route modified in order to stabilize W- and Ln-containing ions in the solution. Nd_2O_3 (Aldrich, 99.9%) was dissolved in concentrated hot nitric acid (65% vol.) in stoichiometric proportion and the resulting nitrate was complexed using citric acid at a molar ratio 1:2 cation charge to citric acid. Another solution was prepared using ammonium tungstate (Fluka, >99%) and complexing it with citric acid (Fluka, 99.5%) at the same ratio. Metal complexation in both cases was promoted by heat treatment at 120 ºC for 1 h. Both solutions were neutralized by controlled addition of ammonium hydroxide (32% wt.) and mixed at room temperature. The resulting solution is gradually concentrated by stepwise heating under stirring up to 150 ºC and followed by foaming.

The resulting thick foam product was subsequently calcined in air to eliminate carbonaceous matter and favor the mixed oxide crystallization. The minimum calcination temperature to attain this was around 700 ºC for 10 h.

The bar samples were prepared using the NWO55 material calcined at 900 ºC for 10 h and uniaxially pressed at 100 MPa. The green geometry of the bars was 40x5x4 mm^3. The samples were sintered in air at 1550 ºC for 5 h.

5.2 Microstructural characterization techniques

5.2.1 X-Ray diffractometry (XRD)

X-ray diffraction (XRD) is a non-destructive technique for the qualitative and quantitative analysis of the crystalline materials, in the form of powder or solid. The basic principle of XRD is the "reflection" of an X-ray beam from a family of parallel

and equally spaced atomic planes, following Bragg's law: When a monochromatic X-ray beam with wavelength λ is incident on lattice planes, diffraction occurs if the path of rays reflected by successive planes (with distance d) is a multiple of the wavelength. The XRD principle is illustrated in the following figure:

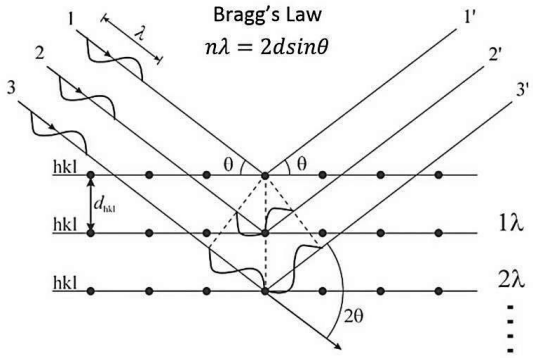

Figure 5-1 X-Ray Diffraction principle, Bragg's law [222].

X-Ray diffraction is used for the phase composition analysis. The diffractometer (D5000, Siemens) was equipped with X-ray tube with copper anode (λ = 1.5418 Å), an accelerating voltage 40 kV and a current 40 mA were used. Phase identification was carried out with ICDD PDF2-Database (Release 2004) and X'Pert Highscore Plus (PANalytical B.V.).Crystal structures were obtained from the Inorganic Crystal Structure Database (ICSD). The TOPAS program (Bruker AXS GmbH,) was used for the quantitative phase analysis and lattice parameter determination.

High temperature XRD (HT-XRD) was performed for BSCF and ST·F50 materials. Depending on the desired investigation, different conditions were applied for each material. In case of BSCF the aim of the investigation was the formation and dissolution rate of the hexagonal phase during a typical creep test. Therefore, a heating and subsequent cooling thermal cycle (heating/ cooling rate 0.1 K/sec, dwell step at each temperature 30 min) was applied. Pre-annealing was skipped in order not to alter the hexagonal phase amount.

In case of ST·F50 compound, the aim of the investigation was to determine the behavior of the material in the two atmospheres (air and vacuum) similar to the creep test. Therefore, the sample was initially heated up to 950 °C and cooled down to room temperature. Then the measurement was started for a new heating / cooling

thermal cycle like following: stepwise heating in air (pO_2 ~ 0.21 bar) up to 950 °C, 30 min dwell time to equilibrate and then cooling with 1 K / min to room temperature. XRD patterns were taken for each 50 °C step. The same thermal cycles were repeated in vacuum atmosphere (pO_2 ~ 10^{-2} bar).

5.2.2 Microscopy

Scanning electron microscope (SEM) produces images of a sample by scanning it with a focused beam of electrons. The electrons interact with atoms in the sample, producing various signals that are detected and contain information about the sample's surface topography and composition. The principle is illustrated in Figure 5-2:

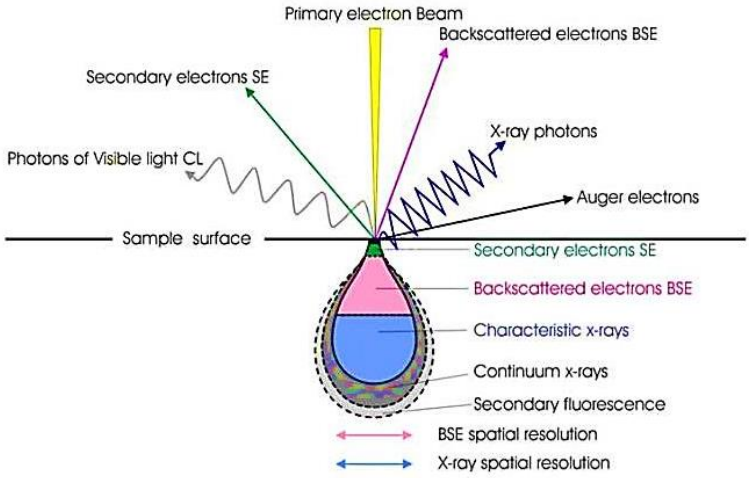

Figure 5-2 SEM operational principle [223].

Electron Backscattered Diffraction (EBSD) is a SEM-based technique that realizes the characterization of the microstructures of crystalline samples, by acquiring and automatically indexing electron backscattered (Kikuchi) patterns. With their high-intensity field-emission electron sources, SEMs equipped with EBSD detector can acquire and index tens to hundreds of Kikuchi patterns per second. Thus high-resolution EBSD maps are derived. Features of microstructure such as crystal orientation, grain size, global and local texture, recrystallize / deformed fractions, grain boundary characterization, slip system activity are also studied [224].

Light Microscopy (LM: Axiomat, Zeiss) and Scanning Electron Microscopy SEM (LEO 440, Zeiss SUPRA 50 VP) on cross-sections prepared by ceramography was used for the microstructure investigations. The detailed preparation steps are described in the following paragraph. Elemental analysis was carried out by energy-dispersive X-Ray spectroscopy (EDS, Inca, Oxford). EBSD patterns were obtained on a Carl Zeiss Merlin fitted with the Oxford Instruments' Nordlys II EBSD detector while the Aztec 2.4 software was used for grain size analysis and grain orientation mapping. The grain size was evaluated by ECD method similar to other materials.

Specimens were embedded in epoxy resin and ground with silicon carbide abrasive paper by subsequent steps with decreasing size of abrasive particles (from 400 to 4000 grit) followed by polishing using diamond paste with grain size from 6 µm to 0.25 µm for 30 min each. For grain size analysis the epoxy resin was removed and the polished sections were thermally etched for 20 min to 1 hour 100 °C lower than the sintering temperature. Thermal etching time depends on the grain size since smaller grains require longer etching until all grain boundaries were visible. For the materials with secondary phases segregated in grain boundaries, polishing was made with diamond paste up to 3 µm. Finally, for the samples tested by EBSD the final polishing step was performed with silica suspension in order to slightly etch the surface and achieve better contrast. In general, each material requires optimization of the ceramographic preparation that also depends on the desired investigation.

Porosity and grain size were graphically analyzed with the AnalySIS Pro® software using the planimetric method. The results of grain size analyses were recalculated into the diameter of a circle having an identical area. Then the measured grain was given as equivalent circular diameter (ECD) in µm. Porosity was evaluated by measuring the total pore area on microstructure images and divided by the total investigated area yielding the porosity percentage in the material. EBSD was applied for the grain size estimation of ST·F100x materials and grain orientation investigations of the perovskite materials.

Fractographic analysis was performed on fractured specimens after mechanical tests. Fracture origins were identified using a stereoscope (Olympus SZH10) and SEM (Zeiss SUPRA 50VP). The fractured surface should have suitable size, be

cleaned of any organic residues, and mounted on a specimen holder for viewing in the SEM.

5.3 Mechanical Characterization techniques

In the following sessions the applied mechanical tests, the experimental procedures as well as the subsequent evaluation methods are described in detail and the theoretical background is introduced.

5.3.1 Depth sensitive indentation

The instrumented depth sensitive indentation allows the measurement of the penetration depth of the indenter into the material (h) as a function of the applied load P. The indenters are generally made of diamond. Often a Vickers pyramid indenter with an angle of 136° between the triangle faces is used. Indentation load-displacement curves are used to determine mechanical properties as outlined in DIN 50359 – 1 [225]. During measurement the force applied to the indenter tip and the indenter penetration depths are continuously recorded during loading and unloading. A typical load (*P*) – displacement (*h*) curve is then obtained (Figure 5-3). The indentation tests in the current work were performed with a Fischer HC100 micro-indenter according to guidelines listed in ASTM C1327-08 [226]. The range of indentation loads varies from 10mN to 1000mN.

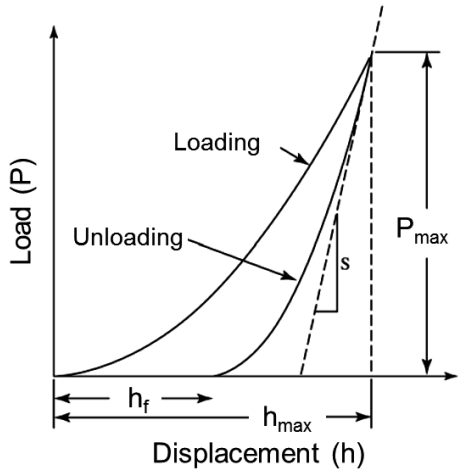

Figure 5-3 a) Schematic representation of load (P) -displacement (h) data for a depth sensing indentation experiment.

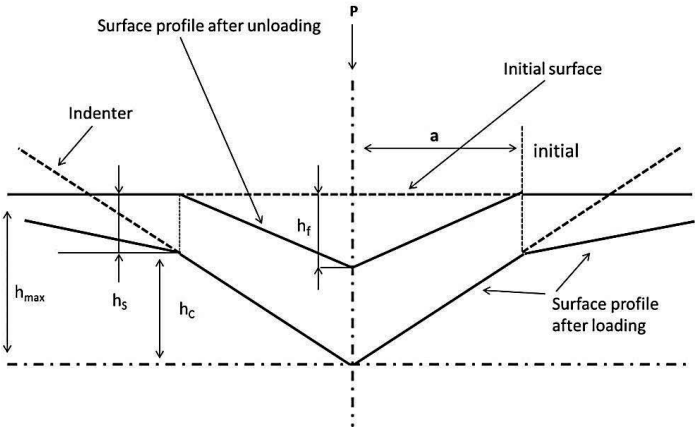

Figure 5-4 Main parameters used in analyzing unloading vs. indenter depth curves.

The elastic modulus is obtained from the slope of the linear part of unloading curve *S*, at the point of maximum load using the following equations [227,228]:

$$E_r = \beta \cdot \frac{\sqrt{\pi}}{2} \cdot \frac{S}{\sqrt{A_c}}$$ Equation 5-1

Where A_c is the projected contact area (obtained via calibration), β is a correction factor that depends on the geometry of the indenter ($\beta = 1.0124$ for Vickers indenter), *S* is the unloading slope ${}^{dP}/_{dh}$ and E_r is the reduced elastic modulus. *E* of the indenter tip is not infinite; therefore, the elastic modulus E_i is then derived from:

$$E_{IT} = \frac{1-\nu^2}{\frac{1}{E_r} - \frac{1-\nu_i^2}{E_i}}$$ Equation 5-2

Where E_i is the elastic modulus of the indenter, ν and ν_i are Poisson's ratios of the tested material and indenter, respectively [229]. The results obtained from this method can possess a rather large scatter in case of low surface quality or inhomogeneity effects. Moreover, the projection area A_p of the indentation imprint should be calculated for the determination of E_{IT} and micro-hardness H_{IT}. It is derived from the unloading slope according to $A_c = 24.5h_c^2$, where: h_c - is the contact depth (Figure 5-4). Additional terms are normally added to calibrate the indenter shape.

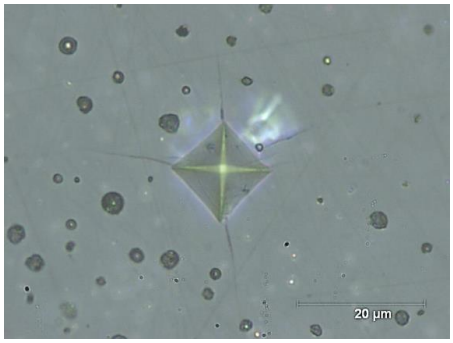

Figure 5-5 Typical Indentation imprint of LWO54 at 1N.

Micro-hardness of plastic materials is calculated according to the equation:

$$H_{IT} = 1.8544 \frac{P_{max}}{d^2} = 1.8544 \frac{P_{max}}{49h_{max}^2}$$ Equation 5-3

where H_{IT} indentation micro-hardness P_{max} peak load, d length of impression's diagonal and h_{max} the depth at peak force [230].

Indentation fracture toughness

Besides the elastic modulus E_{IT} micro-mechanical representative properties like micro-hardness H_{IT}, and fracture toughness of single grains and phases were investigated with the depth-sensitive indentation test method [228]. The fracture toughness of the material is derived from the length of cracks induced by indentation (Figure 5-5). Depending on the indentation crack geometry, several equations that correlate the size of the indentation crack with the fracture toughness are reported in literature [231]. In the current work, the equation proposed by Niihara [232] (Equation 5–5) was applied for indentation toughness determination in $MPa \cdot m^{1/2}$, based on impressions carried out with a load of 1 N. Like it was discussed in chapter 4.3, at lower loads, Palmqvist propagation of indentation cracks is more likely to be observed. In that case, indentation toughness was determined as following:

$$K_{IC} = 0.018 \left(\frac{E}{H_{IT}}\right)^{0.4} H_{IT} \alpha^{0.5} \left(\frac{l}{\alpha}\right)^{-0.5} \quad \text{Equation 5-4}$$

Where a half of imprint's diagonal length, l crack length measured from the end of the imprint.

For higher loads, radial or half-penny crack systems are typical and K_{IC} in $MPa \cdot m^{1/2}$ can be derived from the Anstis [233] equation when $c/\alpha \geq 2$ is fulfilled:

$$K_{IC} = 0.016 \cdot \left(\frac{E}{H_{IT}}\right)^{0.5} \cdot \left(\frac{P}{c^{1.5}}\right) \quad \text{Equation 5-5}$$

Where P is the indenter load, *c* the distance from indent center to the end of radial crack

E_{IT} and H_{IT} were measured for all materials with Fischer scope micro-indenter by applying a load of 1000 mN for a matrix of 8 x 8 indentations of equal distance at 3 - 5 times the indent diagonal in order to avoid effects of crack pattern as well as plastic zones of neighboring indents. Fracture toughness was also determined for load of 1 N.

For this test small pieces of materials with various dimensions but with minimum 2x2 mm^2 surface were used. Specimens were prepared by ceramography as

described earlier in order to obtain parallel and flat surfaces with minimum roughness.

5.3.1 Impulse Excitation technique

In this test, the fundamental resonant frequency of specimens of suitable geometry is measured by exciting them mechanically using a singular mechanic strike. A transducer, i.e. a non-contacting microphone, senses the resulting mechanical vibrations of the specimen and transforms them into electric signals. The entire oscillation waveform after excitation is recorded and by the use of the appropriate fundamental resonant frequencies, specimen dimensions and mass the dynamic elastic modulus can be calculated. Procedure and analysis are outlined in ASTM E 1876 – 01 [234]. Young's modulus, shear modulus, Poisson's ratio and damping coefficient are determined with this technique. The main advantage of this method over static methods (i.e. bending, indentation) is that the stresses remain far below any plasticity limit. The experimental set-up is shown in Figure 5-6.

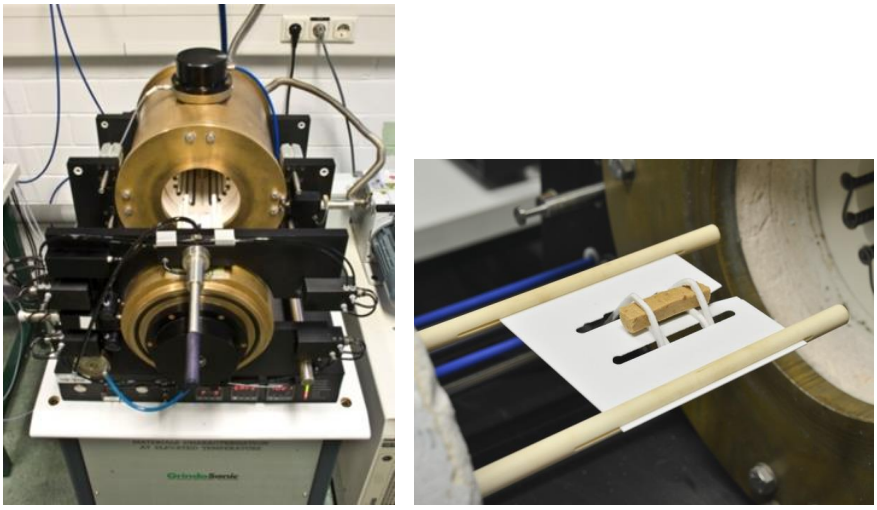

Figure 5-6 Impulse Excitation setup and test configuration.

Impulse excitation technique enables measurements of Young's modulus from room temperature up to 1000°C under different atmospheres such as air, N_2 and Ar / 4% H_2 gas mixture.

E, shear modulus G and Poisson's ratio ν are linked with the following equation.

$$G = \frac{E}{2 \cdot (1+\nu)}$$ Equation 5-6

Bar and disc shaped specimens are used for the impulse excitation technique. Both geometries show characteristic modes of vibration depending on boundary conditions such as the support points and type as illustrated in Figure 5-7:

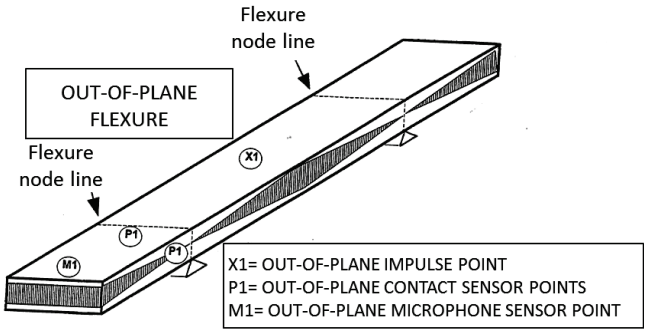

Figure 5-7 A schematic representation of a rectangular bar sample used to measure elastic modulus by impulse excitation technique for flexural vibration [234].

Given the flexural and torsional frequencies, Young's moduli are derived from equation:

$$E = 0.9465 \cdot \left(\frac{m \cdot f_f^2}{b}\right) \cdot \left(\frac{l^3}{t^3}\right) \cdot T$$ Equation 5-7

Where f_f denotes the flexural frequency, m mass, l length, b width of sample and T a correction coefficient. Factor T is a complex algebraic term that depends on the Poisson's ratio, the thickness and length of the test specimen. If $h/l \geq 20$, then T can be simplified to:

$$T = 1 + 6.585 \cdot \left(\frac{h}{l}\right)^2$$ Equation 5-8

Dense LWO54 was tested with impulse excitation technique (GrindoSonic J.W. Lemmens N.V, Belgium) in order to investigate the effect of temperature and atmosphere on E. Heating and cooling rates were 5 K / min. Measurements were performed in air and in gas mixture Ar / 4% H_2.

Table 5-2 List of dense LWO54 samples tested with Impulse Excitation technique

Sample	Dimensions		Testing conditions
	m (gr)	$l * b * t$ (mm^3)	
IEK1-S2	3.40	$32.20 * 4.08 * 4.15$	RT- 1000°C in air Heating/ cooling rate: 5 K/min
IEK1-S2	3.40	$32.20 * 4.08 * 4.15$	RT-1000°C in Ar / 4% H_2 Heating/ cooling rate: 5 K/min
CPT-C2	2.72	$32.15 * 3.91 * 3.39$	RT- 1000°C in air Heating/ cooling rate: 5 K/min

5.3.2 Bending Experiments

Bending experiments were performed on an electromechanical test machine (Instron 1362). The central displacement of the specimens was measured by a sensor in contact with the lower (side in tension load) surface of the sample. The displacement was monitored with a ceramic extension rod attached to a linear variable differential transformer (Sangamo, LVDT, range ± 1 mm with precision ± 1.25 µm). The load was applied with a 1.5 kN load cell (Interface 1210 BLR). Two different bending techniques were used, ring-on-ring test and ball-on-3-balls test. The experimental setups are illustrated in Figure 5-8 and Figure 5-9, respectively. In case of ring-on-ring test, a half-sphere was used for the loading set-up in order to assure the alignment and eliminate uncertainties and scattering of obtained results (Figure 5-8). For the ring-on-ring test disc-shaped specimens were used, while for ball-on-3-balls disc as well as rectangular-shaped samples were tested. Tests were carried out from room temperature up to 1000 °C. The temperature was monitored close to the specimen surface with a type K thermocouple.

Two bending test types were applied for the determination of the mechanical properties of LWO54. E and σ_f in air, at room temperature and at higher temperatures were determined for dense LWO54 material with ring-on-ring test. Three batches of disc-shaped specimens were provided from IEK-1. One batch was produced using powder from solid state synthesis and the other two from commercial powder (Cerpotech) produced with spray pyrolysis. More details of the preparation of these batches were presented in previous chapter. The aim of the experiments was to see the effect of different powder characteristics and sintering conditions on E and σ_f.

Ball-on-3-balls tests were applied for the determination of strength of the porous LWO54 material manufactured by tape casting technique. The benefit of this test is that the flatness of the sample does not have impact on the fracture stress determination as described below. The manufacturing process of the porous LWO54 material revealed challenges due to very active sinterability that led to bended and wavy surfaces. Further preparation of these samples for ring-on-ring test was restrained by the low thickness of the specimens (up to 300 µm). Moreover, strength tests and subsequent fractography analysis could support the optimization of the manufacturing process. Tests were performed at room temperature in the Institute for structural and functional ceramics, at Montanuniversität Leoben, Austria. In collaboration with this department, the ball-on-3-ball test configuration was developed in IEK-2 using Al_2O_3 substrate and Si_3N_4 balls so that measurements for energy application relevant conditions could be performed at temperatures up to 1000 °C (Figure 5-10) and different atmospheres such as vacuum, N_2 and Ar / 4% H_2. Calibration with different materials (glass and tape casted MgO) at room temperature were successively performed. However, there was an equipment related limit in IEK-2, regarding to the fracture load of the tested materials; it should exceed the fracture load limit of 2 N at room temperature in order to be accurately measured. Therefore, the measurements were performed in Leoben for the currently developed materials. Samples were provided by IEK-1 in disc-shape and then cut in ZEA-1 (Zentralinstitut für Engineering und Technologie, Forschungszentrum Jülich GmbH) in rectangular shape of smaller size, so that tests fulfill the ISO criteria regarding specimen geometry and the required amount of specimens for Weibull statistics as described below.

5.3.2.1 Ring-on-ring bending test

a) Test procedure and general evaluation

The ring-on-ring experimental set-up is illustrated in Figure 5-8. In this test, a loading ring bends a thin disc vertically while it is being restrained by a supporting ring. The linear bending theory is applied for the determination of fracture stress since brittle ceramic materials usually fail after mainly elastic deformation. In the area inscribed by the smaller ring exists an equi-biaxial tensile stress state and here initialization of fracture is expected.

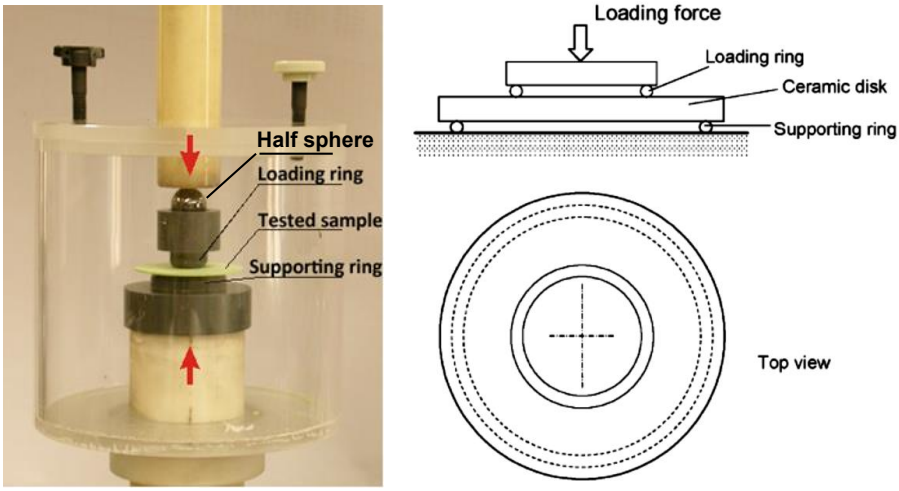

Figure 5-8 Experimental set-up of ring-on-ring bending test.

The elastic modulus is derived from the linear part of the load displacement curve (at low loads a non-linearity in the curve might be observed due to the specimen's unevenness) after ASTM C1499-05 [235,240].

$$E_{RoR} = \frac{3 \cdot (1-\nu^2) \cdot r_1^2 \cdot \Delta F}{2\pi \cdot \Delta f \cdot h^3} * \left[\left(\frac{r_2}{r_1}\right)^2 - 1 - ln\left(\frac{r_2}{r_1}\right) + \frac{1}{2}\left(\frac{1-\nu}{1+\nu}\right) * \left(\frac{r_2^2 - r_1^2}{r_3^2}\right) * \left(\frac{r_2^2}{r_1^2}\right)\right]$$

Equation 5-9

Where ΔF is the difference in force and Δf is the corresponding change in displacement in the linear part of load-displacement curve, h is the specimen thickness, r_1, r_2 and r_3 are radius of loading ring, supporting ring and specimen, respectively.

For linear behavior, as it might be expected for brittle fracture, the maximum stress is constant over the tensile loaded surface inscribed by the loading ring:

$$\sigma = \frac{3F(1+\nu)}{2\pi \cdot h^2} \cdot \left[ln\left(\frac{r_2}{r_1}\right) + \left(\frac{1-\nu}{1+\nu}\right) \cdot \left(\frac{r_2^2 - r_1^2}{r_3^2}\right)\right]$$

Equation 5-10

where F is the applied force.

The ring-on-ring bending test assures the uniform distribution of the stress in the central part of the specimen above the loading ring far from the edges where usually machining defects exist [236].

The most used approach to describe the strength distribution of a ceramic is the Weibull distribution as described earlier in chapter 4.2. The fracture stress data σ that obtained experimentally were used to determine the characteristic strength σ_0 and the Weibull modulus w. By taking the natural log on both sides, the Weibull equation is rewritten as:

$$ln\sigma_0 = ln\sigma + \frac{1}{w} ln\left\{ln\left[\frac{1}{1-P_f(V_0)}\right]\right\} \qquad \text{Equation 5-11}$$

that yields a straight line according to a linear equation $y = ax + b$ with X axis representing the $ln\sigma_0$ and the Y axis $ln\left\{ln\left[\frac{1}{1-P_f(V_0)}\right]\right\}$. The slope yields the Weibull modulus w. The stresses should be ranked in ascending order with specific probabilities of $P_f(\sigma_i) = \frac{i-0.5}{N}$ where i is the ranking number and N the number of tested samples. The procedure described is according to ASTM C1239-07 [159]. A loading rate of 100 N/min was used in order to minimize potential influence of stable crack growth on strength [237].

Characteristic strength was recalculated for the same size of discs according to the equation:

$$\frac{\sigma_2}{\sigma_1} = \left(\frac{V_1}{V_2}\right)^{\frac{1}{w}}$$

since the failure probability depends on the tested effective volume or area depending if volume or surface defects are failure relevant.

Effective volume is calculated for ring-on-ring test according to ASTM C1499-05 [238,239]:

$$V_{eff,specimen} = \left(\frac{\left(2\pi r_1^2\right)t}{2(w+1)}\right)\left(1+\frac{44(1+v)}{3(w+1)}\frac{w+5}{w+2}\right) \times \left(\frac{r_2-r_1}{2r_1r_3}\right)^2 \frac{8r_3^2(1+v)+4(r_2-r_1)^2(1-v)}{(3+v)(1+3v)}$$

Equation 5-12

The specific average dimensions of the samples as well as the specimen number of the different tested batches are summarized in the following table. Sample dimensions were according to DIN 51105:2010-08 [240]. Prior to the test samples that showed irregular surface quality were grinded and polished in order to achieve flat and parallel surfaces as well as homogeneous thickness along the discs also according to DIN 51105:2010-08.

Table 5-3 Specimen geometries and testing conditions for the ring on ring test for the dense LWO54 material.

Material	Diameter $\tilde{D}$ [mm]	Thickness $\tilde{h}$ [mm]	Number of samples *N*	r/R [mm]	Load rate N/ min	Temperature [°C]
IEK1-S2	21.35	1.706	13	3.95 / 7.5	100	RT, air
CPT-D1	21.01	0.790	3		1	RT, air
	20.97	0.770	9		100	
	21.02	0.750	3		1000	
	20.95	0.783	6		100	400, air
	20.90	0.755	3			600, air
	20.95	0.788	3			800, air
	20.95	0.740	3			1000, air
CPT-D2	21.57	0.545	9		100	RT, air
	21.58	0.544	3			400, air
	21.55	0.544	3			600, air
	21.58	0.543	3			800, air
	21.75	0.740	3			1000, air

5.3.2.2 Ball-on-3-balls bending test

In ball-on-3-balls test the bottom side of a disc specimen is supported by three balls, which are in equal radial distance from the center, while the fourth ball applies the load in the central point of the upper side of the disc until the fracture of the sample. The fracture load is measured. The test is standardized in ASTM F 394-78 [241]. In general, sintered discs and rectangular samples with no special finishing can be

tested, allowing a quick testing procedure. The configuration is described below and it is illustrated in Figure 5-9 and Figure 5-10:

The maximum principal stress is located on the disc surface opposite to the loading ball. It has been shown that the stress depends on the applied load and geometric set-up of the test, which includes the dimensions of the disc: thickness and diameter, size and positions of the balls and elastic properties of ball and disc material [242]. In another study of the same group, the stresses were analyzed for a wide range of loading geometries to analyze their influence proving that the test is very stable against errors in the geometry of specimens as well as the loading device, while the most sensitive parameter is the thickness of the specimen. Other parameters such as misalignment, small deviations of the threefold geometry or some buckling and wrapping of the specimens have only little effect on the measured maximum strength of the disc [243]. Therefore, the testing procedure can easily be miniaturized since specimens with a volume less than 1 mm^3 could be successfully tested [244].

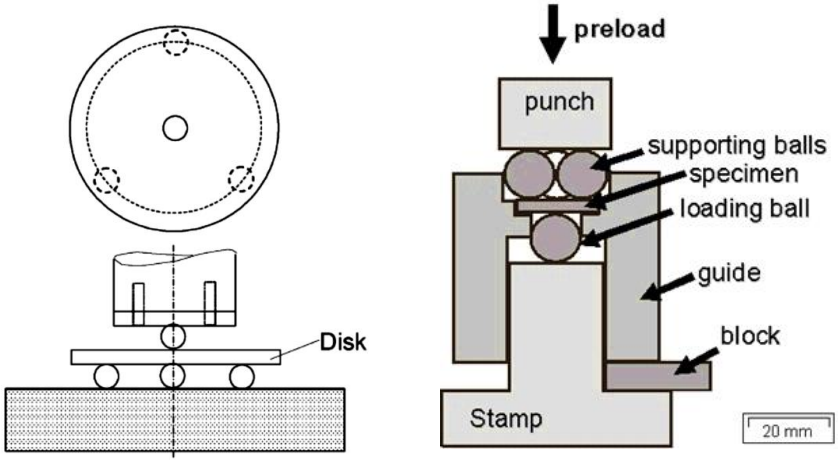

Figure 5-9 Shematic illustration of experimental set up for ball-on-3-ball test.

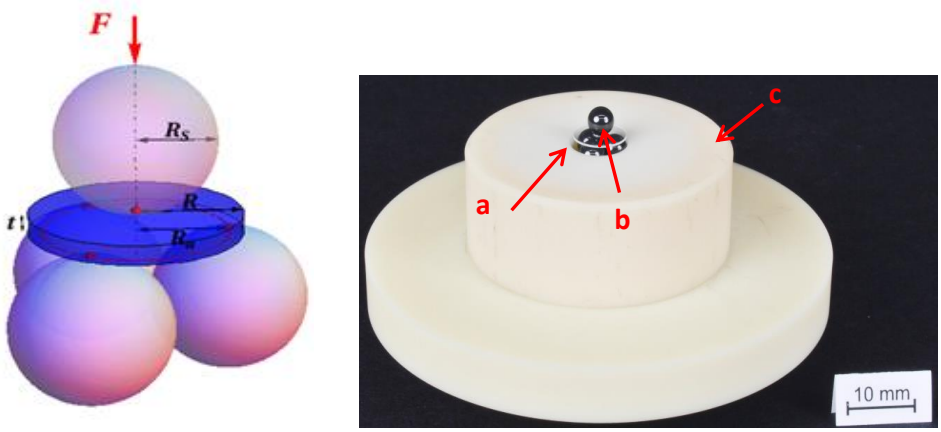

Figure 5-10 Left) Configuration of balls right) ball-on-3-ball configuration developed in IEK-2 where a) is glass specimen, b) Si_3N_4 balls and c) Al_2O_3 jig.

The fracture load is measured and the strength is estimated according to the following numerical solution, assuming that all balls have the same size, are made of the same material and all supporting balls are in contact.

$$\sigma_{max} = f\,(\alpha, \beta, v) \cdot \frac{F}{t^2}$$ Equation 5-13

$$\alpha = \frac{t}{R}\ ,\ \beta = \frac{R_a}{R},\ R_a = \frac{2R_s}{\sqrt{3}}$$ Equation 5-14

Where F is the fracture load in N, t the thickness in mm, f a dimensionless factor that is given as function of the disc geometry t/R, the support geometry R_a/R, and the Poisson's ratio of disc material *v*; its values range 0.2 - 0.4 [245]. R is the radius of the specimen in mm, R_a the support radius that depends on R_b, the radius of the supported balls [246]. The first principal stress σ_{max} is in the center of the top plane, where the stress is biaxial. The function f is analyzed and published in [247] for the parameter range:

$$f = 0.366631 + \frac{\left(2.62749 + 27.2083 * \left(\frac{t}{L}\right) - 51.5632 * \left(\frac{t}{L}\right)^2 * (1 + 0.996214 * v)\right)}{1 + 30.859 * (\frac{t}{L})}$$

Equation 5-15

Where L is the specimen width (L= 4 mm). Equation 5-15 permits small variations in the thickness of each specimen to be taken into account. For a typical LWO54 sample with t = 0.260 mm thickness and a Poisson's ratio v = 0.24, the geometric factor resulted in f = 2.1

$$0.05 < \alpha = 0.6$$ Equation 5-16

$$0.55 < \beta < 0.9\ and\ 0.2 < \mu < 0.35$$ Equation 5-17

For the maximum stress the equation yields for disc- and rectangular- shaped discs, respectively:

$$\sigma_{B3B} = f \cdot \frac{F}{t^2}$$ Equation 5-18

$$\sigma_{B3B} = (3.3 - 2.7 \cdot t + 1.55 \cdot t^2) \cdot \frac{P}{t^2}$$ Equation 5-19

For the evaluation of results regarding the disc-shaped samples, an online web-mathematica platform was used [248] where the σ_{B3B}, pre-factor f and V_{eff} can be derived. For the evaluation of f and V_{eff} FEM simulations are required. Development

of own software and simulations studies in order to derive f pre-factor were beyond the scopes of this study.

The aim of these tests was to investigate the effect of porosity on the fracture strength of LWO54 tape casted material. Also, the experiments were designed for the investigation of temperature and atmosphere on the strength of porous material. Nevertheless, the method is limited for materials that exhibit fracture force over 2 N at room temperature, since a pre-load of 2 N needs to be applied for an effective measurement. Therefore, materials with fracture load below this limit already break before the measurement starts but still, samples with very low thickness can be effectively characterized. Ball-on-3-balls testing method was calibrated with testing material of MgO provided by IEK-1 (Fb=10N) and commercial glass DeSAG D263 (Schott Gruppe) with h ~ 0.145 mm. Moreover, LWO54 and MgO of the same batches were tested for comparison in Leoben, leading to similar values of F_b. The dimensions tested materials and the testing conditions are summarized below:

Table 5-4 Sample list for plate-shaped porous LWO54 tested with B3B method at RT

Material	Number of specimens N	Dimensions	Thickness	Testing conditions
LWO54_CPT_S_25	29	3x4 mm^2	0.248±0.009	Pre-load 0.2 N, 13,8N/min
LWO54_CPT_S_26	14		0.254±0.003	
LWO54_CPT_S_29	29		0.239±0.002	

5.3.3 Creep

Creep tests were carried out on cylindrical and bar-shaped specimens, as they are described in Table 5-5. The sintered specimens were polished to obtain parallel end surfaces for compressive creep tests. The tested materials as well as the testing conditions are summarized below:

Table 5-5 List of samples tested for creep in compression

Material	Sample geometry, number of samples		Conditions
BSCF·Z100x	10, cylinders	~ 12.0mm Ø 6.0 mm	800°C-950 °C interval steps of 50 °C Stress 30, 63, air
ST·F100x	ST·F30, 3 bars	3.8*7.1*8.0 mm^3	800°C - 1000 °C, intervals of 50 °C Stresses 10 – 80 MPa, air, ST·F50 vacuum (10^{-2} mbar)
	ST·F50, 3 bars	4.0*4.0*13.0 mm^3	
	ST·F70, 2 bars	3.1*5.6*18.5 mm^3 3.0*5.9*12.2 mm^3	
LWO54	IEK-S1, 1 bar	3.3*4.2*12.0 mm^3	700°C - 1450 °C, intervals of 100 or 150 °C 20 -6 3 MPa, air, 900 – 1000 °C 20-100 MPa vacuum, Ar / H_2 4%, Ar / H_2 4% 2.5% H_2O Also samples with different grain sizes were measured under air
	IEK-S2, 1bar 1cylinder	3.9*4*13.9 mm^3 8.7 mm Ø 6.0 mm	
	CPT-D2, 2 bars	3.6*3.8*14.8 mm^3	
NWO55	1, bar	2.6*3.2*9.44 mm^3	900 - 1350 °C, intervals of 100 or 150 °C, 10 – 63 MPa, air

Creep tests were performed in compression mode using an INSTRON 1362 electromechanical testing machine equipped with high temperature furnaces. The experimental configuration is illustrated in Figure 5-12. In all cases, the flat sides of the samples were carefully grinded and polished prior to experiments in order to obtain parallel contact surfaces. The experimental set-up is illustrated in Figure 5-12. A linear variable differential transducer (LVDT, Sangamo, range ± 1 µm, precision 1.25 µm) located in the lower part of the loading machine, was used to measure the traverse displacement. The LVDT was assembled with the bottom of the half-sphere in the clamping device by an alumina rod so that the position change of the lower traverse relative to the upper specimen fixture was measured yielding information of the sample deformation. All tests were performed in constant stress mode at constant temperature steps according to the general heating and loading profile illustrated in Figure 5-11. An annealing step was applied in beginning of each experiment for several hours in order to obtain thermal equilibrium of materials and to minimize chemical expansion effects as suggested by Rutkowski [249]. Also before each isothermal step an additional annealing period of 1 h was applied for minimizing thermal expansion effects of the testing machine that might affect the measured deformation rate. In some cases, cooling steps were also applied for the determination of creep rates. In all cases, each creep measurement was terminated

after 24 h of steady-state deformation or until an integral deformation of 100 µm was reached.

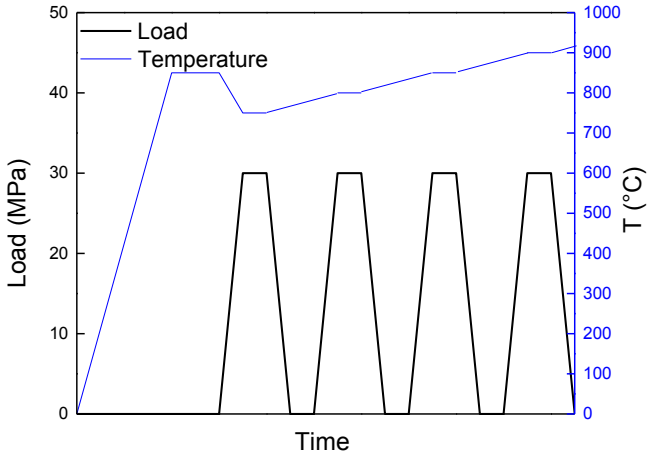

Figure 5-11 Typical heating and loading profile for compressive creep tests in constant load mode.

The applied force was measured with load cells of 10 kN (Interface, 1210 ACK) and 1.5 kN (Interface, 1210 BLR) measurement range in air and under vacuum (pO_2 10^{-2} bar) or mixed gas atmosphere (Ar / 4% H_2 or Ar / 4% H_2 & 2.5 % H_2O), respectively. Data concerning temperature, stress and deflection during the tests were collected with a sampling rate of 0.5 Hz.

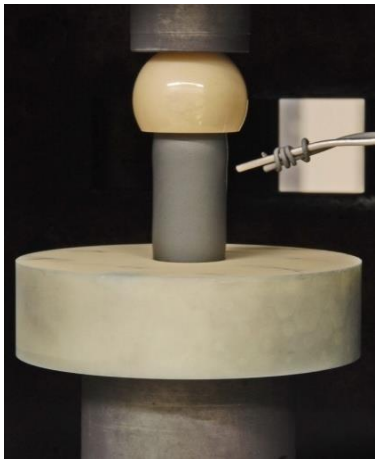

Figure 5-12 Setup for compressive creep test. The specimen is mounted between Al_2O_3 table and half sphere.

The strain for all materials was calculated from the ratio of measured displacement Δh and initial height h_0:

$$\varepsilon = \frac{\Delta h}{h_0}$$ Equation 5-20

In Figure 5-13a, a typical time vs. strain curve is presented. Two regions can be distinguished that can be attributed to the primary and secondary creep stage. The creep rate should be determined from the slope of the secondary creep stage (minimum creep rate). It was shown by Rutkowski [249] that fitting of 2nd order polynomial yielded more accurate results than linear fit.

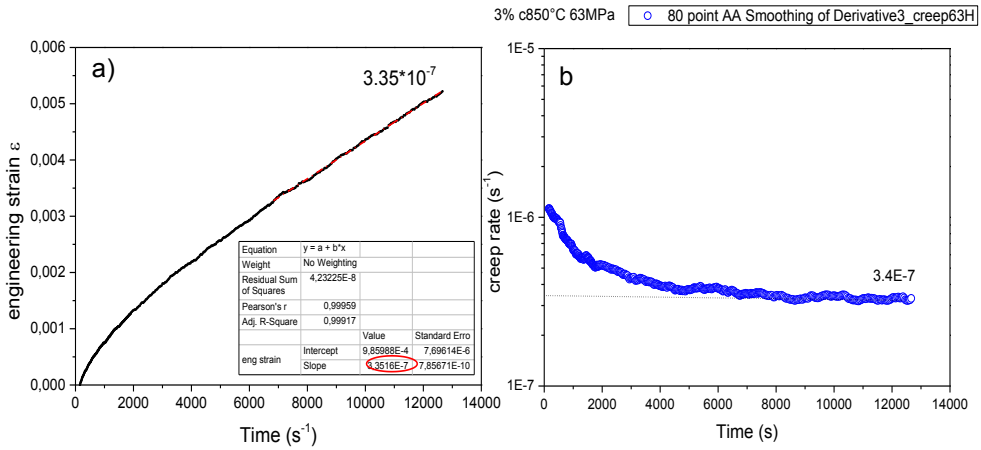

Figure 5-13 Typical strain-time curve for BSCF·Z3 at 850°C for cooling sequence at 63MPa. Minimum creep rate is determined in a) by linear fitting from the linear part of the curve b)by differentiation of strain.

Aiming at an improvement of previously used analysis procedures that are mainly based on a subjective assessment of the secondary creep range, in the current study the steady state creep rate was determined by plotting the moving average $\dot{\varepsilon}$ as derived via differentiation of the data vs time as shown in

Figure 5-13. Tertiary creep stage was not observed in any of the experiments. Moreover, especially for the temperature were deformation rates of the materials were close to the sensitivity limit of the experimental set-up longer testing time was applied not only to reduce the effect of background noise but also to minimize the potential influence of primary creep [254]. In all cases, the engineering strain was applied for the determination of creep rate, since the total strain did not exceed 10% and yielded values close to the true strain. Creep ratio in compression is independent for length to diameter ratios of 1.5 to 2.5 for cylinders according to Poteat et al. [250]. Beyond these limits, barreling or buckling can occur. Nevertheless, barreling, cracking or buckling effects, that would lead to change of the cross sectional area, were not observed after the tests. Thus, the deformation of specimens can be considered homogeneous. The stress exponent *n* was determined for several constant stress steps at one temperature in order to see if there is potential influence of threshold stress. Such an effect was not observed in any case. Subsequently, the obtained creep rates were applied to Equation 4 – 11 for the determination of creep parameters via multi-linear regression. By plotting the natural logarithm ln of the

steady state creep-rate $\dot{\varepsilon}$ versus $\ln \sigma$ at constant temperature T, n is determined as the slope in the plot. The activation energy Q_a can be calculated from the slope of the $\ln \dot{\varepsilon}$ vs reciprocal of the absolute temperature $1000 / T$ at constant stress according to Arrhenius approach, while the inverse grain size exponent p is the slope of the $\ln \dot{\varepsilon}$ versus $1/d$ curve. Finally, by plotting $\ln \dot{\varepsilon}$ versus $\ln pO_2$, the partial oxygen exponent m is derived.

The exact testing conditions of each material are described in the following paragraphs.

BSCF·Z100x

In these series of experiments the comparison of the doped materials with the reference BSCF5582 was in focus. More precisely, the possible suppression of hexagonal phase, thus the shift of the related cubic-to-hexagonal effects like the hysteresis to lower temperatures was the main aim of these investigations. Thus, the suggested heating profile by Rutkowski [249] was applied to enable direct comparison of the data. A typical BSCF·Z100x test run was conducted in the temperature range from 800 to 950 °C, which corresponds to 0.65 $T_m \leq T \leq 0.78\ T_m$ (melting temperature T_m = 1290 °C for BSCF [251]). For BSCF·Z100x, prior to testing, the samples were pre-annealed at 850 °C for 24 h to ensure chemical equilibrium and eliminate associated strains. Subsequently, the sample was cooled down with a rate of 8 K/min to the first (i.e. lowest) measuring temperature. The temperature was incremented stepwise, with 50 K intervals, using heating and cooling rates of 8 K/min. At every measurement temperature, the sample was allowed to equilibrate for 1 h before the actual load was applied. Applied loads were 30 and 63 MPa. All tests were performed in ambient air. In order to investigate the effect of doping on the creep mechanism, constant stress steps were applied for each tested temperature as illustrated in the typical heating-loading profile in Figure 5-11. Since the number of samples was limited and extensive studies had already been performed for the BSCF5582 reference material, no experiments for the evaluation of inverse grain size exponent or oxygen partial oxygen exponent were performed. Finally, in the case of extreme Zr doping, BSCF·Z10, a different heating profile was applied in order to investigate the effect of highest doping level on the cubic-to-hexagonal phase transformation as well as the governing creep mechanism.

ST·F100x

The main focus of these experiments was the determination of the creep rates and the governing creep mechanism at the operation related temperatures that correspond to 0.49 ≤ T/T_m ≤ 0.54 (T_m=1900°C for $SrTiO_3$ [252]). STF50 was tested up to 1000°C as example material for the more accurate determination of activation energy. While the heating-loading profile that was applied follows the one described above, some modifications were made in comparison to BSCF·Z100x series. The testing conditions of ST·F100x series include a very slow heating and cooling rate of 1 K/min in order to avoid crack formation related problems like they had been reported for sintering studies and permeation experiments. It seems that after densification the materials undergo a large expansion, due to heterogeneous phase equilibria that produce oxygen gas as reported for the $Sr(Fe,Co)_{3-\delta}$ [220]. According to previous studies of these materials regarding permeation, no phase changes are expected [66]. Therefore, only a short pre- annealing step of 5 h at 850°C was applied to ensure that the materials vacancy population would reach equilibrium at this temperature. The applied stresses were in the range of 10-80 MPa in order to determine the effect of stress on the creep rate. At every test temperature, the sample was allowed to equilibrate for 1 h before the actual load was applied. Also, the testing times were long enough to overcome possible chemical strain related effects that can affect the creep rates especially in the first 24 h of measurement as reported for BSCF5582 [249]. All tests were performed in air. Exemplary for all STF materials, a set of experiments was performed for STF 50 under different atmospheres (pO_2 200 mbar and 10^{-5} mbar) in order to derive the m exponent. Each step was applied until the secondary creep stage was achieved. Same heating and cooling profile was applied.

The strains were not large enough to yield any differences between true strain and engineering strain. Total strain after each experiment was much less than 10 %. The creep data for the STF materials are presented in detail in Appendix B.

LWO54

The aim of these experiments was again the determination of creep rates as well as the governing creep mechanism in the application relevant temperature range of 600 - 800 °C [3], corresponding to 0.39 ≤ T/T_m ≤ 0.48 (T_m= 1960 °C for La_6WO_{12}

[114]) which did yield measurable deformation. Therefore, measurements were carried out at higher temperatures (1050 – 1450 °C 0.59 ≤ T/T_m ≤ 0.77) with intervals of 50 K. Applied stresses were in the range of 20 - 80 MPa. Samples with different grain sizes were tested for the determination of grain size exponent. The experiments were carried out in air. The heating profile followed the typical ones described above. Heating and cooling rates were 8 K/ min. In these cases, the samples were heated to the highest temperature and subsequently cooled down to the lowest measuring temperature step. At every measurement temperature, the sample was allowed to equilibrate for 1 h before the actual load was applied. No secondary phases were observed during permeation experiments performed at IEK-1, the applied temperatures were high enough to obtain equilibrium and the measuring times were long so that deformation was not affected by potential chemical strain effects. Therefore, the pre-annealing step at an intermediate temperature was not essential and was skipped.

In order to investigate the effect of the environment on the creep rate, tests under vacuum (10^{-2} mbar), gas mixture Ar / 4% H_2 and humidified Ar / 4% H_2 with 2.5 % H_2O were performed. The thermal heating profile was applied (Figure 5-11). A pre annealing step was applied for 12 h at 900°C since H^+ protons are not inherently in the structure of the material, but are introduced from the environment as described in the theory part for the proton conducting transport mechanism. To enhance the absorption of the H^+ a thin Pt coating was applied which acts as a catalyst similar to permeation experiments. Coating was applied by sputtering (Balzers union SCD 040). It was found that this layer does not affect the creep rates of the material. In case of the Ar / 4% H_2 tests two different ways of supplying the gas were tested. Initially the gas was inserted into the chamber once (closed system) while in following experiments, the gas flow was continuous. The second case was found to be more applicable since leakage of the furnace was observed. Given that the experiments run for long period of time and the H_2 portion in the gas mixture is low, the testing conditions in the first case of closed system were not considered adequate for providing realistic creep rates.

NWO55

NWO55 was also investigated regarding creep behavior for comparison to LWO54 with respect to creep rates and governing creep mechanism. The experiments were performed in air, in the temperature range 900 °C – 1350 °C for stresses of 10 – 63 MPa.

6 Results and Discussion

6.1 BSCF·Z100x

6.1.1 Solid solubility limits and microstructure

Figure 6-1 shows XRD patterns of sintered samples collected at room temperature BSCF·Z100*x* before and after annealing at 850 °C in air for 336 h. Diffraction patterns of both series can be indexed using a cubic perovskite structure. In the patterns obtained for BSCF·Z10, peaks of a secondary phase can be assigned to $(Ba,Sr)ZrO_3$ [PDF 00-006-0399]. The peak at 27.8° obtained for pure BSCF can be assigned to hexagonal $Ba_{0.5}Sr_{0.5}CoO_3$ [PDF 99-000-0030]. The latter observation is consistent with previous reports [50,57], showing that cubic and hexagonal polymorphs may coexist in BSCF after annealing at 850 °C.

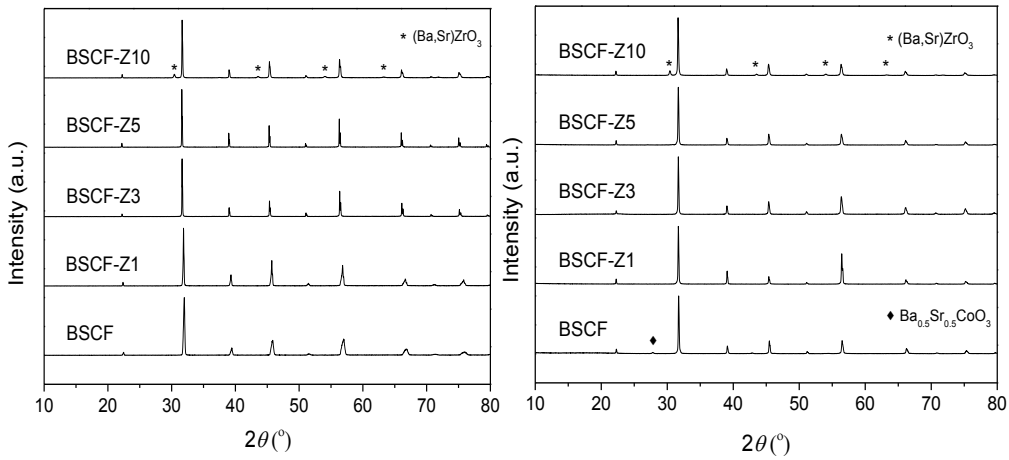

Figure 6-1 XRD patterns of sintered compacts of BSCF-Z·100x (left) before and (right) after annealing in air, at 850 °C, for 336 h. Reflections for $(Ba,Sr)ZrO_3$ and hexagonal $Ba_{0.5}Sr_{0.5}CoO_3$ are indicated.

Figure 6-2 shows that the evolution of the cubic lattice parameter for the series BSCF·Z100*x* is in accordance with Vegard's law up to the composition x = 0.03, suggesting that the solid solubility limit lies in the range 3 - 5 mol% of Zr. The latter is supported by combined TEM and EDX investigations conducted by Ravkina et al. [61], showing that Zr-rich phases crystallize at the grain boundaries of samples BSCF·Z100*x* with $x \geq 0.05$.

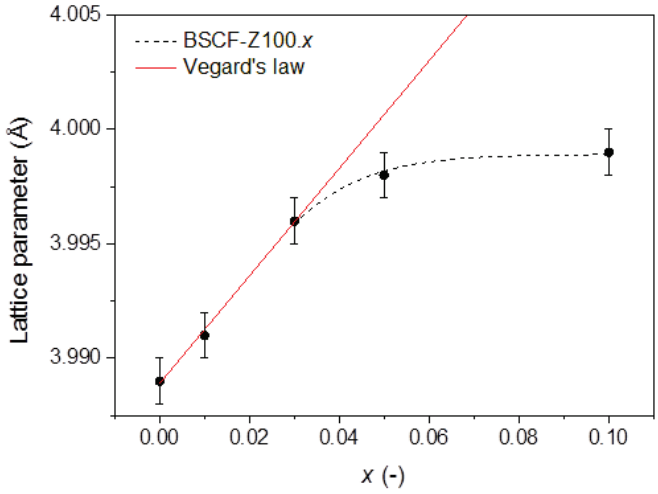

Figure 6-2 Evolution of the lattice parameter with x in BSCF·Z100x. The dashed line indicates Vegard's law for solid solution.

Typical SEM micrographs of BSCF·Z100*x* samples are given in Figure 6-3, verifying that homogenous microstructures were obtained. From these micrographs porosities of less than 5% were extracted for all samples in the series. SEM and EDX analysis of the BSCF·Z10 specimen after thermal etching confirmed segregation of Zr-rich phases at the grain-boundaries.

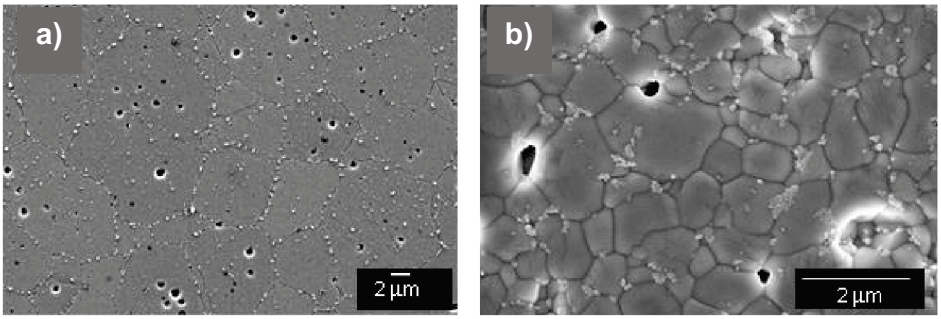

Figure 6-3 Typical SEM micrographs of sintered BSCF-Z100 ×x ceramics: (a) BSCF-Z3 and (b) BSCF-Z10 (thermally etched 950°C for 20min).

Table 6-1 lists grain sizes that were estimated from Light Microscope Images or SEM micrographs (depending on the grain size, the smaller the grain size SEM analysis was required). These Images for all compositions are presented in Appendix A. From

the results it is immediately apparent that substitution of (Co,Fe) by Zr severely suppresses grain growth.

Table 6-1 Average grain size along with standard deviations (s.d.) for BSCF·Z100x after sintering. (Equivalent Circular Diameter ECD). The analysis was performed for reference specimens for BSCF and BSCF·Z1

Material	Grain size (µm)
BSCF	17.0 (6.0)
BSCF [45]	29.0 (11.0)
BSCF·Z1	17.0 (4.0)
BSCF·Z3	8.0 (2.0)
BSCF·Z5	5.0 (2.0)
BSCF·Z10	1.5 (0.5)

At similar sintering conditions (see next section), the grain size for BSCF·Z10 is less by a factor ~13 compared to that observed for pure BSCF. The observations are tentatively explained by a solute drag effect exerted by possible segregation of Zr to the grain boundaries (due to the charge and size mismatch with native (Co, Fe) ions in BSCF). At dopant concentrations in excess of the solid solubility limit, secondary phase pinning or dragging mechanism (Zener pinning) may contribute to the suppressed grain growth [253]. Regarding the reference BSCF materials, the apparent larger grain size results from the different manufacturing process (spray pyrolysis and isostatic pressing for BSCF studied in the current work vs solid state synthesis and extrusion for the reference one from literature. Sintering conditions were also different (1150 °C for 30 h in current work vs 1130 °C for 3 h in the reference [45].

6.1.2 Creep measurements

Arrhenius plots of the creep rates of compositions BSCF·Z3 and BSCF·Z10 upon heating and cooling are presented in Figure 6-4. Similar results were obtained for other compositions of the BSCF·Z100x series (see Appendix A).

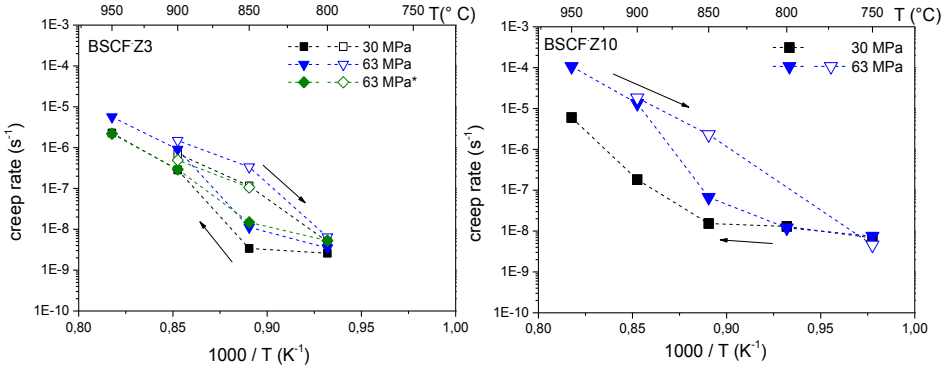

Figure 6-4 Temperature dependence of the steady-state creep rate for (left) BSCF-Z3 and (right) BSCF-Z10 at nominal stresses of 30 and 63 MPa. The arrows indicate heating and cooling directions. The closed points represent heating and open ones the cooling sequence. *after Pećanac et al. [254].

For BSCF·Z3 a good agreement is noted with results obtained previously by Pećanac et al. [254] on sintered extruded tubes (porosity 6 %, grain size 20 ± 8 µm) as illustrated in Figure 6-4 (left), verifying an insignificant influence of the production route. A profound hysteresis in the creep rates was observed upon thermal cycling for all investigated compositions. The origin of the hysteresis in the creep rate for pure BSCF was explained previously by the material's phase instability below ~850 °C [48]. Therefore, it seems that the Zr doping does not affect the hysteresis which is present in pure and doped materials. This effect will be further discussed in chapter 6.1.3.

Activation energies and average stress exponents obtained by fitting experimental data of the creep rate of compositions BSCF·Z100x, at T ≥ 850 °C, according to Equation 4-11 are listed in Table 6-2:

Table 6-2 Activation energy, Q_a (at 63 MPa), and average stress exponent, n, for creep of BSCF·Z100x. Data were obtained from fitting experimental data (linear regression, Q_a and standard error of the steady-state creep rate (T ≥ 850°C).

	n [-]		Qa [kJ/mol]	
	Heating	*cooling*	*heating*	*cooling*
BSCF[45]	1.7 ± 0.2	-	530	340 ± 40
BSCF·Z1	2.0 ± 0.5	1.9 ± 0.1	570 ± 70	320
BSCF·Z3	1.5 ± 0.2	1.2 ± 0.2	730 ± 150	320 ± 10
BSCF·Z5	2.4 ± 0.6	-	660 ± 45	-
BSCF·Z10	4.0 ± 1.5	4.6 ± 0.5	845 ± 190	440 ± 25

Due to the hysteresis in the creep rate, the apparent activation energies for heating and cooling runs are found highly dissimilar. As hexagonal polymorphs are absent in pure BSCF when heated up to ~950 °C [48], and polymorphism is induced only during long-term annealing below ~850 °C, the extracted values of Q_a from cooling curves are considered to reflect the activation energy for creep of the cubic perovskite phase. Average values of Q_a extracted from data of cooling runs for pure BSCF [45], BSCF·Z1 and BSCF·Z3 are in the range 320-340 kJ/mol. Good agreement is noted with the value of 350 kJ/mol extracted from data of sintered extruded tubes of BSCF·Z3 measured under similar conditions [254].

For BSCF·Z10 a slightly higher value of 440 kJ/mol is measured (see Table 6-2). For this composition, an additional test was performed at the temperature range 850°C – 900 °C and after subsequent cooling to 850 °C (Figure 6-5), where no or minimum amount of hexagonal phase is expected even during the heating phase.

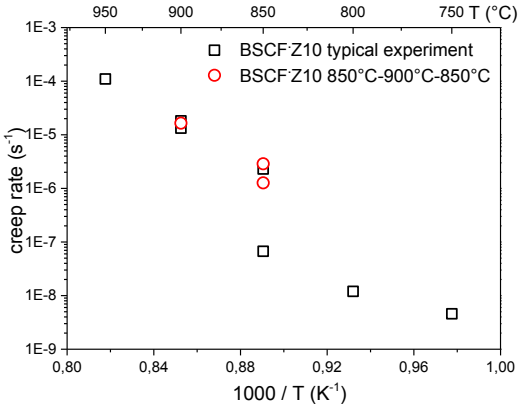

Figure 6-5 Creep rates of BSCF·Z10 obtained for different heating profiles.

Indeed, the yielded activation energy Q_a was lower (560 kJ/mol during heating and 380 kJ/mol during cooling) and the hysteresis loop was narrower as well. But again, in case of cooling the activation energy is slightly higher than for the other compositions. Nevertheless, it is clearly evidenced that even for the highest doping level of 10% the cubic-to-hexagonal transformation is not avoided. The observed high activation energies resemble those measured for cation diffusion in perovskite oxides as determined from diffusion couple and isotope tracer experiments [255,256,257], and exclude oxygen ions as the rate controlling species, noting that

the activation energy for oxygen transport in BSCF ceramics has been reported to be below 50 kJ/mol [42].

As can be seen from Table 6-2, the stress exponent n varies between 1.5 and 2, except for BSCF·Z10, suggesting a diffusion-aided creep mechanism for the compositions with lower Zr contents. Strictly speaking, the value of n is close to unity for diffusion creep, while for, e.g. dislocation creep, it is usually in the range of $3 \leq n \leq 8$ [258,259,260]. For pure BSCF (with grain size 29 ± 11 µm) a value of $n = 1.7 \pm 0.5$ for T > 800 °C was reported by Rutkowski et al. [45] while Yi et al. [261] reported $n = 0.76 \pm 0.23$ for the lower stress regime 5 - 20 MPa. The stress exponent n higher than 1 indicates the coexistence of other creep mechanism additional to diffusion. The grain size exponent $p = 1.7 \pm 0.2$ reported by Rutkowski [45] and $p = 2.45$ reported by Yi et al. [261] correspond to the hypothesis that both grain boundary and bulk diffusion are coexisting as it was also suggested by Schröder et al. [262] via diffusion studies.

For BSCF·Z10, the stress exponent obtained in the current study is ~4, suggesting a change from diffusion to dislocation creep at higher Zr contents. The grain size measured before and after the test agreed within the limits of uncertainty (1.0 ± 0.3 µm and 1.5 ± 0.5 µm, respectively), and no specific grain orientation could be verified by electron backscatter diffraction (EBSD). An alternative explanation would be, that grain boundary pinning by secondary (Ba,Sr)ZrO_3 phases contributes to diffusional creep in BSCF·Z10. For a diffusion creep mechanism, the creep rate depends on grain size. The measured creep rates were therefore normalized to a grain diameter of 1 µm. A value $p = 1.7$ was used for the inverse grain size exponent in the calculations, which was taken from a previous study on the grain size-dependence of the creep rate of pure BSCF [45].

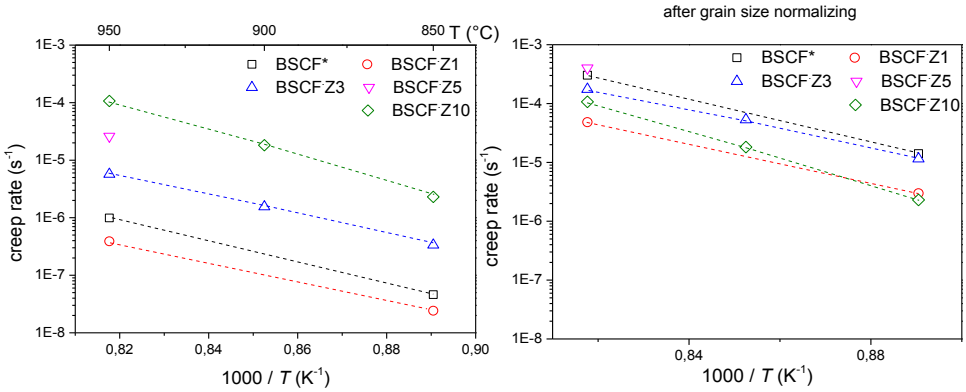

Figure 6-6 Steady-state creep rate of BSCF·Z100x, at T ≥ 850 °C (cooling runs), (left) before and (right) after normalization to grain size d = 1 µm (*data after [45]).

Figure 6-6 shows the creep rates (cooling curves), at T ≥ 850 °C, of compositions BSCF·Z100x before and after normalization, respectively. Figure 6-6 (right) reveals that the normalized creep rates vary for the different compositions. Overall, only by causing supression of grain growth, Zr substitution of (Co,Fe) in BSCF leads to an enhancement of the creep rate relative to that observed for the pure material [263].

6.1.3 Microstructural studies after creep test

Microstructural analyses after the creep tests were performed in order to gain more information about the effect of Zr doping on the cubic-to-hexagonal transformation and also for the creep mechanism.

HT-XRD was performed for BSCF5582 material with high amount of the hexagonal phase $Ba_{0.5}Sr_{0.5}CoO_3$ (~ 40%), after annealing at 850 °C. The following phases were present in the microstructure as verified by the XRD analysis: cubic BSCF ~ 60% (PDF 99-000-0029) ~40% hexagonal $Ba_{0.5}Sr_{0.5}CoO_3$ (PDF 99-000-0030) and a minority monoclinic phase with possible composition $(Ba,Sr)_2(Fe,Co)_2O_5$ (depicted as $Ba_2Fe_2O_5$ ICDD 00-043-0256). The results are presented below:

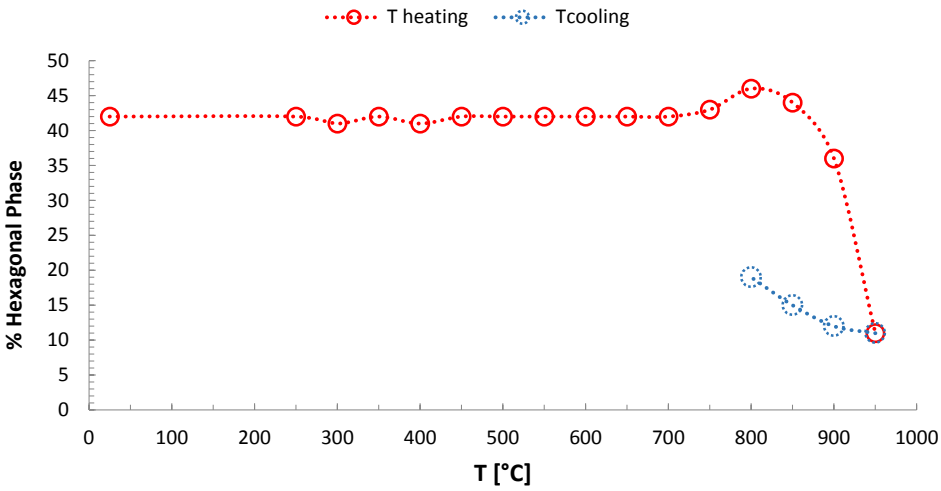

Figure 6-7 Evolution of hexagonal phase $Ba_{0.5}Sr_{0.5}CoO_3$ with temperature for heating and cooling sequence for BSCF5582.

Although several hexagonal polymorphs have been observed by various groups, in the current study $Ba_{0.5}Sr_{0.5}CoO_3$ was the main phase observed and verified for all materials after creep tests (Appendix A). This polymorph is mainly segregated at grain boundaries as it can be observed in the SEM images after the creep test as well as after an additional annealing test that will be described later in this section. From the HT-XRD results it can be seen that the hexagonal phase remains constant up to 700°C when it starts to be increased with gradually increasing rate up to 800°C. Then it starts to be transformed to cubic phase again with gradually increasing rate up to 950°C. The hexagonal-to-cubic transformation rate is very fast above 900°C. Upon cooling the hexagonal phase is formed again proving the reversibility of this transition. The remaining 10% of the hexagonal phase at 950°C is also an effect of thermal cycle, since its amount seems to be dependent on the thermal history and dwell time [44,51,53,254]. At this point it could be noted, that despite of this fact the obtained creep rates were not affected since the same thermal conditions were applied for all tests. The hexagonal-to-cubic transformation follows the same trend as the hysteresis curve for BSCF [45] and BSCF·Z3 materials shown in Figure 6-6. When the hexagonal phase is present, creep rates are lower, while in the temperature range where the cubic phase dominates, creep rates are higher. Regarding the other observed phases described before, the monoclinic phase seems to disappear for temperature higher than 900°C, while from 800°C a new phase

appears that cannot be identified (d_{100}=18° 2θ) because it overlaps with the hexagonal phase. Nevertheless, it doesn't belong to any of the other three phases. The thermal cycle was interrupted at 750°C due to equipment related problems. A measurement at RT after quenching of same sample from 750°C showed only the cubic and hexagonal phases.

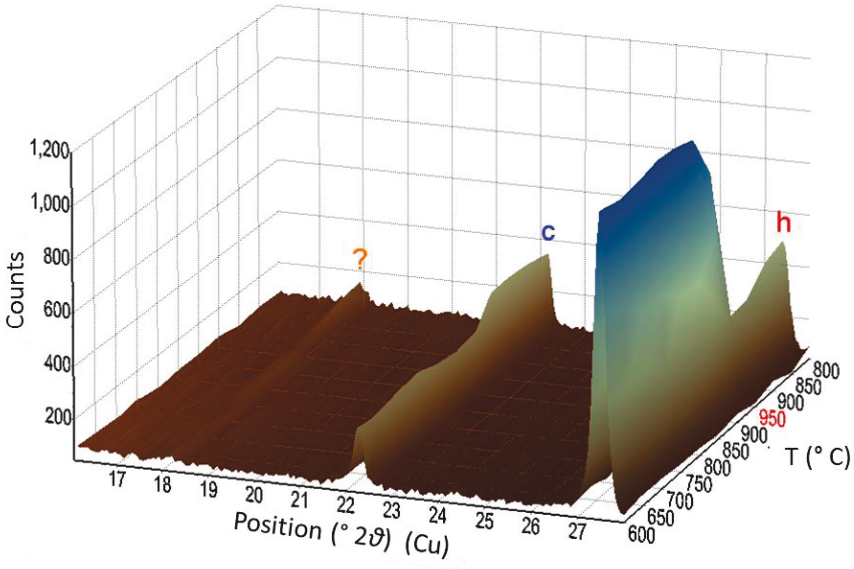

Figure 6-8 HT-XRD data of BSCF5582 where the hexagonal-to-cubic transformation is shown. Another unidentified phase is present above 800 °C (2θ 18°C).

In case of BSCF·Z3, after the creep test with a last step at 750°C, the hexagonal phase $Ba_{0.5}Sr_{0.5}CoO_3$ was present after the test, and mainly located at grain boundaries as verified with XRD and EDX analysis as illustrated in Figure 6-9. Yakovlev et al. [60] observed during electrical conductivity studies, that the growth of hexagonal phase at grain boundaries restricts the overall rate of the surface exchange reaction while it simultaneously reduces grain boundary diffusion. Hence, the hexagonal phase probably blocks grain boundary diffusion paths and eventually leads to a higher creep resistance.

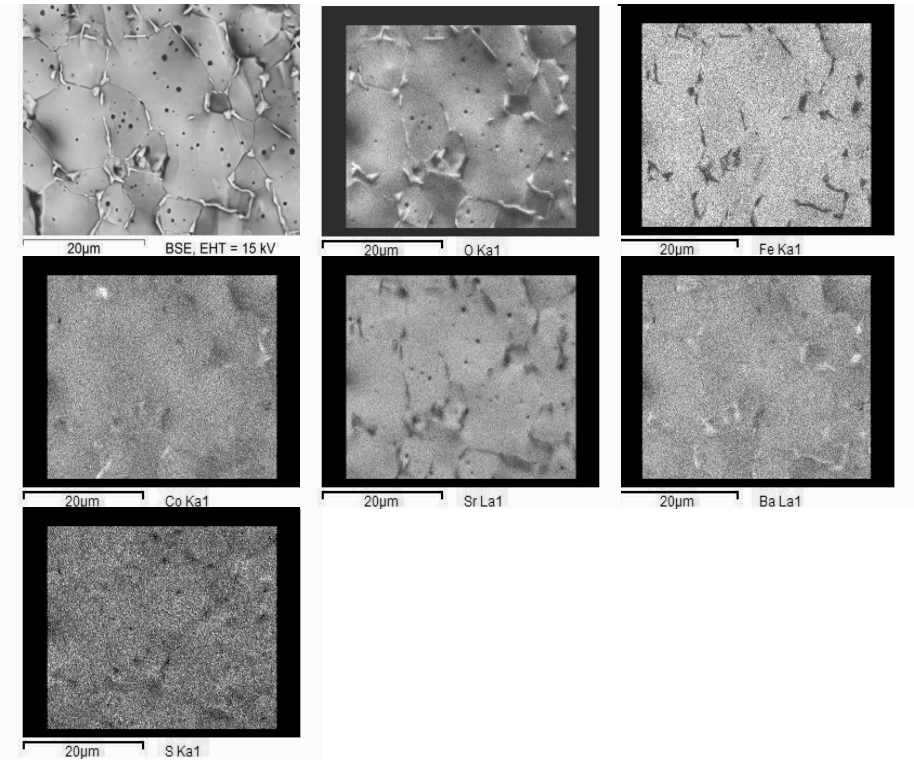

Figure 6-9 BSCF·Z3 microstructure after creep test (final step 750°C- 63 MPa) Hexagonal phase is present and mainly located at grain boundaries.

The XRD analysis for BSCF·Z100x after creep test is presented in Figure 6-11. For BSCF·Z10 after creep test (final step 750 °C) this hexagonal phase was also present as verified by XRD analysis. Nevertheless, the SEM analysis is not so clear since there is segregation of the two phases at the grain boundaries ($Ba/SrZrO_3$) and $Ba_{0.5}Sr_{0.5}CoO_3$. A representative EDX analysis is presented in Appendix A. In case of BSCF·Z1 and BSCF·Z5 other phases were present in the microstructure as well. Nevertheless, in case of BSCF·Z1 the secondary phases were of small amount thus could not be verified by XRD analysis. In case of BSCF·Z5 the monoclinic phase $Ba_2Fe_2O_3$ was present. A table summarizing all the phases detected after creep tests can be found in Appendix A). A possible reason could be that this compound is not stable, since the Zr doping was close to the dissolution limit (see section 6.1.1). The representative SEM Images are also presented in Appendix A.

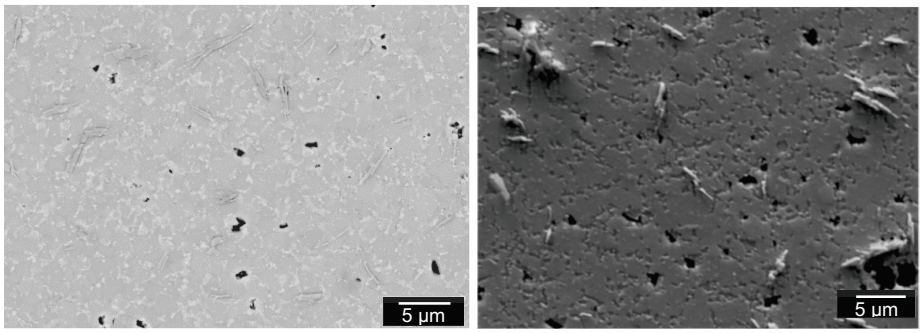

Figure 6-10 BSCF·Z10 microstructure after creep test (final step 850°C 63Mpa). Backscattered (left) EBSD (right).

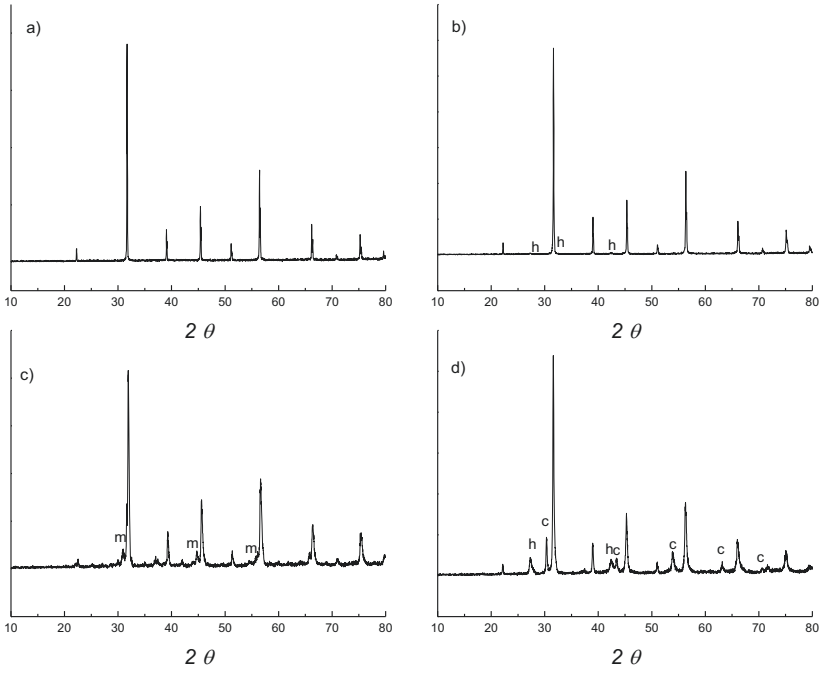

Figure 6-11 XRD after creep test for BSCF·Z100x series. a) BSCF·Z1 (last step 750°C 63 MPa) b) BSCF·Z3 (last step 750°C cooling) hexagonal phase $Ba_{0.5}Sr_{0.5}CoO_3$ (h), c) BSCF·Z5 (last step 950°C 63 MPa) $Ba_2Fe_2O_5$ (m) d) BSCF·Z10 (last step 850°C 63MPa) (Ba/Sr)ZrO_3 (c) and hexagonal. In all cases matrix phase was cubic BSCF5582.

In case of diffusional creep, grain growth is expected. Therefore, a grain size analysis for the same samples of BSCF·Z3 and BSCF·Z10 was performed. The grain size measured before and after creep tests agreed within the limits of uncertainty (1.0 ±

0.3 µm and 1.5 ± 0.5 µm, respectively) for BSCF·Z10, and no specific grain orientation could be verified by electron backscatter diffraction (EBSD). For BSCF·Z3 grain growth was also negligible (8 ± 2 before test and 8 ± 4 after the creep test). Moreover, no change in the aspect ratio was observed. Maybe the total strain (less than 10% after the creep test) was too small to yield significant grain growth. In case of BSCF·Z1 a very inhomogeneous microstructure was revealed with two areas of different porosity and grain size (Figure 6-12). It seems that in one area there was irregular grain growth leading to a very big grain size while in the second area the grain size was 17 ± 5.5 µm. This difference in grain growth could be the reason of the lower creep rates obtained for this composition. The reference sample that was used for the grain size analysis showed homogeneous microstructure but also similar grain size (see Table 6-1).

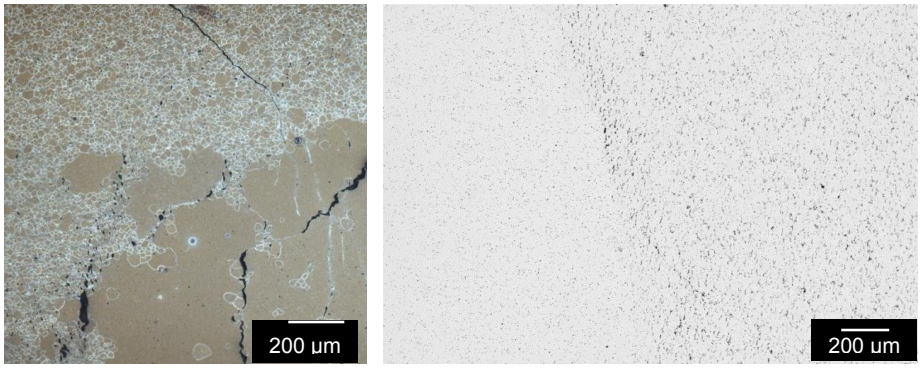

Figure 6-12 Microstructure of BSCF·Z1 after creep test (last step 750°C 63 MPa) polished surface (right) thermally etched at 970°C for 30 min in air (left).

6.2 ST·F100x

6.2.1 Structural analysis

XRD patterns at room temperature for the ST·F30, ST·F50 and ST·F70 compositions (section 5.1.2) before and after creep measurements in air are shown in Figure *6-13* (PDF 01-084-1004), verifying in all cases a cubic perovskite structure, without any evidence of a second phase formation.

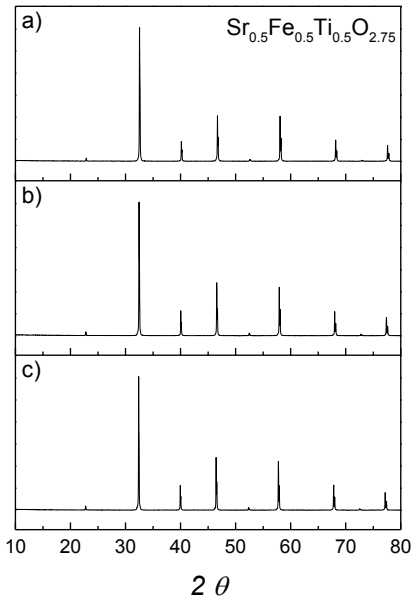

Figure *6-13* XRD patterns for ST·F100x series before creep test a) ST·F30 b) ST·F50 c) ST·F70.

Figure 6-14 shows the dependence of the lattice parameter on the Fe content for the ST·F100x materials. The lattice parameter at room temperature decreases monotonously with increasing Fe content. The results are in good agreement with data reported for materials with the same composition in literature, where it is suggested that the lattice parameters for ST·F100x materials lie between the Vegard's plots [264] of $Sr^{2+}Ti^{4+}_{(1-x)}Fe^{4+}_{x}O_3$ and $Sr^{2+}Ti^{4+}_{(1-x)}Fe^{3+}_{x}O_{3-x/2}$ indicating a mixed valence of $Fe^{3+/4+}$ [66,265]. The ionic radii of the VI-fold coordinated Fe-cations are smaller (0.585 Å for Fe^{4+} / 0.55 Å for Fe^{3+} in low spin state [266]) than the Ti^{4+} radius (0.605 Å), explaining the decrease in lattice parameters.

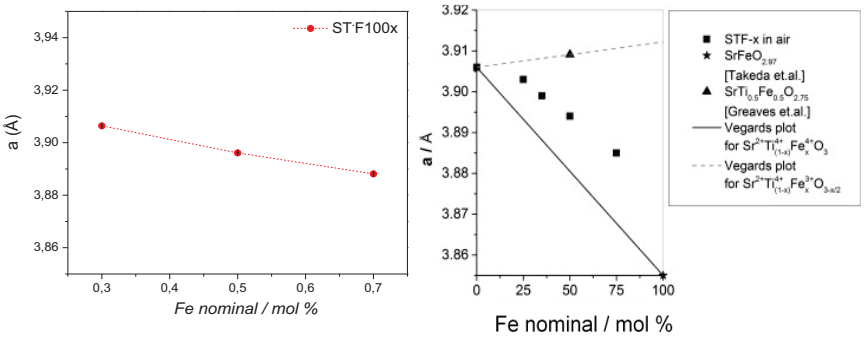

Figure 6-14 Evolution of lattice parameters with Fe content, current study (left) and literature values (right) [66].

Typical SEM micrographs of ST·F100x materials are presented below from longitudinal cross-sections. In all cases the SEM micrographs verify a homogeneous microstructure with no preferential grain orientation. Typical microstructures after creep tests will be presented in section 6.2.4.

Average grain size of ~ 4 µm and porosities of ~ 2 % were determined for ST·F50 and ST·F70 materials, while higher porosity of ~ 8 % and slightly smaller grain size of ~ 2 µm were observed for ST·F30.

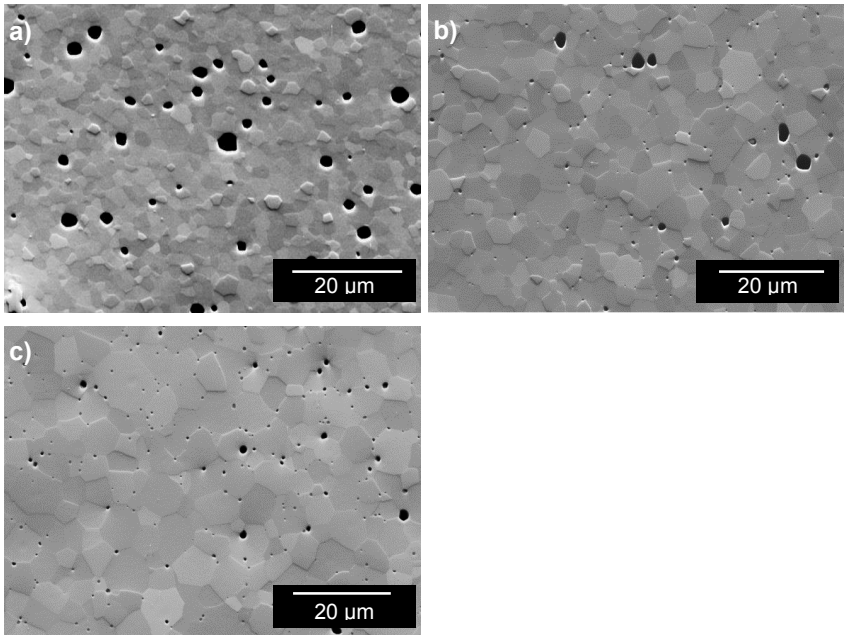

Figure 6-15 Microstructures of ST·F100x materials before creep test a) ST·F30 b) ST·F50 c) ST·F70.

Table 6-3 Results of microstructural analysis for ST·F100x materials.

Material	Porosity (%)	Grain size (ECD µm)
STF 30	8 ± 1	2 ± 1
STF 50	2 ± 1	4 ± 1
STF 70	3 ± 1	4 ± 2

6.2.2 Indentation results

Indentation testing permitted determination of elastic modulus, hardness and fracture toughness of the STF materials. The results are presented in Table 5-4. Higher E_{IT} values are obtained for the ST·F70 compound, while for ST·F30 and ST·F50 values are ~160 GPa, similar as reported for undoped $SrTiO_3$ [150]. The increasing Young's modulus with rising Fe amount might be an indication of effects related to the bond strength. Hence, compounds with stronger bonds exhibit a higher Young's modulus than weak bonded compounds [168]. Therefore, the indentation results, where ST·F70 shows the smallest lattice parameter (Figure 6-14) and the highest Young's modulus (Table 6-4) are in good agreement with theory, although an expected difference between ST·F30 and ST·F50 could not be verified. Micro-hardness shows the same trend: it's increasing with increasing Fe content.

Table 6-4 Indentation results for the ST·F100x series for a load of 1 N.

Material	E_{IT} (GPa)	H_{IT} (GPa)	K_{IC} (MPa·m^{½})
ST·F30	164 ± 5	8.0 ± 0.5	0.93 ± 0.04
ST·F50	157 ± 4	8.6 ± 0.3	0.89 ± 0.02
ST·F70	186 ± 4	9.0 ± 0.3	0.95 ± 0.09

Fracture toughness values were calculated for a Palmqvuist type crack geometry. They are similar for all compounds. The results are in good agreement with literature data, where a fracture toughness K_{IC} = 0.89 $\mathrm{MPa} \cdot \sqrt{\mathrm{m}}$ was reported for $SrTiO_3$ [169]. A typical hardness imprint with indentation cracks is shown in Figure 6-16.

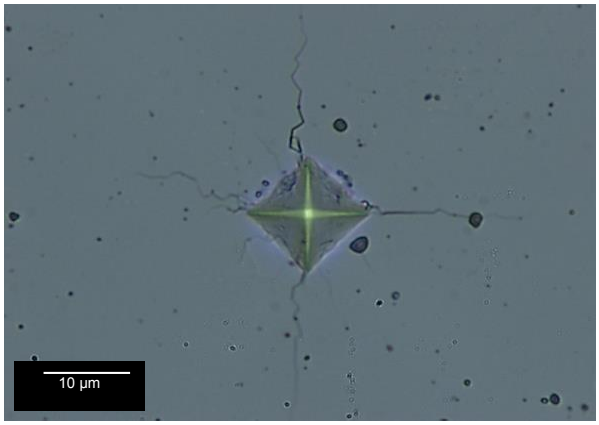

Figure 6-16 Typical indentation imprint at 1 N for ST·F50.

6.2.3 Creep measurements

All creep rates obtained in the current study are presented in Appendix B, while the Arrhenius plots for all compositions at stresses of 30 & 63 MPa are presented in Figure 6-17.

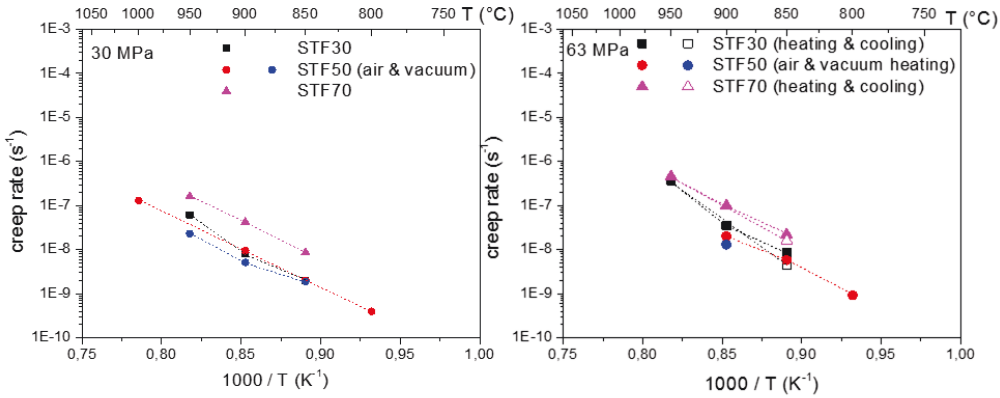

Figure 6-17 Creep rates for ST·F100x materials.

Creep rates were in the range of ~ $3 \cdot 10^{-7}$- ~ $3 \cdot 10^{-10}$ s^{-1} for all ST·F100x materials in temperature regime 800 – 1000 °C and the stress range 10 - 70 MPa, respectively. Thermal heating and cooling cycles were applied similar as in the case of BSCF·Z100x materials to investigate possible hysteresis effects. The results obtained for ST·F30 and ST·F70 show that the heating and cooling creep rates agree (difference between the two values obtained at 850 °C in heating and cooling rate was 20 %) hence no hysteresis effect was observed. In case of ST·F50 the tested samples showed cracks before the cooling steps were applied, therefore the obtained values were omitted. Nevertheless, similar behavior for ST·F50 might be expected.

The results for ST·F70 indicate higher creep rates than for the other compositions. It was demonstrated that permeation rates and thermal/chemical expansion increase with increasing Fe content for ST·F100x materials [66]. Creep might then be related to the defect chemistry of the material like it was suggested for $La_{0.58}Sr_{0.4}Co_{0.2}Fe_{0.8}O_{3-\delta}$ [267]. Steinvik et al. [268] found that for $Sr(Ti,Fe)O_{3-\delta}$ materials formation of superstructures take place when more than 50 % B sides are occupied with Fe cations, whereas the phases with smaller iron content are disordered. The degree of ordering in the oxygen sublattice determines the concentration and mobility of oxygen vacancies. Higher concentration of oxygen vacancies could be the reason for higher creep rates, since more diffusional paths are created. However, it seems for the other materials investigated in this study that creep rates are dependent on grain size in case of diffusional creep. Therefore, more

systematic studies regarding the grain size as well as the grain size exponent should be performed to exclude this possibility. Tests in different atmosphere should also be done for this composition to verify if the reason of the higher creep rates is related to the defect chemistry.

The average activation energies are between 360 and 430 kJ/mol. The activation energies as well as the stress exponents are presented in Table 6-5. It seems that in ST·F50 and ST·F70 diffusion aided creep since dominates due to n = 1. But for ST·F30 a higher stress exponent n indicates contribution of a different creep mechanism. The stress exponent also increases above 900 °C, pointing towards contribution of dislocations to the deformation mechanism, thus a transition of diffusion to power law creep at higher stresses and temperature is evident. In case of ST·F30 the activation energy also appears to show a tendency towards an increase with applied stress (390 ± 50 kJ/mol at 30 MPa and 430 ± 70 kJ/mol at 63 MPa from 850 - 950 °C).

Table 6-5 Activation energy Q_a and average stress exponent n for creep of STF100·x. Data were obtained from fitting Equation 4-11 to experimental data.

x	Q_a(kJ/mol)			n		
	T (°C)	Load (MPa)		950 °C	900 °C	850 °C
		30	63			
0.3	850-950	390 ± 50	430 ± 70	2.4 ± 0.2	2.0 ± 0.1	2.0 ± 0.1
0.5		340	320 ± 30	-	1.2 ± 0.1	1.5
0.7		330 ± 10	350 ± 10	1.1 ± 0.2	1.5 ± 0.1	1.2 ± 0.2
0.5 (vacuum)	850-950	280 ± 40	-	-	1.6 ± 0.3	-

The activation energies for the undoped STF materials that were discussed in chapter 3.2.2 are compared to the activation energies of ST·F100x materials obtained from the current work at 30 MPa (Table 6-6). The activation energy for diffusion of oxygen in $SrFeO_3$ (SF) and Sr in $SrTiO_3$ (ST) are 54 and 296 kJ/mol, respectively [269,270] establishing the A or B cations as the slowest moving species controlling the creep rate. In fact, Ti^{4+} was suggested to be the rate limiting cation in case of $SrTiO_3$.

It seems that the activation energy decreases when ST is doped with Fe, however, the effect appears to be independent of the amount of dopant, since the obtained activation energies for the three different doping levels agreed with in the limits of standard deviation. In case of SF, the activation energy is very close to the one reported for Sr diffusion [270].

Table 6-6 Activation energies for ST·F100x materials.

Material	Q_a (kJ /mol)	Reference
ST	628 ± 24	208
ST·F30	390 ± 50	Current work (271)
ST·F50	330 ± 25	
ST·F70	330 ± 10	
SF	260 ± 30	204

Overall, it seems that substituting iron for Ti^{4+} changes the rate controlling species while the doping amount does not seem to influence the activation energy.

A set of experiments under different pO_2 was performed in order to determine the oxygen partial pressure exponent, *m*, where as an example for the ST·F100x series, ST·F50 was chosen. The results were already presented in Figure 6-17. Creep rates in air and vacuum were almost identical at 850 °C. For higher temperatures a small increase is observed for creep rates in air compared to the vacuum data. Nevertheless, activation energies for air and vacuum were similar (330 ± 25 kJ/mol and 280 ± 40 kJ/mol). The stress exponent at 900 °C for vacuum was determined to be 1.6 ± 0.3. The equivalent value for air at this temperature is 1.2 ± 0.1, hence also here data agree within the limits of uncertainty. Overall, differences between the behavior in air and under vacuum are too small to determine an oxygen partial pressure exponent (see also literature chapter 4.5.2). However, as rough estimation for the experimentally boundary conditions, the oxygen partial pressure exponent was determined to be close to zero. Nevertheless, it appears to increase slightly with temperature from 850 to 950 °C as shown in Figure 6-18.

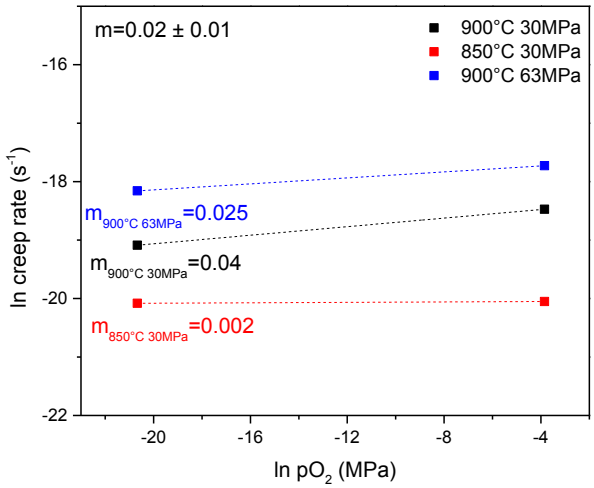

Figure 6-18 Creep rate pO_2 dependence and oxygen partial pressure exponent of creep rate.

6.2.4 Microstructural analysis after creep test

XRD patterns after creep tests revealed only the cubic perovskite phase verifying the microstructural stability of the materials (Figure 6-19):

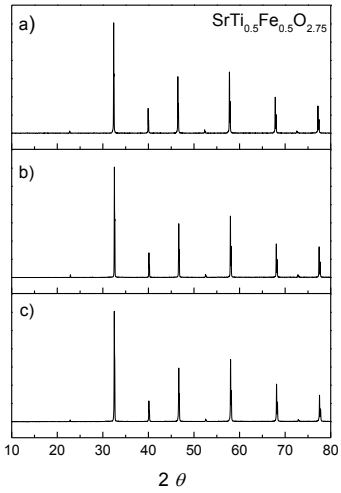

Figure 6-19 XRD patterns at RT after creep test for a) ST·F30 b) ST·F50 c) ST·F70.

Furthermore, high temperature XRD (HT-XRD) was performed in the same atmospheres as in creep tests (air and vacuum) for direct comparison. HT-XRD for ST·F50 also verified the structural stability for the material from room temperature up

to 950 °C. The cubic perovskite phase was maintained for both atmospheres in the entire temperature range. The results of the HT-XRD are presented below:

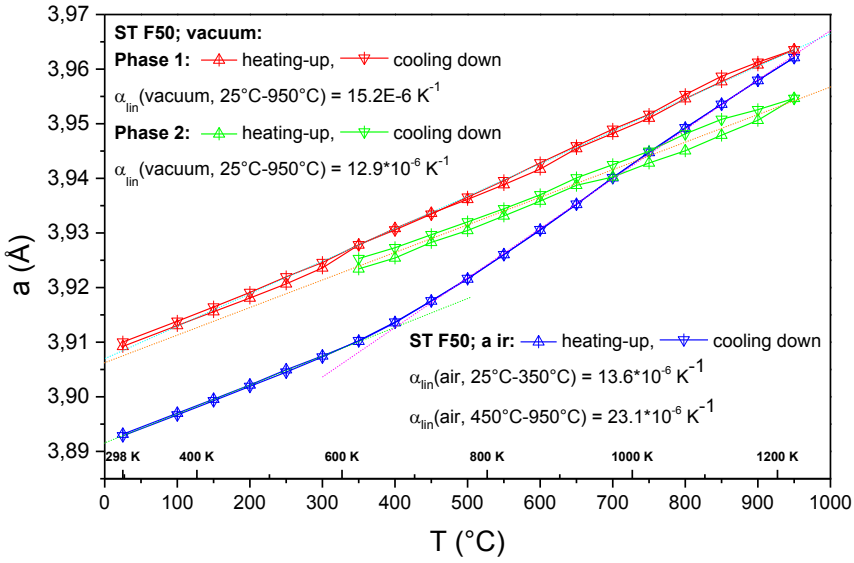

Figure 6-20 HT-XRD of ST·F50 in air and vacuum.

The overall expansion behavior of ST·F50 in air and vacuum is illustrated in Figure 6-20, where the lattice parameter is plotted as a function of temperature. In air an increase in the slope was observed above 450 °C, which was ascribed to reversible combined thermal and chemical expansion. The total expansion coefficient representing both thermal and chemical expansion was calculated from the slope according to $\alpha = \frac{\Delta l}{l_0 \cdot \Delta T}$. For the temperature range 25 – 350 °C the thermal expansion coefficient is $13.6 \cdot 10^{-6}$ K^{-1} and increases to $23.1 \cdot 10^{-6}$ K^{-1} from 450 – 950 °C, which can be attributed to the contribution of chemical expansion. Similar values for the overall expansion coefficient for these materials are reported in literature [66,272]. In case of vacuum measurement, the XRD revealed two different cubic perovskite phases, with slightly different expansion coefficients ($15.2 \cdot 10^{-6}$ and $13 \cdot 10^{-6}$ K^{-1}) for the temperature range 25 - 950°C. The presence of the second cubic phase can most probably be attributed to an experimental error due to a possible temperature gradient along the sample holder, which was heated from below. Therefore, this phenomenon was not further analyzed. For the main phase, the kink of the slope was noticeably less pronounced than in air, indicating that the chemical expansion in

vacuum is lower than in air for temperatures above 450 °C. For MIEC perovskite materials, the total strain at elevated temperature results from thermal and chemical expansion. The parallel initial slope for both atmospheres observed from 25 to ca. 450 °C is merely attributed to thermal expansion.

The chemical expansion results from the release of oxygen from the perovskite phase. The fact that in vacuum the lattice parameters are higher at room temperature indicates that more Fe is initially reduced at 3+ valence state. From the graph it can be seen that the reduction starts above 400 °C. The oxygen release is associated with the reduction of VI-fold coordinated Fe cations from Fe^{4+} to Fe^{3+} initiating an increase in the ionic radius during heating (0.585Å Fe^{4+} to 0.645Å Fe^{3+}) and / or decreasing oxygen partial pressure [273.274,275] Simultaneously with the Fe reduction oxygen vacancies are released from the lattice to maintain the charge neutrality. The chemical expansion increases due to the formation of oxygen vacancies (vacancy concentration). Each new vacancy leads to an increase in the lattice parameter of the oxide crystal, thus the lattice expands as the oxide becomes more non-stoichiometric [276]. The identical lattice parameters observed at 950 °C for air and vacuum indicate similar final oxidation state under both conditions, however, the energy needed in air to reach such amount of oxygen vacancies is higher since Fe is fully reduced at 950 °C.

To investigate the effect of creep on microstructure, longitudinal cross-sections, parallel to the loading axis, were cut from the central part of the samples. SEM images for all compositions after creep tests are presented in Figure 6-21. The microstructural studies after the creep tests verified again that the material remained single phase. Changes in the microstructure regarding grain growth or aspect ratio were negligible for all materials.

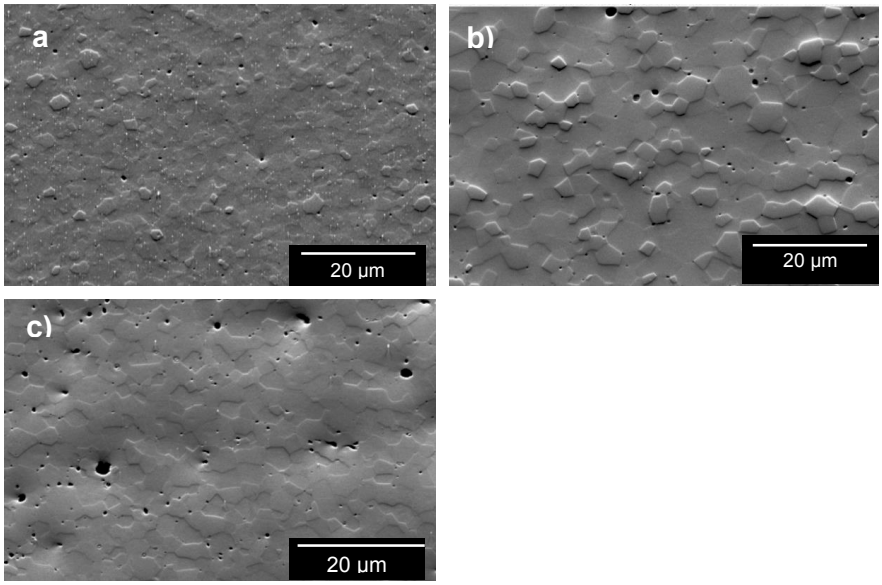

Figure 6-21 Microstructures of ST·F100x materials after creep test a) ST·F30 (last step 850°C 63 MPa cooling) b) ST·F50 (last step 950 °C 30 MPa) c) ST·F70 (last step 850°C 63 MPa cooling).

EBSD grain orientation mappings for ST·F50 compound (Figure 6-22) show the distribution of grains in specific orientations. Inverse Pole Figure (IPF) maps in which the colors correspond to the crystal orientations are shown in the projection for the Euler angle based color scale for the three dimensions *X*, *Y*, *Z*. No specific grain orientation was detected for any of the materials parallel to the compressive load direction which indicates homogeneous deformation. Same results regarding grain orientation were obtained for the other two compounds.

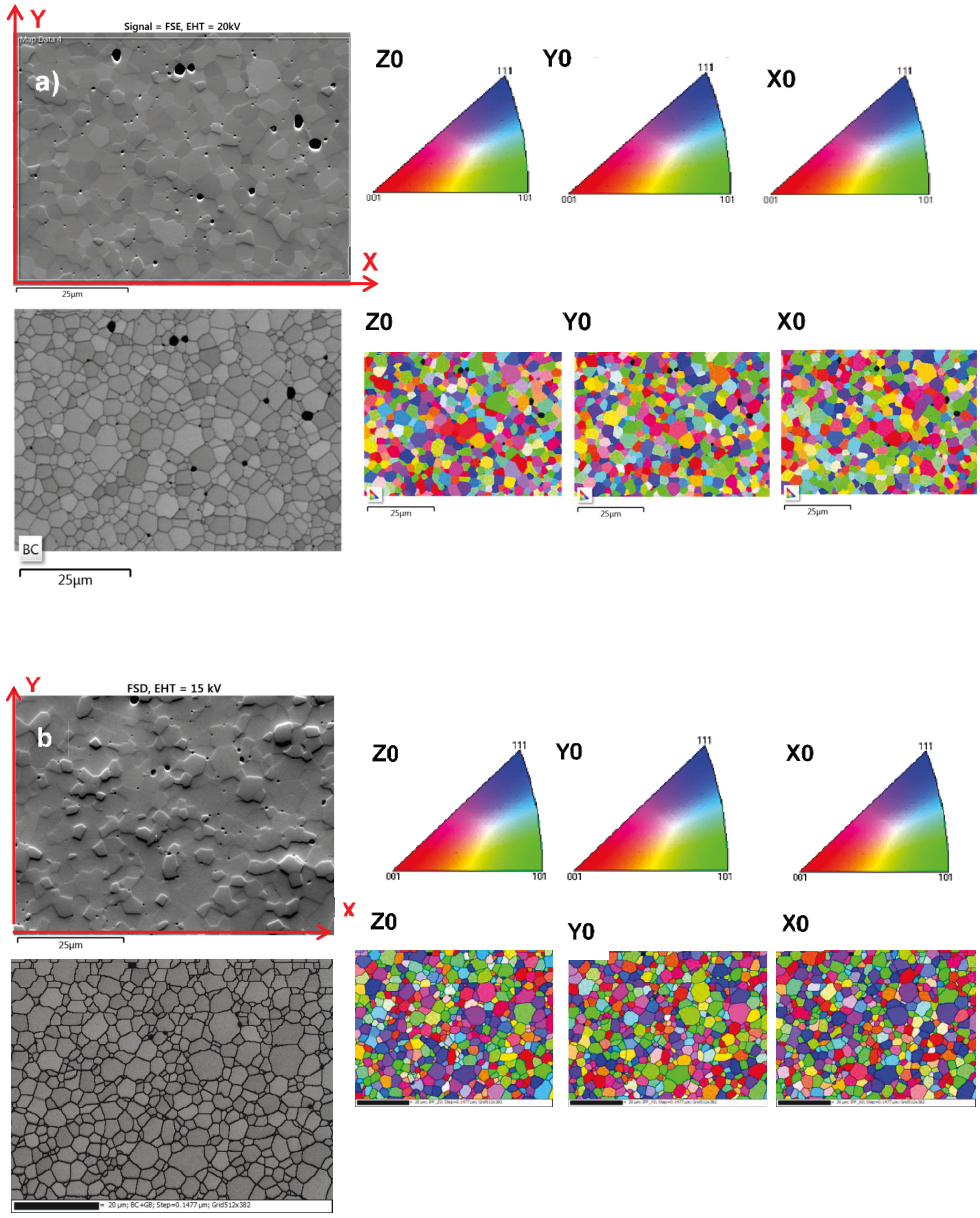

Figure 6-22 Band contrast images and EBSD orientation maps for the ST·F50 compound a) before and b) after creep test (last step 850°C 63 MPa cooling). Analysis was performed in the loading direction for the crystallography planes of cubic single phase $SrTi_{0.5}Fe_{0.5}O_{3-\delta}$ in 3D (X, Y, Z axis).

6.3 LWO54

Dense and porous LWO54 have been characterized, the respective results are presented in separate sections. Whereas the dense material was investigated to gain basic understanding of the material´s behavior, the porous LWO was characterized to assess the relationship between mechanical properties and manufacturing process and to identify optimization possibilities.

6.4 Dense LWO

6.4.1 Structural analysis

Materials based on IEK-1 powder and CPT powder were characterized. Room temperature XRD patterns of LWO54 after sintering are presented below. All materials were verified to be single phase, cubic $La_{5.4}WO_{12-\delta}$ (ICSD 189792). The different relative intensities in Figure 6-23 are due to the different specimen state (powder or dense sample).

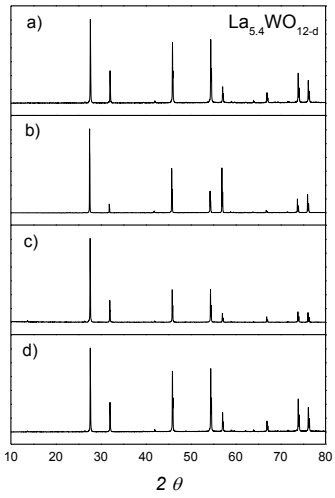

Figure 6-23 XRD patterns at RT of LWO54 after sintering a) IEK-S1 b) IEK-S2 c) CPT-D1 d) CPT-D2.

Typical microstructures of LWO54 specimens' longitudinal cross-sections after sintering are presented below:

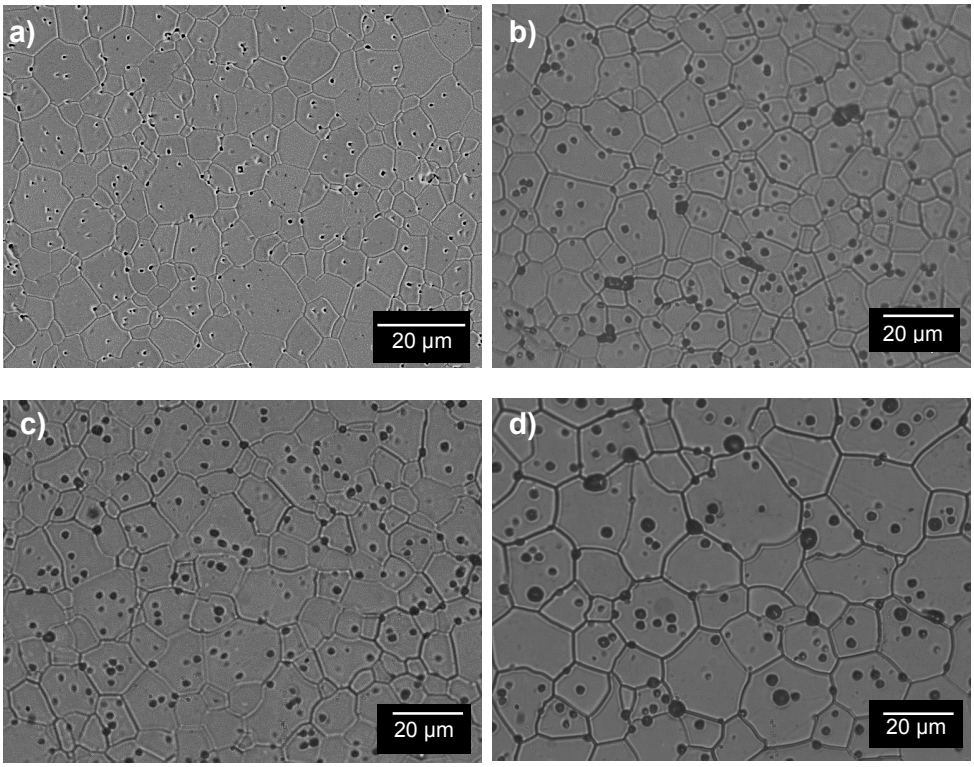

Figure 6-24 Microstructures of dense LWO54 specimens a) IEK-S1 b) IEK-S2 c) CPT-D1 d) CPT-D2

Porosities and grain sizes were determined are presented in Table 6-7.

Table 6-7 Microstructural data of tested materials

	Sintering conditions T_{sint} (°C) / dwell time (h)	**Porosity (%)**	**Grain size (µm)**
IEK-S1	1500 / 3	12 ± 3	6 ± 3
IEK-S2	1500 / 12	3 ± 1	11 ± 4
CPT-D1	1500 / 15	9 ± 4	9 ± 3
CPT-D2	1500 / 15	6 ± 1	17 ± 6

In cases of IEK-S1 and IEK-S2 homogeneous microstructures were found. The shorter dwell time for IEK-S1 led to a higher porosity and a slightly smaller grain size in comparison with the other materials. Although CPT-D1 and CPT-D2 (both produced from commercial powder) have identical sintering conditions, the obtained grain sizes appear to be slightly different due to the different powder characteristics (particle size and specific area BET, see Appendix C) that obviously led to different

sintering behavior. Different sintering behavior regarding shrinkage could also be the reason for the higher porosity and inhomogeneous pore size of CPT-D1. For these samples, besides areas with different porosity, also some big irregular pores were observed as will be discussed later in the fractographic analysis (section 6.4.1). Overall, the aim of different dwell times was to obtain different grain size in order to investigate the effect of grain size on elastic modulus, creep and strength. But due to different powder characteristics, the microstructures were not optimal for systematic studies in all cases.

6.4.2 Elastic modulus, hardness and fracture toughness

6.4.2.1 Indentation results

Indentation testing permitted a determination of elastic modulus, hardness and fracture toughness. The indentation results for a load of 1 N are presented in Table 6-8.

Table 6-8 Indentation results for LWO54 materials at RT (load of 1 N).

Batch name	E_{IT} (GPa)	H_{IT} (GPa)	K_{IC} (MPa·m^{½})
IEK-S2	130 ± 2	8.2 ± 0.3	1.11 ± 0.1
CPT-D1	120 ± 3	7.1 ± 0.4	1.18 ± 0.1
CPT-D2	94 ± 2	7.3 ± 1.5	0.93 ± 0.1

The IEK-S2 material exhibits the highest Young's Modulus and micro-hardness. The lower values obtained for CPT-D1 and CPT-D2 are probably due to larger porosity [277]. The small standard deviation indicates a rather homogeneous microstructure compared to the indentation size (volume). Similar fracture toughness values were obtained, except for CPT-D2 that exhibits slightly lower values.

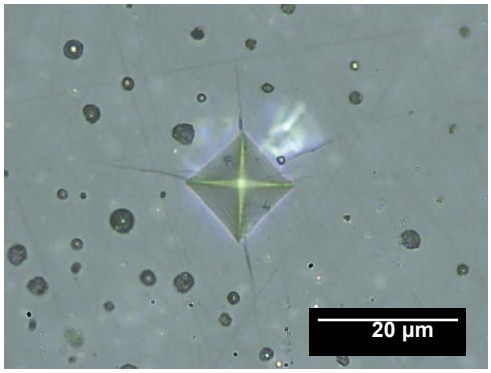

Figure 6-25 Example of typical indentation imprint for LWO54 at 1 N load (CPT-D2).

Roa et al. [174] investigated the micro-mechanical properties of LWO materials with different compositions and microstructures (porosity > 95 %, grain size 1 - 30 µm, some secondary phase segregation) and concluded that Young's modulus and micro-hardness are not affected by the microstructure. The reported values (E_{IT} = 130 ± 15 GPa and H_{IT}= 8-9 GPa) are in good agreement with the materials tested in the current study except for CPT-D2 that revealed lower values. They report a higher fracture toughness of ~ 2 $\mathrm{MPa} \cdot \sqrt{\mathrm{m}}$, which might be related to differences in micro-structure and/or test parameters (loading rate, Berkovich indenter geometry). Nevertheless, the values are comparable to other candidate materials for hydrogen transport membrane and proton-conductors for fuel cell applications (see Table 4-6).

6.4.2.2 Impulse excitation technique

Only IEK-S2 and CPT-D2 specimens were tested in air to derive representative data for the temperature dependency of the elastic modulus. The IEK-S1 samples were not fulfilling the geometry requirements for this test.

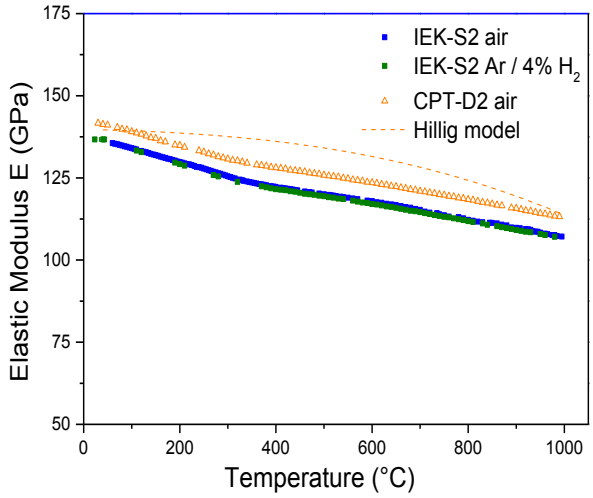

Figure 6-26 Elastic modulus of LWO54 in air (IEK-S2 and CPT-D2) and in Ar / 4% H_2 (IEK-S2) as a function of temperature measured by the impulse excitation technique. The dashed lines represent the model from Hillig [158].

The elastic modulus was ~ 140 GPa at room temperature independent of grain size. Overall, the values at room temperature are in good agreement with the results obtained from indentation and also with literature [156]. However, for CPT-D2 the impulse excitation technique yielded a slightly higher value than the indentation tests. The differences will be discussed in separate chapter.

Generally, the elastic modulus of polycrystalline ceramics, without grain boundary softening, is expected to decrease by ~ 1 % / 100 Kelvin [278]. For LWO54 a decrease by ~ 20 % up to 1000 °C is observed for both materials independent of atmosphere and grain size. A change in the slope is indicated at ~ 400 °C and at higher T the elastic modulus decreases less pronounced with increasing temperature up to 1000 °C.

The temperature dependence of elastic modulus can also be described by the Hillig model, using E_0 = 140 GPa with a melting temperature of T_m = 1960 °C (from the phase diagram La_2O_3-WO_3 [115]). The model predicts that the elastic modulus decreases by ~ 20 % up to 1000 °C, similar to the experimental results. The kink at ~ 400 °C might be attributed to chemical or thermal expansion related effects at this temperature. Escolástico et al. [280] performed TGA measurements after permeation

tests and observed a weight loss at 400 °C temperature suggesting oxygen release from the matrix.

6.4.2.3 Ring-on-ring bending test

LWO54 materials were tested in ring-on-ring bending in order to determine the effect of microstructure on elastic modulus at room temperature. The tested batches were IEK-S2, CPT-D1 and CPT-D2. Samples from IEK-1 powder were not available due to limited amount of powder. Elevated temperature tests were only carried out for samples of the commercial powder CPT-D1 (Figure 6-27). Batch CPT-D2 was also tested at elevated temperatures but samples broke during heating before the measurement started. The reason will be discussed in fractography analysis (6.4.1)

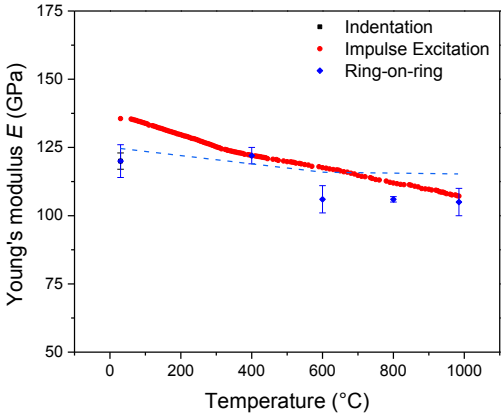

Figure 6-27 Evolution of Young's modulus with temperature for LWO54 (CPT-D1) tested with impulse excitation and ring-on-ring method.

Table 6-9 Comparison of elastic moduli of LWO54 materials determined with different methods

Test Method	Batch name			Testing conditions
	IEK1-S2	CPT-D1	CPT-D2	
Ring-on-ring (prepared surface)	120 ± 6	127± 6	130 ± 20	RT
Ring-on-ring (unprepared surface)	100 ± 20	-	-	RT
Indentation	130 ± 2	120 ± 3	94 ± 2	RT
Impulse Excitation	136	-	142	RT

The results show an average elastic modulus of ~ 120 GPa obtained at room temperature for all tested materials (Table 6-9). Similar as obtained by the other methods, slight differences observed via indentation testing are not visible in the global bending test results. The effect of temperature on the elastic modulus was investigated for the CPT-D1 batch. The decrease with increasing temperature agrees with the impulse excitation results, although at 400 °C a slight increase is observed, whereas in impulse excitation a kink was observed at ~ 400 °C suggesting that the onset of chemical or thermal expansion differences might affect both test results in a different way.

6.4.2.4 Comparison of elastic modulus testing methods

From the results discussed in the previous paragraphs, it can be seen that impulse excitation yields slightly higher Young's moduli for the tested materials. The ring-on-ring test is quite sensitive to the surface condition and hence sample preparation, i.e. wavy surfaces lead up to 20 % different results for the same batch. When flat surfaces are ensured, the elastic modulus values are ~ 10 % lower than obtained via impulse excitation. Regarding indentation tests, specimens with very good preparation (flat and parallel surfaces, minimum roughness) lead to values that agree with impulse excitation. Nevertheless, lower values for CPT-D2 indicate differences in micro- and macro-mechanical properties for this material.

6.4.3 Strength

Fracture stress measurements were performed in ring-on-ring geometry at room temperature for batches IEK-S2, CPT-D1 and CPT-D2. The selection of specific batches was described earlier (see chapter 5.1.3). Mean values of strength are in good accordance with characteristic strength estimated from Weibull analysis (Table 6-10).

Additionally, a set of experiments was performed at room temperature with different loading rates to assess possible effects of subcritical crack growth. Furthermore, CPT-D1 batch was tested up to 1000 °C in order to determine the effect of temperature on strength. Weibull analysis was performed in the cases where specimen numbers were reasonable for statistical analysis as described in chapter 0. Note, that according to DIN the specimen number was too low for a Weibull analysis, hence it should only serve as an indication of the materials behavior.

A typical Weibull plot is presented in Figure 5-28 for batch CPT-D1. The equivalent graphs for the other batches are presented in Appendix C. The results for all batches are summarized in (Table 6-10).

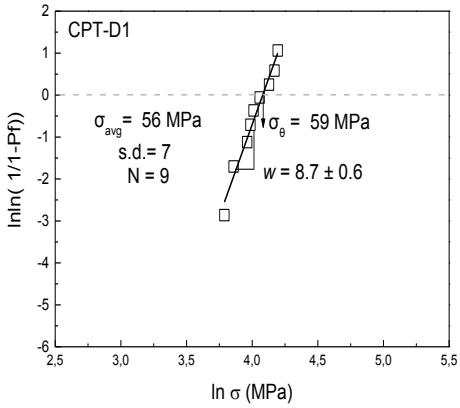

Figure 6-28 Weibull plot for LWO54 (batch CPT-D1) at room temperature.

Table 6-10 Strength results for LWO54 materials at room temperature.

	Batch name		
	IEK1-S2	CPT-D1	CPT-D2
Number of specimens, *N*	13	9	9
Characteristic fracture strength σ_0 (MPa)	124 ± 6	59 ± 3	50 ± 3
Mean fracture strength (MPa)	115 ± 20	56 ± 7	47 ± 7
Lower (0.95%) $t_{0.95}$ / upper (0.05%) $t_{0.05}$ Confidence bounds on σ_0	112 / 137	53.6 / 65.2	45.1 / 54.7
Biased Weibull Modulus w * standard error linear regression	6.2 ± 0.4*	8.7 ± 0.6*	8.0 ± 0.7*
Unbiased Weibull Modulus w_{ub}	5.5 ± 1.5	7.2 ± 2.4	6.7 ± 2.2
Lower (0.95%) $q_{0.95}$ / upper (0.05%) $q_{0.05}$ Confidence bounds on w	3.4 / 7.2	3.8 / 9.9	3.5 / 9.2
Elastic Modulus (GPa)	120 ± 6	127 ± 6	130 ± 20
Fracture strain ε (%)	0.1	0.04	0.04

The LWO54 material prepared by solid state synthesis route (IEK1-S2) has almost a factor ~ 2 higher strength than the batches prepared from commercial powder (CPT-D1 and CPT-D2). This can be related to the more homogeneous microstructure of the IEK1-S2 material. In case of CPT-D2 large agglomerates and irregular pores were found (see fractographic analysis chapter 5.4.1). Also, a secondary Ba rich phase was detected by EDX analysis. Although the CPT-D2 batch also exhibited lower strength values, the microstructure was rather homogeneous with similar porosity as obtained for the IEK-S2 batch (see chapter 6.4.1). Therefore, the values appear also to reflect the effect of grain size on strength. Larger grain sizes are known to lead to lower strengths [168]. The differences in fracture stress are also reflected in fracture strain, where the values are higher for the IEK-S2 batch.

Measurements with different load rates were performed for CPT-D1 in order to investigate if the material is prone to subcritical crack growth (SCG). This experimental set did not reveal a variation in the strength values in the limits of

standard deviation (see Figure 6-29), implying that the material is not significantly sensitive to subcritical grain growth at RT in air.

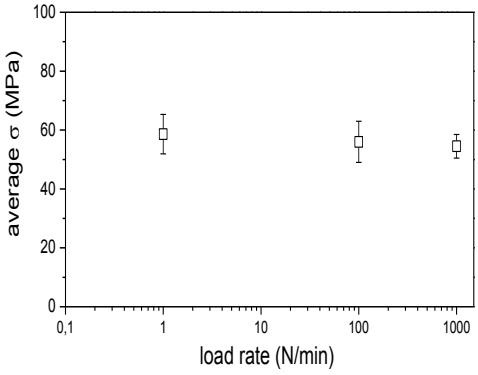

Figure 6-29 Average strength obtained for different load rates. (CPT-D1 batch).

Another set of experiments was performed for the CPT-D1 batch to characterize the elevated temperature strength. The results are illustrated in Figure 6-30. Due to the limited number of tested specimens, Weibull statistics was not applied and only mean values are presented. Testing of CPT-D2 samples was not possible since specimens broke during heating as described earlier.

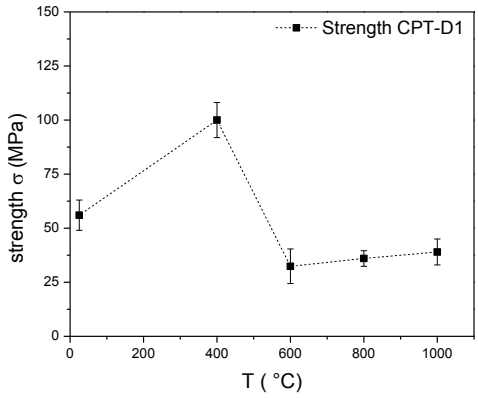

Figure 6-30 Dependence of strength and E on temperature.

The strength of most ceramics decreases monotonously with temperature. In the case of LWO54 an unusual increase of strength is observed at 400 °C from 56 ± 7 to 100 ± 8 MPa (note, at this temperature also the elastic modulus increased). At higher

temperatures (600 – 1000 °C), the strength decreases again. The overall decrease from room temperature to 1000 °C was ~ 45 %.

A set of experiments was performed at 400 °C with different heat treatment in order to determine if this unusual behavior is related to chemical strain effects. A sample was heated up to 1000 °C, cooled down to 400 °C, where it was tested and another sample was heated up to 400 °C, and the load was applied after 12 hours dwell time.

Whereas the sample tested after cooling from 1000 °C revealed almost the same strength (see Table 6-11), the dwelled sample showed a 20 % lower strength. In case of chemical- thermal expansion, dwelling at this temperature could modify the stress distribution due to diffusional processes. No significant effect on elastic modulus was observed. Still, to strengthen this argument more tests are required since this value could be statistical result. In this study more tests could be done due to lack of specimens of the specific batch.

Table 6-11 Experimental setup CPT-2 batch at 400°C

Heating profile	Mean strength σ_B (MPa)	E (GPa)
Standard, heating to 400°C	108 ± 10	122 ± 3
Heating to 1000°C / cool to 400°C	107	129
Heating to 400°C / dwell 12 h	86	120

6.4.1 Fractography

After ring-on-ring tests, the broken discs were used for fractography analysis according to the ASTM C 1322-05b in order to locate and characterize fracture origins. Localization of fracture origin was started by analyzing fracture patterns of the three batches.

The IEK-S1 batch shows high energy fracture patterns, thus the possible failure initiating defects were small and not easy to be located. Moreover, a very homogeneous and fine microstructure was observed for both, fractured and polished surfaces.

The batches prepared from the commercial powder CPT-D2 broke with a lower energy fracture pattern, hence, it was possible to identify failure origins. In case of CPT-D1 fractography analysis revealed agglomerate like defect as typical failure origin (Figure 6-31), related to local clusters of shell like voids formed in numerous

locations in the bulk. Such irregularities were also observed on polished cross-sections. The size of the defects was found to be about 50 - 170 µm. Moreover, EDX analysis (Appendix C) in the polished surface revealed a secondary Ba rich phase. Another observation from fractography analysis is that crack propagation seems to be mostly trans-granular. This is in agreement with indentation results where straight indentation lines indicate trans-granular crack propagation.

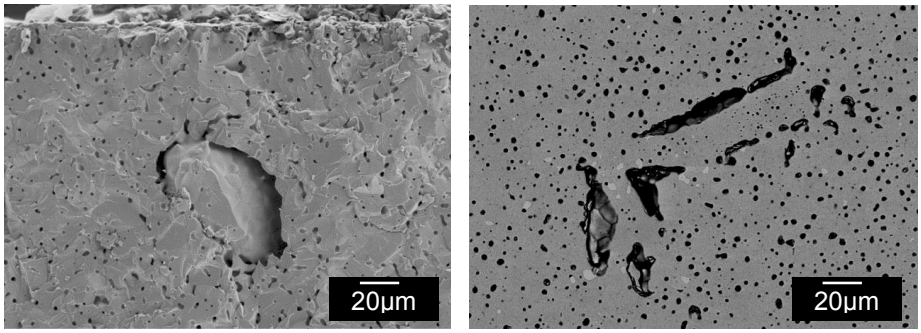

Figure 6-31 Microstructure of LWO54 (batch CPT-D1) showing agglomerates as failure origin in a fracture surface σ_B =44MPa (left) irregular pores and agglomerate in a polished cross section (right).

The CPT-D2 batch indicated lower room temperature strength values than both IEK-S2 and CPT-D1 batches. For this material, zones with higher porosity were identified as failure origin. The size of these porous zones was around 80 µm. They were found in a larger number of places in the matrix close to the surface and inside the bulk. Thus, they were considered as volume defects.

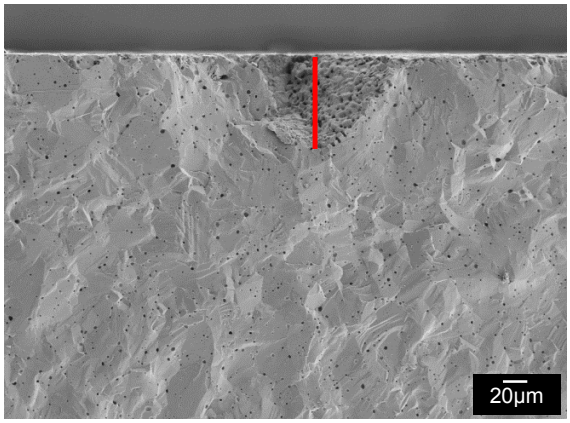

Figure 6-32 Fracture surface of LWO54 (batch CPT-D2 σ_B=22 MPa) after ring-on-ring test at room temperature showing a pore zone as failure origin.

As failure origin for CPT-D2 specimens fractured at 1000 °C a crack around a porous zone similar to the one shown in Figure 6-32 was determined. But also segregation of impurities in the form of very fine grains between the matrix grains was detected. EDX verified Zr, Al, Cr and Fe contaminations. A rough estimation yielded a flaw size about 600 µm. Such a failure origin is illustrated in Figure 6-33. A detailed EDX analysis is presented in Appendix C.

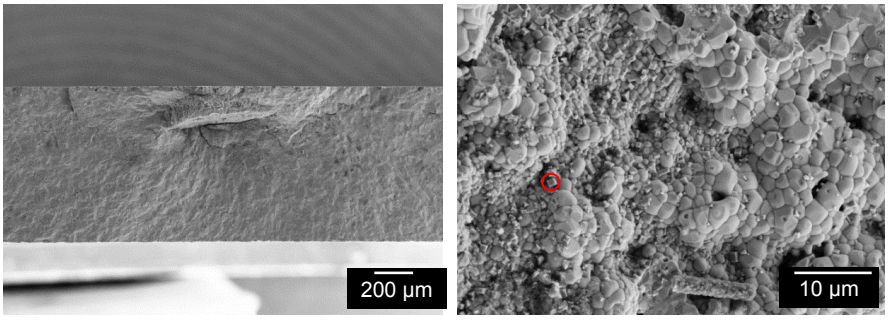

Figure 6-33 Fracture surface of LWO54 (CPT-D2 batch) broke before tested at 1000 °C. Higher magnification (right) show secondary phase as fine grains located (red circle) on the grains of the matrix.

Overall, it seems that the IEK-S2 batch has a higher strength due to its finer microstructure. Irregularities such as big pores, agglomerates and impurities have detrimental impact on strength, especially at higher temperatures. In all cases the fracture mode was transgranular and the defects were located in the bulk of the material thus allowing the use of effective volume in the Weibull size scaling.

From the fracture stress and the representative size of the defects identified as failure initiator (critical defect size), the fracture toughness can be calculated using the Griffith equation (Equation 4 - 10), yielding K_{IC} ~ 0.5 $\mathrm{MPa}\cdot\sqrt{\mathrm{m}}$ for CPT-D1 (σ_B=31.5 MPa, c=145 µm) batch and ~ 0.2 $\mathrm{MPa}\cdot\sqrt{\mathrm{m}}$ for CPT-D2 (σ_B=22 MPa, c=80 µm). These values are much lower than the ones determined via indentation, probably due to complexity and three dimensional nature of the defect type. Thus, the fracture toughness yielded by these calculations is a rough estimation.

6.4.2 Creep tests

The creep rates obtained for LWO54 are presented in Appendix C, while the Arrhenius plots for all compositions for applied stresses of 40 and 63 MPa in air are presented in Figure 6-34.

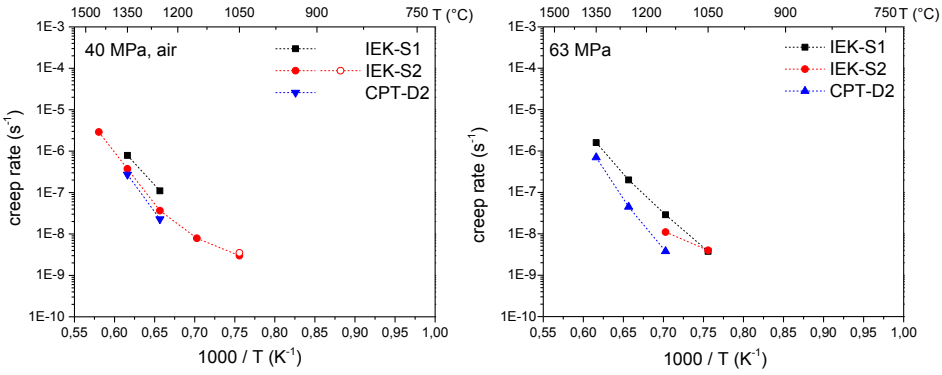

Figure 6-34 Arrhenius plots for LWO54 materials for applied stresses of 40 and 63 MPa in air.

Sample batches IEK-S1, IEK-S2 and CPT-D2 were tested with respect to creep deformation. The selection criterion was based on the grain sizes of the samples; therefore, CPT-D1 which had the same grain size as IEK-S2 was excluded from the test series.

The IEK-S2 material, which had an intermediate grain size (~ 10 µm) was tested over the temperature range 700 – 1450 °C (0.43 ≤ T/ T_m≤ 0.77) at nominal stresses of 20 – 63 MPa in air. Indications of creep deformation were observed above 900 °C for 63 MPa. However, at this temperature the deformation rate was close to the limit of measurement uncertainty (~1.5 µm / 24 hours), therefore, only creep rates at T ≥

1150 °C were used for creep characterization. Creep deformation seems to be insignificant at the operation relevant temperatures of 600 – 800 °C for dense LWO54 materials. Furthermore, creep rates obtained at 1050 °C for IEK-S2 during heating and cooling thermal cycle are almost identical (difference between the values 14 %) thus excluding a hysteresis effect (see BSCFZ related chapters). The obtained creep rates were similar for IEK-S2 and CPT-D2 material, while IEK-S1 revealed higher creep rates as can be seen in Figure 6-34.

The creep parameters were determined by multi-linear fitting of Equation 4 – 11, similar as for the other tested materials. The results are presented in Tables 6-12 to 6-14, while the plots are given in Appendix C:

Table 6-12 Activation energies of LWO54 materials

Stress	IEK1-S1		IEK1-S2		CPT-D2
	1050 – 1250°C	1250 – 1350°C	1050 – 1250°C	1250 - 1350°C	1250 - 1350°C
20	-	-	190 ± 40	380	-
40	-	405	210 ± 30	480	480
63	330 ± 10	420	-	--	565

Table 6-13 Stress exponents for LWO54 materials

Temperature (°C)	Material		
	IEK1-S1	IEK1-S2	CPT-3
1050	-	0.60 ± 0.01	-
1150	-	0.80 ± 0.05	-
1250	1.20 ± 0.10	1.00	1.70
1350	1.20 ± 0.15	1.70	1.50
1450	-	1.20	-

Table 6-14 Inverse grain size exponent p for LWO54 materials

Temperature (°C)	Stress	
	40 MPa	63 MPa
1150	-	1.9 ± 0.3
1250	1.5 ± 0.2	1.4
1350	1.0 ± 0.1	0.8

An average activation energy of 450 ± 35 kJ/mol for 1250 – 1350 °C at 40 MPa along with an average stress exponent of 1.2 ± 0.4 for 1050 – 1450 °C for all materials indicate diffusional aided creep.

The activation energies are in good agreement with those obtained from interdiffusion studies, i.e. Vøllestad et al. [279] reported activation energies of 410 ±

30 kJ/mol and 450 ± 30 kJ/mol for La and W, respectively, for 1150 – 1350 °C in air and 5% H_2 / Ar. The diffusion coefficient for La diffusion through grain boundaries was determined to be 170 ± 50 kJ/mol. It was concluded that this reflects migration via a common mechanism for both species, facilitated by vacancies in the lanthanum sub-lattice.

The stress exponents are close to 1 and increase slightly with temperature for the IEK-S2 material. The jump to $n \sim 1.7$ at 1350 °C was biased by primary creep effects for the respective material.

The inverse grain size exponent p in Table 6-14 is independent of stress but decreases with increasing temperature.

The various possible creep mechanisms give rise to different combinations of exponents n and p so that the transitions from one mechanism to another could be defined. At 1150 °C $p \sim 2$, (Note that p only changes for temperature, Table 6-14) only IEK-S2 material with the grain size ~ 11 µm was tested at 1150 °C, and yielded $n \sim 1$. This suggests diffusional creep where the diffusion path could be either along the grain boundaries (Coble) or through the grains (Nabarro- Herring) according to Table 4-7. Vøllestand et al. [279] determined the activation energy of La through grain boundaries in air to be 170 ± 50 kJ/mol, similar to the activation energy derived for IEK-S2 material at this temperature. With increasing temperature p slightly decreases, up to 1250 °C, to ~ 1.5. For IEK-S1 and IEK-S2 materials with grain size up to ~ 10 µm the stress exponent is close to 1, while for CPT-D2 with larger grains (~ 17 µm) the stress exponent is slightly increased ($n \sim 1.7$). For CPT-D2 it seems that additional mechanisms contribute to the diffusional mechanism. For the IEK-S1 and IEK-S2 materials with smaller grain size, again a combination $1 < p < 2$ and $n \sim 1$ is found and diffusional mechanism is suggested. Moreover, a kink in activation energy is observed at this temperature (Table 6-12) for IEK-S2, indicating a transition from Coble to Nabarro-Herring creep. For IEK-S1 or CPT-D2 materials this kink was not observed. Coble creep also dominates for smaller grain sizes (Figure 4-3*),* hence this behavior could be valid only for the intermediate grain size. To verify this hypothesis, studies with a broader grain size range are required. In case of CPT-D2, measurable creep rates could not be obtained for the lower temperature range. Moreover, the activation energies reported by Vøllestand et al. [279] are similar to the

ones obtained for T ≥ 1250 °C. Another possibility could be the transition of anions (O^{2-}) to cations (La or W) as the creep rate controlling species.

For further increase to 1350 °C, *p* decreases from 1.5 at 1250 °C to 0.8 (hence *p* is taken to be close to 1). For IEK-S2 material the stress exponent *n* is close to 1. Since no theoretical identification of creep mechanism is possible for the combination of $n \sim 1$ and $p \sim 1$, it is assumed that other mechanisms contribute to creep deformation and there might be a transition to GBS. Overall, similar to the outcome of the diffusional studies by Vøllestad et al. [279] migration seems to occur via a common mechanism for both species via both, lattice and grain boundaries.

Creep tests were also performed under vacuum (10^{-2} bar) in order to determine the oxygen partial pressure dependence under Ar / 4% H_2 as well as wet Ar / 4% H_2 in order to gain information regarding the creep behavior under operation related atmosphere. Sputtering was used to coat the sample with a thin Pt layer (1 µm) to improve the catalytic activity and to avoid surface limitation of kinetics. An additional annealing step of 12 h at 900 °C was applied to reach the H^+ concentrations in the lattice similar to permeation experiments [280]. Moreover, it was found that continuous gas flow was required to maintain constant amount of Ar / 4% H_2 in the chamber.

A testing temperature of 1000 °C was selected. The applied stress and measurement time were chosen to obtain reliable secondary creep rates. Results along with testing conditions are summarized in Table 6-15 and presented in Figure 6-35:

Table 6-15 Creep rates and testing conditions for LWO54 specimens at 1000 °C.

Material	Stress (MPa)	Atmosphere	Conditions	Creep rates (s^{-1})
IEK1-S2	40	Air	Typical	$1.0 * 10^{-9}$
IEK1-S2	40	Air	Pt coating	$2.0 * 10^{-9}$
IEK1-S2	40	Ar/ H_2 4%		$3.0 * 10^{-9}$
IEK1-S2	40	Ar/ H_2 4%, H_2O 2.5%	Pt coating, continuous gas flowing	$1.5 * 10^{-9}$
IEK1-S2	40	Ar/ H_2 4%	Pt coating	$9.6 * 10^{-10}$
CPT-D2	100	Air	Typical	$7.8 * 10^{-10}$
CPT-D2	100	Vacuum (10^{-2} mbar)	Typical	$7.2 * 10^{-10}$

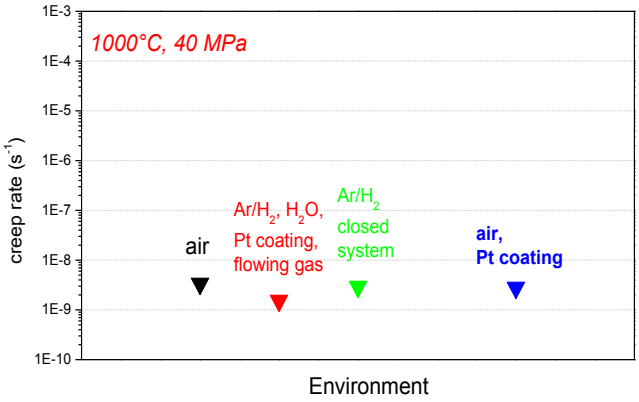

Figure 6-35 Effect of atmosphere on creep rates of LWO54 (IEK-S2) at 1000°C, 40 MPa.

From the results it can be seen that the creep rates are quite similar for both materials. Similar creep rates were obtained for CPT-D2 material under air and vacuum. Regarding IEK-S2 material, it seems that Pt coating does not affect the creep rates in air. In case of Ar / 4% H_2 with continuous gas flow and 2.5 % H_2O in the chamber, slightly lower creep rates are observed. It seems that there is no significant effect of H_2 on the creep rates under the present testing conditions (uncertainties of obtained values ~ 50 %). However, looking at the plot in Figure 6-35, there might be an effect of the gas supply, which could not be kept constant during the test due to the setup limitations.

For CPT-D2 material a rough estimate yielded n ~ 0.5 at 1000 °C in vacuum and a partial oxygen stress exponent of m ~ 0 can be determined, indicating the same behavior as in air.

6.4.3 Microstructures after creep testing

To investigate the effect of creep on the microstructure, longitudinal cross-sections, parallel to the loading axis, were cut from the central part of the samples. The single phase microstructure was verified via XRD and SEM analysis of polished surfaces. Grain size analysis was performed for thermally etched surfaces in order to gain more information about the creep mechanism. Micrographs and grain size analysis are presented in Figure 6-36 and Table 6-16, respectively.

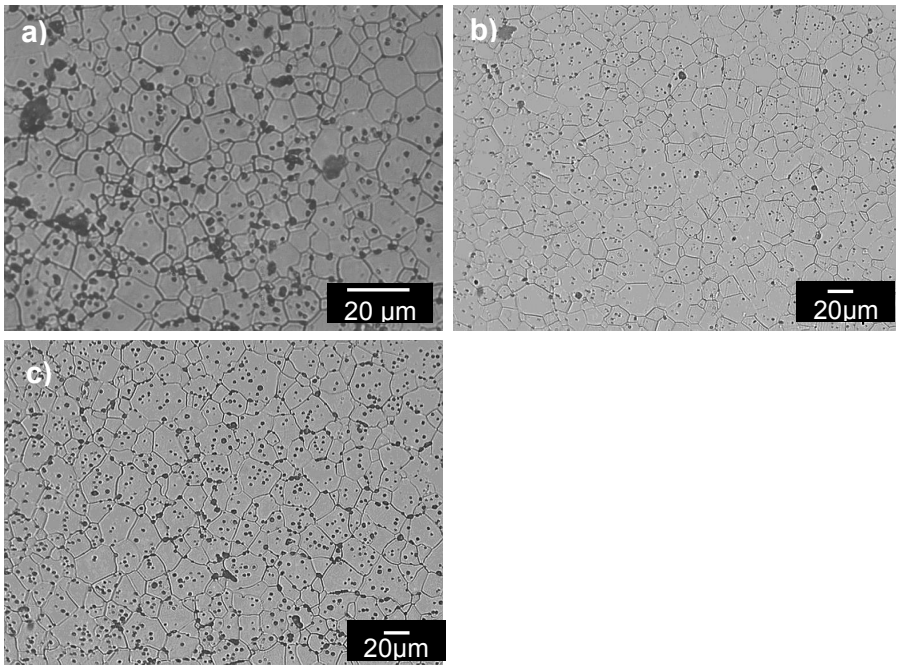

Figure 6-36 Thermally etched microstructures of LWO54 materials after creep test a) IEK-S1 (last step 1350°C, 63 MPa) b) IEK-S2 (last step 1450 °C ,40 MPa) c) CPT-D2 (last step 1350°C, 63 MPa).

Table 6-16 Grain size analysis for LWO54 materials

Material	Before Creep	After creep
IEK1-S1	6 ± 3	8 ± 4
IEK1-S2	11 ± 4	13 ± 5
CPT-D2	17 ± 6	20 ± 8

Overall, it appears to be a tendency for a small grain size increase is for all materials. However, it is within the limits of standard deviation.

Although phase change or contaminations were not observed after the tests, some changes were visible on the surface of the samples. In case of IEK-S2 material tested at 1450 °C in air, EDX indicated a W depletion (Figure 6-37). It seems that at this temperature, the stoichiometry changes and volatile WO_x is produced. A SEM image of this sample is presented below (detailed EDX analysis in Appendix C). Since the effect is limited to the surface of the specimens, an effect onto the creep test results can be ruled out. However, sintering for shorter time at 1500 °C or even lower temperatures might be appropriate.

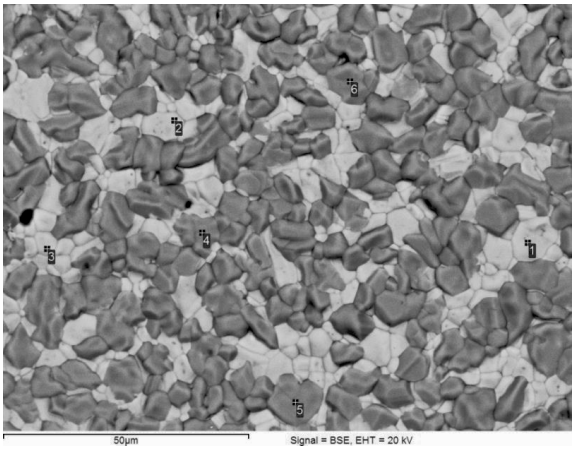

Figure 6-37 Backscattered SEM Image of LWO54 (IEK-S2) after creep test at 1450°C (surface of sample). Two phases are present.

6.5 Porous LWO

6.5.1 Structural analysis

The surfaces of the delivered samples were of different color. XRD analysis verified that the red color was attributed to a much higher (5 times) amount of the secondary phase $La_6W_2O_{15}$ (PDF 00-037-0124). On the red side of the samples the secondary phase was ~ 20% wt.

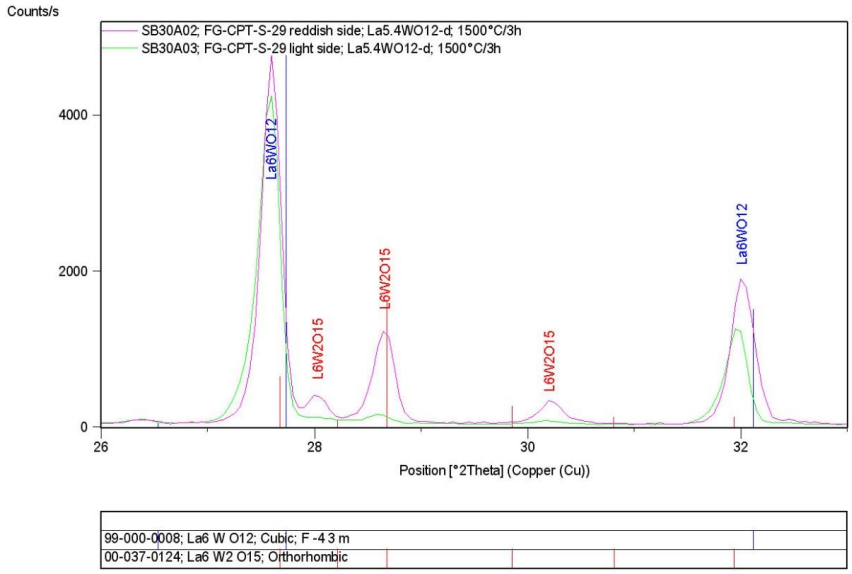

Figure 6-38 XRD comparison of $La_6W_2O_{15}$ on both sides of CPT-P-29 specimen.

The results are summarized in Table 6 – 17. As can be seen, the higher amount of pore former leads to higher porosities. A problem in case of higher porosity is the shape of the delivered samples: samples with highest porosity exhibit significant bending, which, although the method is less sensitive to shape variations that the ring-on-ring test, might have biased the ball-on-3 ball test results.

Table 6-17 Microstructure features of porous LWO54 materials

Material	Pore former (%)	Porosity (%)
CPT-P-29	20	30 ± 1
CPT-P-25	25	32 ± 1
CPT-P-26	35	39 ± 1

The microstructures of the porous LWO54 (cross-sections) materials are presented in Figure 6 – 39.

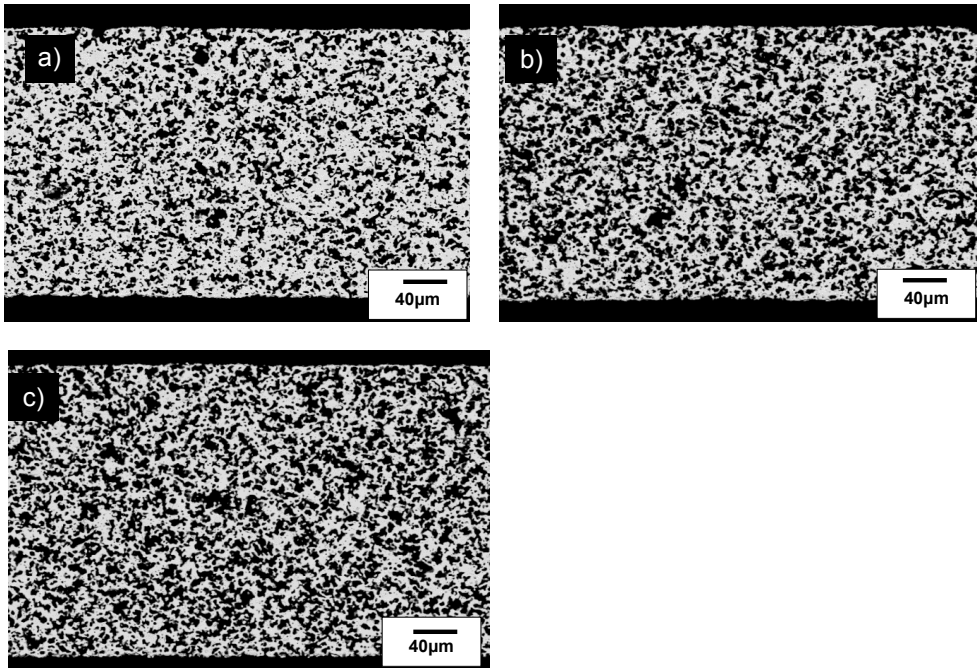

Figure 6-39 Cross- sections of porous LWO54 materials a) CPT-P-29 b) CPT-P-25 c) CPT-P-26.

6.5.2 Strength (Ball-on-3-balls)

The summarized strength results of the LWO54 porous materials are presented in Table 6-18:

Table 6-18 Strength results for porous LWO54 materials at room temperature

	Batch name		
	CPT-P-29	CPT-P-25	CPT-P-26
Number of specimens, N	28	27	14
Characteristic fracture strength σ_0 (MPa)	87.3 ± 1.0	82.3 ± 2	66.7 ± 2
Mean fracture strength (MPa)	84.2	78.1	63.4
Lower (0.95%) $t_{0.95}$ / upper (0.05%) $t_{0.05}$ Confidence bounds on σ_0	85.3 / 89.4	78.6 / 86.2	63.3 / 70.3
Biased Weibull Modulus *w* * standard error linear regression	15.7 ± 1.3	8.4 ± 0.5	11.1 ± 1.5
Unbiased Weibull Modulus w_{ub}	15 ± 3	8 ± 1.5	10 ± 2.7
Lower (0.95%) $q_{0.95}$ / upper (0.05%) $q_{0.05}$ Confidence bounds on w	11.1 / 18.4	5.9 / 9.8	6.3 / 13.1

It can be seen from Figure 6-40 and Figure 6-41 that increasing porosity leads to an almost linear reduction of strength. Moreover, the batch with lowest porosity shows higher Weibull modulus *w,* indicating more homogeneous distributions of the flaw population in the material.

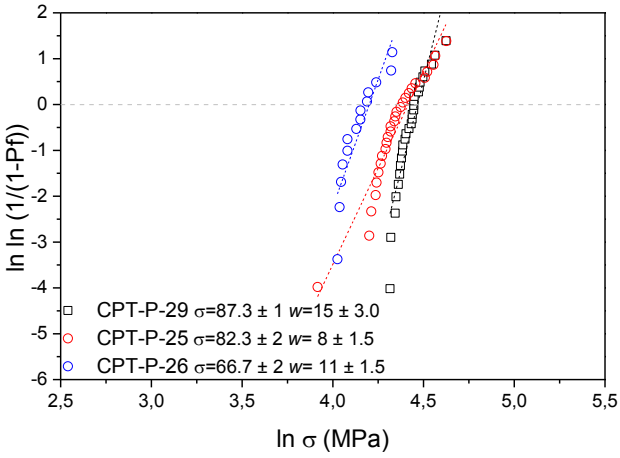

Figure 6-40 Weibull plots for LWO54 porous materials.

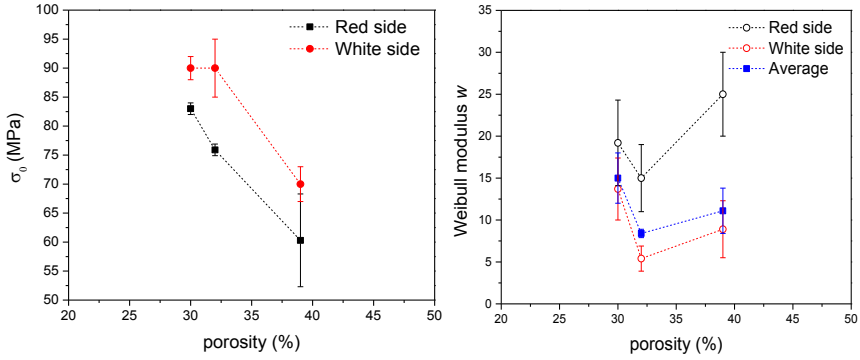

Figure 6-41 Effect of porosity on strength and Weibull modulus of tape casted LWO54. The noted sides indicate which side (red; rich in secondary phase, white; cubic $La_{5.4}WO_{12-\delta}$) were in tension.

In order to clarify whether the secondary phase influences the strength, LWO54 samples were tested both with the higher amount of the secondary phase (red side) in tension or compression. As it can be seen in Figure 6-41, the secondary phase leads to lower strength values and this effect is most pronounced for higher porosity.

6.6 NWO55

The microstructure of NWO55 after sintering is presented in Figure 6-42. It was verified by XRD and SEM analysis that the material had a cubic, single phase, crystal structure (ICSD 189792), and a homogeneous microstructure with ~ 8 % porosity and fine grains (average grain size of 1 ± 0.5 μm). The elastic modulus determined by indentation was E_{IT} = 125 ± 5 GPa.

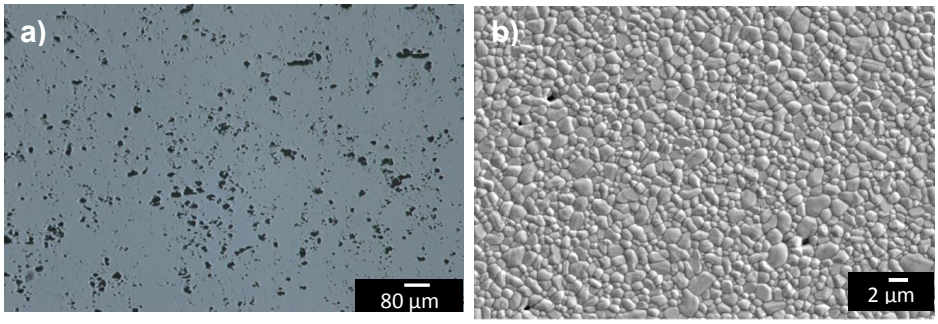

Figure 6-42 Microstructure of NWO55.

The creep rates obtained for NWO55 are presented in Appendix D, while the Arrhenius plots for stresses of 20, 40 and 63 MPa in air are presented in Figure 6-43. The Arrhenius plot of LWO54 with the smallest grain size under the stress of 63 MPa is plotted for comparison.

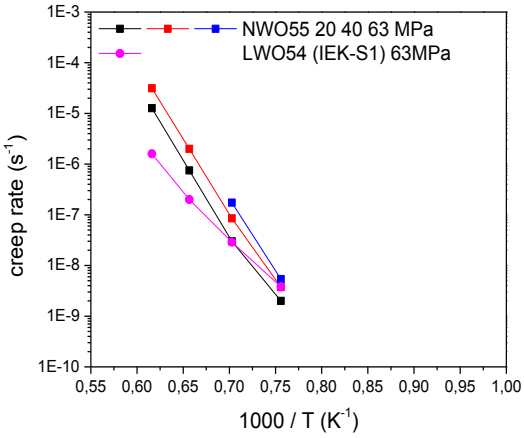

Figure 6-43 Arrhenius plots for NWO55 & LWO54 (IEK-S1) materials at 20, 40 and 63 MPa in air.

Similar to LWO54, measurable deformation rates were obtained at T ≥ 1050 °C for all stresses. The creep parameters were calculated similar as for the other materials and the results are presented in the Table 6-19.

Table 6-19 Creep parameters of NWO55

Stress	Q_a (kJ/mol)		Stress exponent *n*	
	1050 – 1250 °C	1250 – 1350 °C	Temperature (°C)	
20	495 ± 45	580	1050	0.9 ± 0.03
40	525 ± 20	565	1150	1.6 ± 0.03
63	544		1250	1.4
			1350	1.3

An average stress exponent of *n* = 1.3 ± 0.2 and an activation energy of Qa = 540 ± 30 kJ/mol suggests creep mechanism, similar as for LWO54 material. The stress exponent increases after 1150 °C. However, no significant change of the activation energy with temperature is observed similar to LWO54 with the smallest grain size (IEK-S1). The activation energy of NWO55 at 63 MPa for the temperature range 1250 – 1350 °C is higher than that of IEK-S1 material. Overall, NWO55 shows higher creep rates than LWO54 (IEK-S1), which could be attributed to the microstructure (smaller grains for NWO55).

Diffusivity studies by Vøllestad et al. [279] showed that enhanced grain boundary diffusion was the case in cation migration of this compound. The reason of this

behavior remains unclear and more investigations should be done for a deeper understanding. However, they suggested two possible explanations for the favoring of grain boundary diffusion: first could be that NWO55 possesses a crystal structure less cubic than the lanthanum-based tungsten oxides, thus the misfit and re-arrangement of the lattices around the grain boundaries enhances the grain boundary diffusion. The second explanation could be simply due to the microstructure: due to small grain size a higher concentration of grain boundaries is yielded. More investigations are necessary to clarify this behavior.

7 Conclusions

The results of the current work as well as suggestions for further work are separately summarized for the investigated materials in the following chapters. A comparison of these materials is also presented.

7.1 BSCF·Z100x

Micro-structural studies of BSCF·Z100x materials verified the suppression of grain growth with increasing amount of Zr doping. The solubility limit of Zr in BSCF matrix was found to be ~ 4 %. Above this value, the secondary phase (Ba/Sr)ZrO_3 forms mainly on the grain boundaries.

The derived activation energies and stress exponents imply that diffusional creep is the predominant mechanism for BSCF·Z100x ceramics at $T \geq 850$ °C. This was further supported by the fact that the grain-size-normalized creep rates vary little for the different BSCF·Z100x compounds. Doping with 10 % Zr was found to increase the stress exponent to ~ 4 indicating a transition from diffusional to power law creep.

The kinetics of the formation / dissolution of the hexagonal phase previously reported for BSCF was studied by high temperature XRD. The hysteresis loops observed during creep tests agree with the presence of the hexagonal phase in the structure. Zr doping does not seem to prevent the formation of this phase even in case of 10 % doping.

Hence, it was shown that creep resistance of BSCF is not improved by Zr doping. Moreover, the microstructure plays an important role with respect to the creep resistance as verified by a normalization of creep rates with respect to the grain size. Hence, it can be suggested that a modification of the microstructure (larger grains) might be a better strategy to obtain a more creep resistant material than doping.

Obviously, porosity which is a necessity for substrates that are used as support for the dense membrane layers will further increase the creep rates, hence having a potential to render doped BSCF unsuitable for the application as substrate material for dense oxygen transport membrane layers.

7.2 ST·F100x

The micro-indentation technique yielded, in good agreement with literature data, a room temperature Young's modulus of 170 ± 10 GPa and a fracture toughness of 0.92 ± 0.02 $\mathrm{MPa} \cdot \sqrt{\mathrm{m}}$ for all tested STF variants. Compressive tests indicated higher creep rates for ST·F70. Overall the materials were stable maintaining the cubic perovskite phase. This was partly verified by HT-XRD and creep testing; where no creep hysteresis was found, although limited specimens amount and thermally induced fracture of the ST·F50 specimen did not permit a verification of these findings for this composition. The activation energies are similar for all compounds with an average Q_a = 360 ± 40 kJ / mol and it seems that the Fe amount does not alter the activation energy significantly. Creep parameters yielded in case of ST·F50 and ST·F70 an average stress exponent n of 1.3 ± 0.2 indicating a diffusional mechanism, while for ST·F30 a higher n ~ 2 which increased at the higher testing temperature of 950 ° C suggests the contribution of an additional mechanism, i.e. above 950 °C a transition from diffusion to power law creep seems to appear (n = 2.4 ± 0.2).

A comparison with activation energies from literature derive either from creep tests or diffusivity studies revealed that the obtained values for ST·F100x compounds lie between the data reported for the end members of the ST·F100x range $SrFeO_3$ (Q_a = 260 ± 30 kJ/mol [204]) and $SrTiO_3$ (Q_a = 628 ± 24 kJ/mol [208]). This is indicating that the substitution of iron by Ti^{4+} changes the rate controlling species, while the doping amount does not seem to influence the activation energy.

In case of ST·F50 additional creep tests were also performed in vacuum, yielding similar creep rates like in air. However, slightly a lower activation energy was determined in vacuum for this material (280 ± 40 kJ/mol in vacuum compared to 340 kJ/mol in air). An oxygen partial pressure exponent close to zero was determined indicating that creep is independent of pO_2 under the respective testing conditions and, hence, since chemical strain gradients will not exist, the material is suitable for operation in oxygen partial pressure gradients. HT- XRD in similar atmospheres verified the similarity of chemical/thermal expansion in both atmospheres. Nevertheless, the effect of the overpressure on the stress state of the membrane has to be considered.

Overall, it seems that ST·F100x materials fulfill the 1 % strain [214] per year criterion that was suggested in literature for the stability under compressive creep conditions with lower creep rates than BSCF·Z3 and BSCF materials. Furthermore, stability under the application relevant conditions for the OXYFUEL process seems to be promising. Due to their lower creep rate, ST·F70, ST·F30 and ST·F50 seem to be better alternative to BSCF and BSCF·Z materials. Most important regarding the creep mechanism and its relation to pO_2 more investigations in wider pO_2 range should be performed. In order to see if the optimization of microstructure could further improve the creep resistance, given that the creep is governed by diffusion, systematic studies regarding the grain size should be performed. Again, regarding the application, the effect of porosity on creep needs to be investigated, since it can lead to higher creep rates exceeding the 1 % strain per year criterion.

7.3 LWO54

The room temperature Young's modulus determined using three different test methods is ~ 130 GPa, independent of grain size. A decrease in Young 'modulus by ~ 20 % was determined up to 1000 °C and this trend was again independent of the grain size. A slight kink was observed at 400 °C, possibly due to oxygen release from the lattice. Moreover, this behavior was the same in an Ar / 4 % H_2 atmosphere for the same temperature range.

Fracture toughness at room temperature from indentation tests was 1.07 ± 0.1 $MPa \cdot m^{½}$ for all tested materials.

Ring-on-ring bending tests revealed for dense LWO54 with a rather homogeneous microstructure a characteristic strength of σ_0 = 59 ± 3 MPa. It was shown that a factor ~ 2 higher strength value could be obtained for homogeneous microstructure (σ_0 =124 ± 6 MPa for dense LWO from IEK1 powder). Large agglomerates, irregular pores and pore zone areas were identified as strength limiting flaws by fractography. Strength was found to decrease by ~ 30 % up to 1000 °C. An unexpected strength increase by ~ 50 % at 400 °C was observed. Complementary annealing studies indicated a relationship to the onset of chemical / thermal expansion, where longer annealing leads to lower strength. However, further verification is necessary. The strength was independent of the loading rate. Hence, LWO54 does not seem to be prone to subcritical crack growth effects.

Extensive creep studies revealed that LWO54 creep is governed by cation diffusion as the predominant mechanism. The creep parameters were determined to n = 1.2 ± 0.3, p = 1.3 ± 0.4 Q_a = 370 ± 120 kJ / mol in the temperature and stress range 1050 – 1450 °C and 20 – 63 MPa, respectively. The activation energies were in good agreement with diffusion studies by Vøllestad et al [279] who suggested that the migration appears to be a combination of cations along grain boundaries and / or lattice.

LWO54 seems to fulfill the 1 % strain per year criterion [214]. Therefore, regarding creep it seems to be a suitable candidate material for application. Although diffusivity studies revealed lower proton diffusivities for Ar / 4 % H_2 atmosphere, creep experiments in the current work did not reveal any significant change in the creep rates under different atmospheres.

Regarding porous material it was shown that strength decreases almost linearly with increasing porosity for the investigated porosity regime (30 – 40 %). Therefore, an optimum porosity around ~ 30 % regarding strength could be suggested. The Weibull modulus was found to range from 10 – 20 (range is due to porosity and secondary phase) indicating a reliable manufacturing process with a homogeneous flaw distribution. Nevertheless, the manufacturing process can be further optimized, i.e. other parameters like grain size or pore formers that lead to different pore shapes could be examined. Since the material will be used in CO_2 environment, this aspect is also of great importance. The effect of porosity on creep is also of great importance for this material since it will lead to higher creep rates.

A brief study on the creep of the proton conductor NWO55 indicated that creep is again controlled by cation diffusion. An average stress exponent of n = 1.3 ± 0.2 and an activation energy Q_a = 540 ± 30 kJ/mol suggest diffusional creep similar to LWO54 material.

7.4 Comparison of materials

Figure 7-1 presents a comparison between creep rates of ST·F100x and well known perovskite membrane materials; $La_{0.6}Sr_{0.4}Co_{0.8}Fe_{0.2}O_{3-\delta}$ (LSCF [267]), $SrCo_{0.8}Fe_{0.2}O_{3-\delta}$ (SCF [205]), $Ba_{0.5}Sr_{0.5}Co_{0.8}Fe_{0.2}O_{3-\delta}$ (BSCF) [45] and $La_{0.5}Sr_{0.5}CoO_{3-\delta}$ (LSC) [281] at T = 900 °C and stress range 5 – 100 MPa:

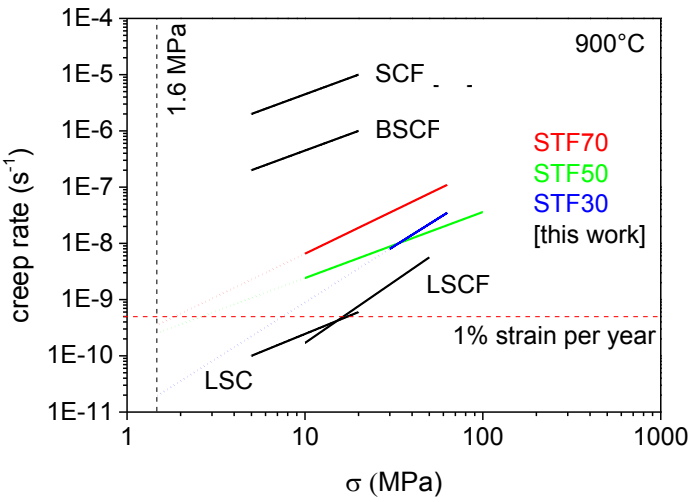

Figure 7-1 Norton plots for OTM materials at 900 °C [45,205,267,281].

It can be seen that ST·F100·X is a suitable alternative to BSCF regarding creep. In case of BSCF the 1 % strain per year criterion is exceeded [214]. At 900 °C an acceptable stress level to avoid exceeding the 1 % strain per year limit [214] is ~ 8 MPa for ST·F30. The equivalent stress for ST·F70 would be ~ 2 MPa. Naturally, at lower operational temperatures higher acceptable stress levels can be expected. Furthermore, contrary to BSCFZ which revealed hexagonal phase formation, the ST·F100x materials were verified to maintain their cubic phase at elevated temperatures It has to be emphasized that for substrates that need to have a porosity of 20 – 40 % for optimum transport towards the dense membrane layer, higher creep rates can be expected, as already verified for BSCFZ [254] and LSCF [282].

Figure 7-2 presents a comparison of the creep rates of BSCF [45] and BSCFZ [254] compounds with different microstructure [grain size (µm), porosity (%)] at T = 850 °C at 8 and 10 MPa in air and vacuum:

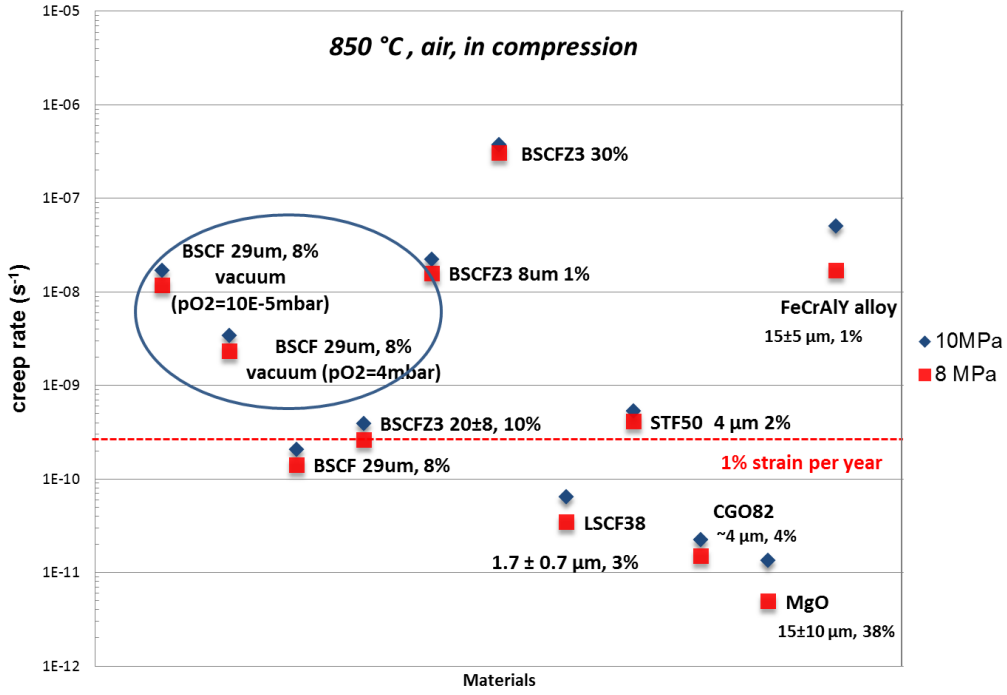

Figure 7-2 Creep rates in compression of oxygen transport membrane materials and possible substrate materials at 850 °C at 8 and 10 MPa [45,254,283].

Kriegel et al. [284] have suggested that for operation of membrane at 850 °C in air versus vacuum the tensile stresses are 8 - 10 MPa. The equivalent creep rates for the most important oxygen transport membrane materials are also presented in Figure 7-2. In this respect the creep rates of different dense and porous BSCF/BSCFZ compounds for the application relevant stresses of 8 and 10 MPa in air and vacuum at 850 °C are presented in Figure 7-2 (grain sizes, porosity and atmosphere, unless air was used, are given). It can be seen that the use of BSCF is not possible since the creep limit of 1 % per year [214] is exceeded in vacuum since the creep of this material has a strong dependence on the pO_2. In case of porous material creep rates are even higher. Also as it can be seen, regarding BSCF the creep rate might vary along the membrane since pO_2 will also vary. This effect should be investigated in further work.

Regarding ST·F50 the creep rates obtained in vacuum and in air were similar and the estimated oxygen partial pressure exponent was close to zero, indicating that the

material is also advantageous compared to BSCF/BSCFZ with respect to chemically induced strain.

The creep rates of different hydrogen transport membrane materials for stresses of 30 - 40 MPa are compared in Figure 7-3. The creep rates depend almost linearly on temperature and can thus be easily extrapolated to the application relevant temperature range 600 – 800 °C, where they are lower than the 1 % strain per year limit [214].

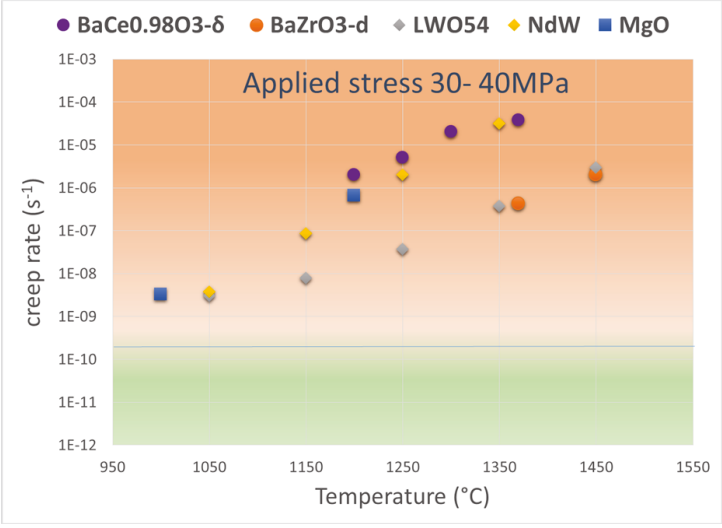

Figure 7-3 Creep rates of hydrogen transport membrane and substrate materials [194,195].

8 Appendix A

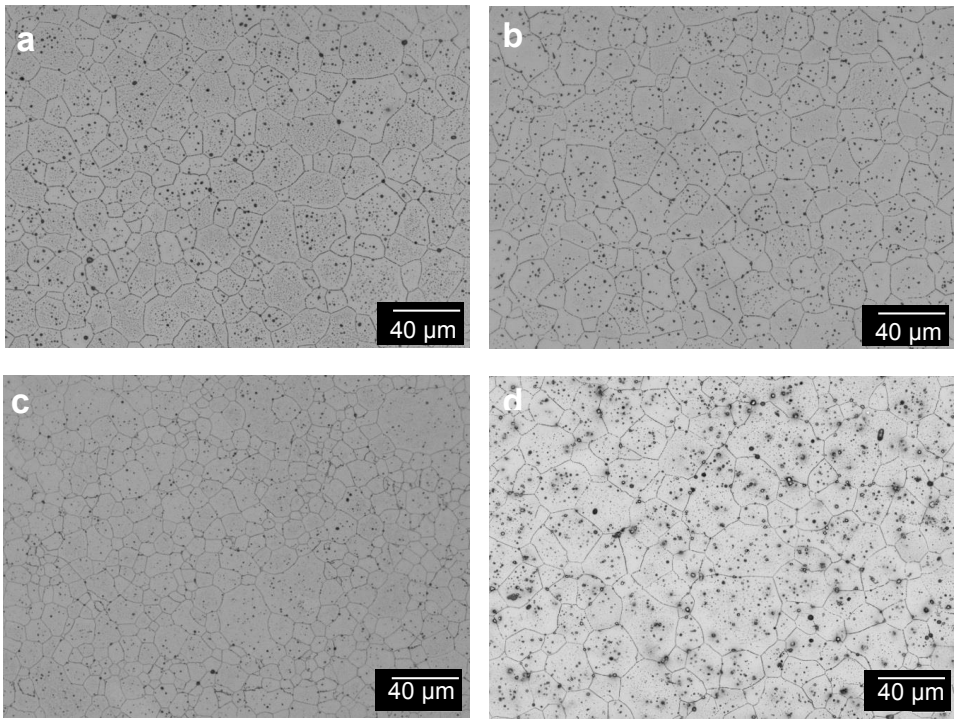

Figure 8-1 Light Microscope Images of reference samples used for the grain size analysis a) BSCF b) BSCF·Z1 c) BSCF·Z3 d) BSCF·Z5

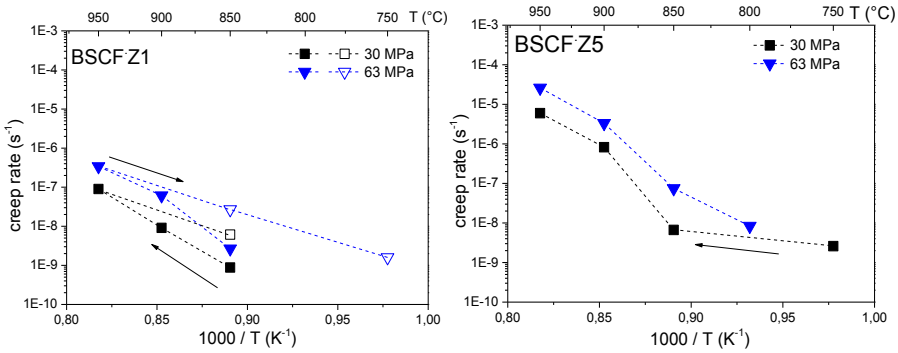

Figure 8-2 Temperature dependence of the steady-state creep rate for (left) BSCF-Z3 and (right) BSCF-Z10 at nominal stresses of 30 and 63 MPa. The arrows indicate heating and cooling directions. The closed shapes represent heating and open ones the cooling sequence

Table 8-1 Creep rates of BSCF·Z100x series obtained in current work (only validate creep rates are presented that are not close to measurement resolution)

Material	Stress (MPa)	Heating / cooling sequence	$\dot{\varepsilon}$ obtained at the temperature of:				
			750°C	800°C	850°C	900°C	950°C
BSCF [45]	29	Heating		$1.5\cdot10^{-9}$	$2.3\cdot10^{-9}$	$4.9\cdot10^{-8}$	$2.6\cdot10^{-7}$
BSCF·Z1	30	Heating	$5.1\cdot10^{-11}$	-	$8.8\cdot10^{-11}$	$9.1\cdot10^{-9}$	$9.0\cdot10^{-8}$
		Cooling	-	-	$6.1\cdot10^{-9}$	-	$9.0\cdot10^{-8}$
BSCF·Z3		Heating		$2.6\cdot10^{-9}$	$3.4\cdot10^{-9}$	$2.8\cdot10^{-7}$	$2.3\cdot10^{-6}$
		Cooling		$5\cdot10^{-9}$	$1.1\cdot10^{-7}$	$7.1\cdot10^{-7}$	$2.3\cdot10^{-6}$
BSCF·Z5		Heating		-	$6.7\cdot10^{-9}$	$8.2\cdot10^{-7}$	$5.6\cdot10^{-6}$
		Cooling		-	-	-	$5.6\cdot10^{-6}$
BSCF·Z10		Heating	$6.8\cdot10^{-9}$	$1.3\cdot10^{-8}$	$1.5\cdot10^{-8}$	$1.8\cdot10^{-7}$	$6.0\cdot10^{-6}$
		Cooling	-	-	$4.9\cdot10^{-8}$	$6.1\cdot10^{-7}$	$6.0\cdot10^{-6}$
BSCF·Z1	63	Heating	-	-	$2.7\cdot10^{-9}$	$6.1\cdot10^{-8}$	$3.4\cdot10^{-7}$
		Cooling	-	-	$2.7\cdot10^{-8}$	-	$3.4\cdot10^{-7}$
BSCF·Z3		Heating	-	$3.5\cdot10^{-9}$	$1.1\cdot10^{-8}$	$9.1\cdot10^{-7}$	$5.6\cdot10^{-6}$
		Cooling	$8.7\cdot10^{-10}$	$6.5\cdot10^{-9}$	$3.3\cdot10^{-7}$	$1.5\cdot10^{-6}$	$5.6\cdot10^{-6}$
BSCF·Z5		Heating	-	$8.4\cdot10^{-9}$	$7.5\cdot10^{-8}$	$3.3\cdot10^{-6}$	$2.6\cdot10^{-5}$
		Cooling	-	-	-	-	-
BSCF·Z10		Heating	$7.5\cdot10^{-9}$	$1.2\cdot10^{-8}$	$6.7\cdot10^{-8}$	$1.33\cdot10^{-5}$	$1.1\cdot10^{-4}$
		Cooling	$4.6\cdot10^{-9}$	-	$2.3\cdot10^{-6}$	$1.8\cdot10^{-5}$	$1.1\cdot10^{-4}$

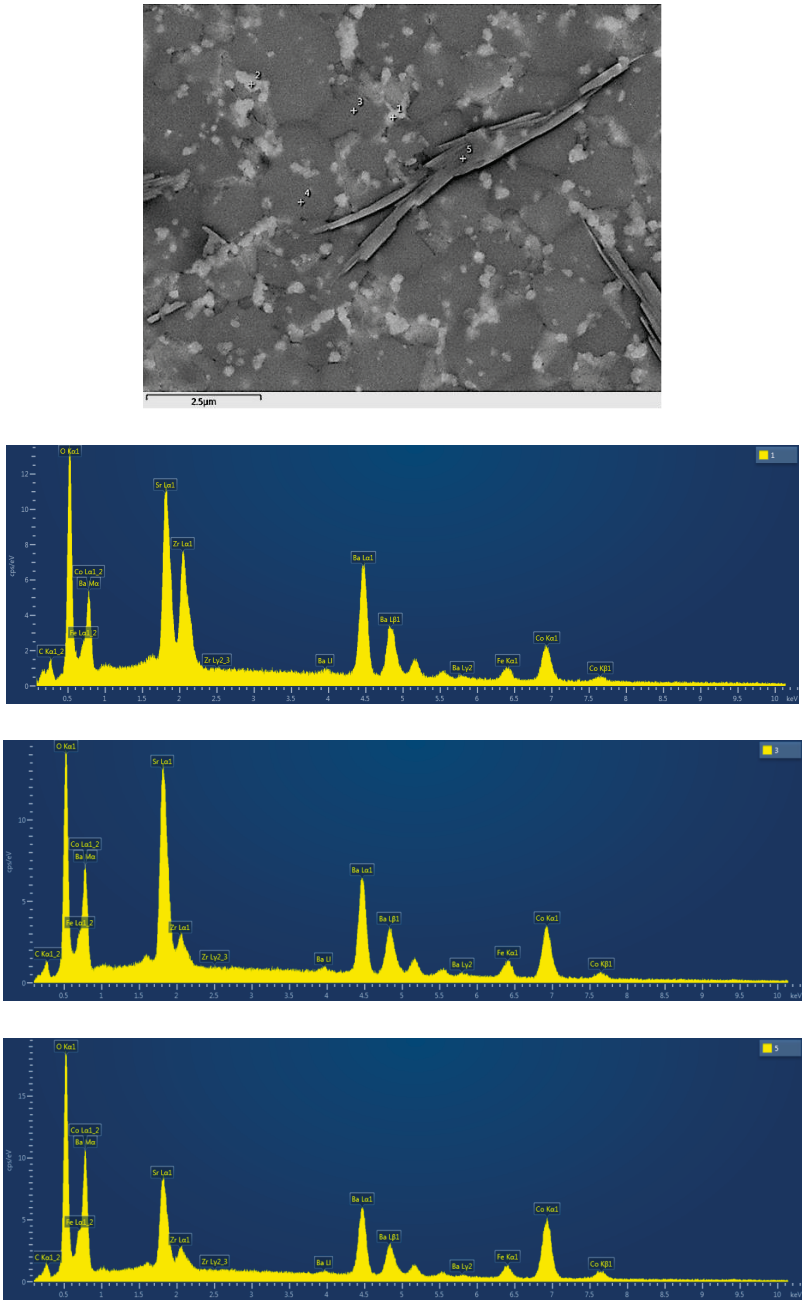

Figure 8-3 BSCF·Z10 microstructure (BSE) after creep test (final step 850°C 63 MPa) and EDX analysis Point 1: (Ba/Sr)ZrO_3 perovskite phase Point 3: BSCF cubic (matrix) Point 5: Hexagonal phase (verified by XRD)

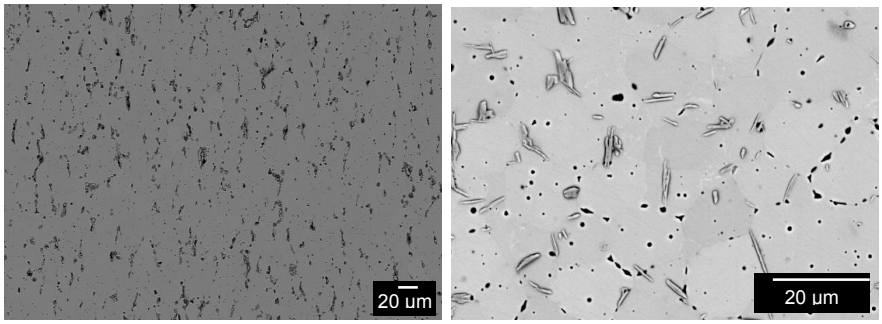

Figure 8-4 Microstructure of BSCF·Z1 (left) (final step 750°C 63 MPa) and BSCF·Z5 (right) (final step 950°C 63 MPa)

Table 8-2 Secondary phases observed in the BSCF·Z100x materials after the creep tests

	Sintering conditions T_{sint} (°C) / time (h)	Secondary phases after creep test		
		T of last step	XRD	SEM
BSCF	1120/30	850 °C heating	$Ba_{0.5}Sr_{0.5}CoO_3$ (40%) , $Ba_2Fe_2O_5$	-
BSCF·Z1	1120/30	750 °C cooling	cubic	Different phase at GB
BSCF·Z3	1050/3	750 °C cooling	Cubic, $Ba_{0.5}Sr_{0.5}CoO_3$	GB
BSCF·Z5	1120/30	950 °C heating	Cubic, $Ba_{0.5}Sr_{0.5}CoO_3$, $Ba_2Fe_2O_5$	-
BSCF·Z10	1120/30	850 °C cooling	Cubic, $Ba_{0.5}Sr_{0.5}CoO_3$, $(Ba/Sr)ZrO_{3-\delta}$	$(Ba/Sr)ZrO_{3-\delta}$ at GB

9 Appendix B

Table 9-1 Creep rates for ST·F100x materials

Material	Stress (MPa)	pO_2 (mbar)	Creep rates (s^{-1}) obtained at the temperature of:					
			800°C	850°C	900°C	950°C	1000°C	Cooling 850°C
STF_30	10	200	-	-	-	$3.2*10^{-9}$	-	
	30		-	-	$8.0*10^{-9}$	$6.0*10^{-8}$ $6.5*10^{-8}$	-	
	35		-	$2.5*10^{-9}$	-	-	-	
	50		-	-	$2.2*10^{-8}$	$1.9*10^{-7}$ $1.7*10^{-7}$	-	
	56		-	$7.1*10^{-9}$	-	-	-	
	63		-	-	$3.5*10^{-8}$	-	-	$4.5*10^{-9}$
	70		-	1. $*10^{-8}$	-	-	-	
STF_50	10	200	-	-	$2.3*10^{-9}$	-	-	
	30		$4.0*10^{-10}$	$2.0*10^{-9}$	$9.4*10^{-9}$ $9.5*10^{-9}$	-	$1.27*10^{-7}$	
	50		-	-	$1.8*10^{-8}$	-	-	
	63		$9.2*10^{-10}$	$5.8*10^{-9}$	$2.0*10^{-8}$	-	-	
	80		-	-	$2.7*10^{-8}$	-	-	
	30	10^{-5}	$9.7*10^{-10}$	$1.9*10^{-9}$	$5.13*10^{-9}$	$2.3*10^{-8}$	-	
	50		-	-	$1.12*10^{-8}$	-	-	
	63		-	-	$1.3*10^{-8}$	-	-	
STF_70	10	200	-	-	$6.1*10^{-9}$	$3.25*10^{-8}$	-	-
	30		-	-	$4.2*10^{-8}$		-	-
	35		-	$1.0*10^{-8}$	$5.3*10^{-8}$	$2.0*10^{-7}$	-	$7.5*10^{-9}$
	50		-	$1.9*10^{-8}$	$7.6*10^{-8}$	-	-	-
	63		-	$2.2*10^{-8}$ $1.7*10^{-8}$	$1.0*10^{-7}$	-	-	$1.6*10^{-8}$

10 Appendix C

Table 10-1 Powder characteristics of LWO54 materials and samples details

Microstructural data		IEK-S2	CPT-D1	CPT-D2
Porosity (%)		3 ± 1	9 ± 4	6 ± 1
Phases in sintered samples (XRD, EDX)		$La_{5.4}WO_{12-\delta}$	$La_{5.4}WO_{12-\delta}$, $La_{10}(SiO_4)_6O_3$, Ba	$La_{5.4}WO_{12-\delta}$
Sintering conditions (T_{sint}/ dwelling time °C/h)		1500 / 12	1500 / 15	1500 / 15
Grain size		11 ± 4	9 ± 3	17 ± 6
Powder characteristics	XRD	$La_{5.4}WO_{12-\delta}$	$La_{5.4}WO_{12-\delta}$ La_2O_3	$La_{5.4}WO_{12-\delta}$ La_2O_3
	BET area (m^2/g)	1.9	3.3	12
	Name	IEK1	C3-77	P1-21
	D_{50} (µm)	1.2	1.1-	0.83
Samples		Ø 22mm, h~1.7mm, defect free	Ø21mm, h~0.7mm , anomaly in surface, impression in the middle	Ø20mm h~1.5mm anomalies need ZEA-1 h ~ 0.5 after ZEA-1

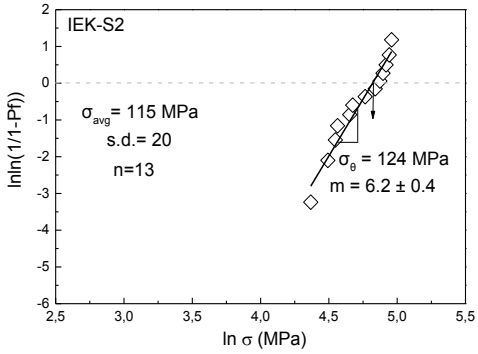

Figure 10-1 Weibull plot for LWO54 at room temperature (batch IEK-S2)

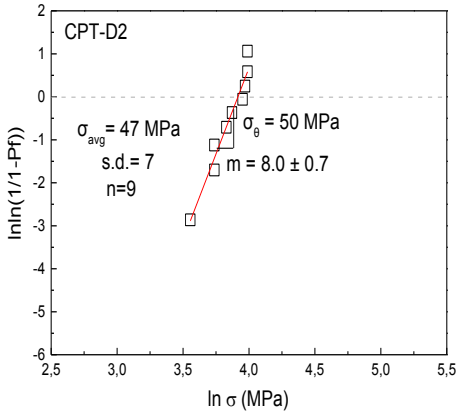

Figure 10-2 Weibull plot for LWO54 at room temperature (batch CPT-D2)

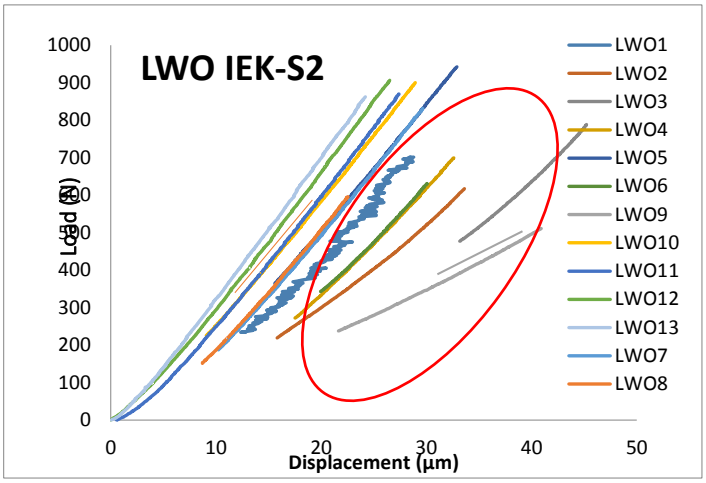

Figure 10-3 Load – Displacement curves for LWO54 (batch IEK-S2) obtained from ring-on-ring bending test at room temperature. The straight lines belong to the samples with prepared surface before the test while the ones in the circle belong to the samples that were tested as received.

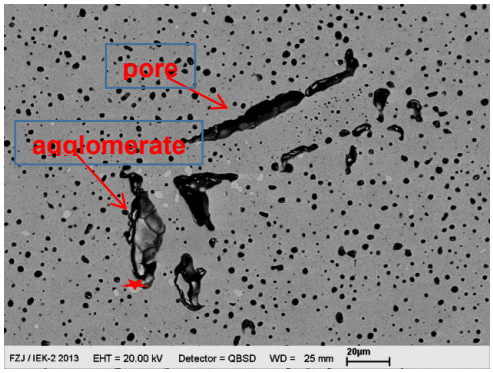

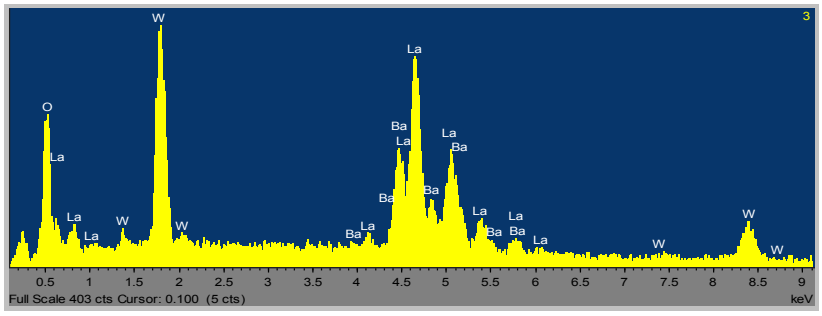

Figure 10-4 Cross section of LWO54 (CPT-D1 batch) after sintering showing irregular pore and agglomerates in the bulk of the material. EDX analysis revealed secondary phase rich in Ba

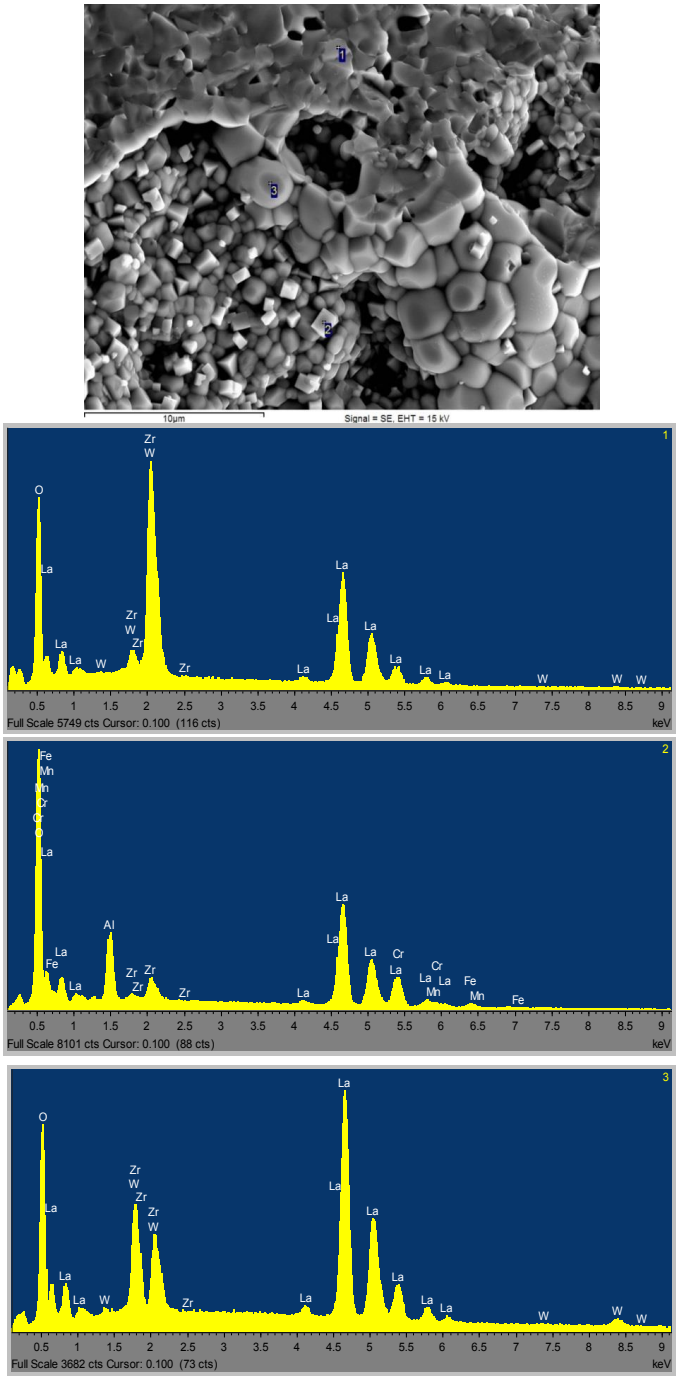

Figure 10-5 EDX analysis of fracture surface of LWO54 (batch CPT-D2) after heating at 1000 °C. A crack around a pore zone was observed where segregation of contaminations Zr, Fe, Cr, Al was detected as fine grains.

Table 10-2 Creep rates (s^{-1}) for LWO54 materials

Stress (MPa)	pO_2 (mbar)	Batch / Grain size (µm)	Creep rates (s^{-1}) obtained at the temperature of:					
			1000°C	1050°C	1150°C	1250°C	1350°C	1450°C
20	200	IEK-S1 6 ± 3	-	-	-	$5.20 \cdot 10^{-8}$	$3.95 \cdot 10^{-7}$	-
40				-	-	$1.10 \cdot 10^{-7}$	$7.90 \cdot 10^{-7}$	-
63				$3.77 \cdot 10^{-9}$	$2.89 \cdot 10^{-8}$	$2.00 \cdot 10^{-7}$	$1.6 \cdot 10^{-6}$	-
20	200	IEK-S2 11 ± 4		$1.96 \cdot 10^{-9}$	$4.23 \cdot 10^{-9}$	$1.86 \cdot 10^{-8}$	$1.16 \cdot 10^{-7}$	$1.14 \cdot 10^{-6}$
40	200			$3.00 \cdot 10^{-9}$	$7.90 \cdot 10^{-9}$	$3.66 \cdot 10^{-8}$	$3.74 \cdot 10^{-7}$	$2.90 \cdot 10^{-6}$
63	200			$4.00 \cdot 10^{-9}$	$1.1 \cdot 10^{-8}$	-	-	-
20	200	CPT-D2 17 ± 6	-	-	-	-	$9.85 \cdot 10^{-8}$	-
40	200		-	-	-	$2.28 \cdot 10^{-8}$	$2.73 \cdot 10^{-7}$	-
63	200		$1.30 \cdot 10^{-10}$	-	$3.78 \cdot 10^{-9}$	$4.48 \cdot 10^{-8}$	$7.00 \cdot 10^{-7}$	-

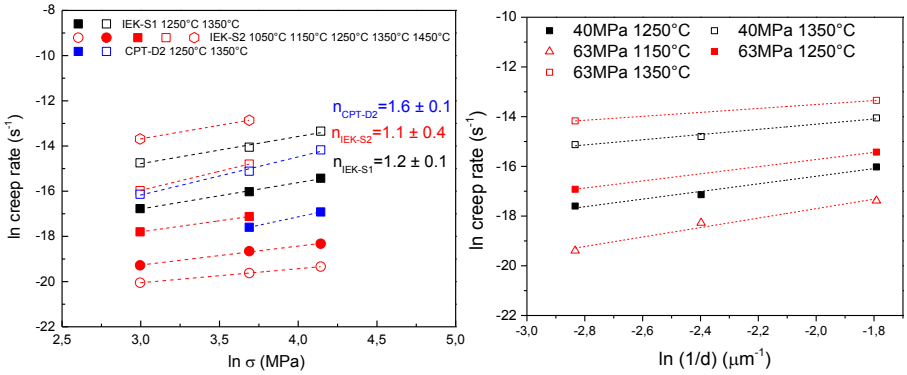

Figure 10-6 Determination of creep parameters for LWO54 materials stress exponent (left) inverse grain size exponent (right)

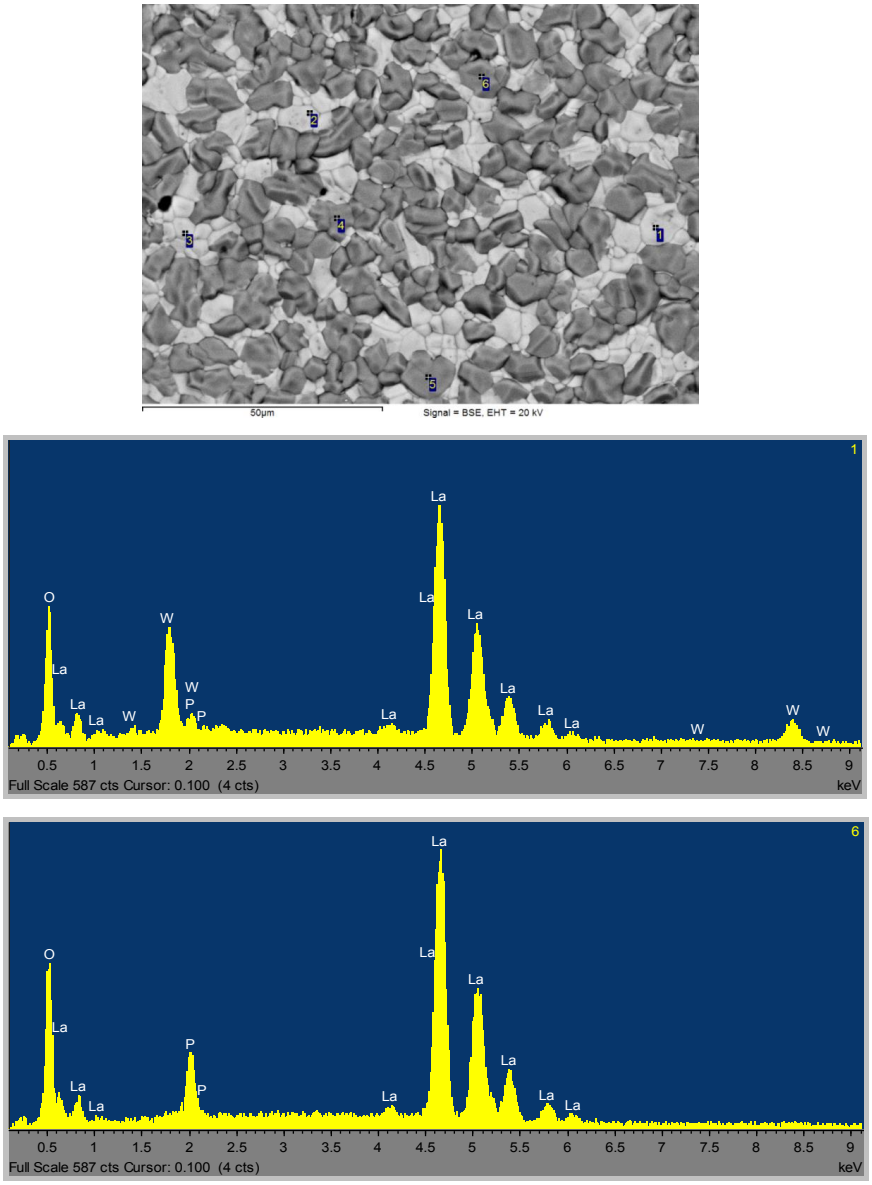

Figure 10-7 SEM Backscattered Image and EDX analysis of LWO54 (IEK-S2) after creep test at 1450°C (surface of sample) Two phases are distinguished, main phase (white) and depleted in W (dark).

11 Appendix D

Table 11-1 Creep rates for NWO55 in air

Stress (MPa)	**pO_2 (mbar)**	**Grain size (µm)**	**Creep rates (s^{-1}) obtained at the temperature of:**				
			900 °C	1050 °C	1150 °C	1250 °C	1350 °C
10	200		-	-	$9.2 \cdot 10^{-9}$	-	-
20			-	$2.0 \cdot 10^{-9}$	$3.0 \cdot 10^{-8}$	$7.5 \cdot 10^{-7}$	$1.3 \cdot 10^{-5}$
40			-	$3.7 \cdot 10^{-9}$	$8.5 \cdot 10^{-8}$	$2.0 \cdot 10^{-6}$	$3.1 \cdot 10^{-5}$
63			$8.9 \cdot 10^{-10}$	$5.4 \cdot 10^{-9}$	$1.7 \cdot 10^{-7}$		

12 References

[1] Gibbins J., Chalmers H., 'Carbon Capture and Storage', Energy Policy, 36 (2008) 4317-4322

[2] I.E. Agency, Technology Roadmap. Carbon capture and storage OECD/IEA (2009)

[3] Czyperek M., Zapp P., Bouwmeester H.J.M., Modigell M., Peinemann K.V., Voigt I., Meulenberg W.A., Singheiser L., Stöver D., 'MEM-BRAIN gas separation membranes for zero-emission fossil power plants' Energy Procedia 1 (2009) 303-310

[4] Kanniche M., Gros-Bonnivard, Jaud P., Valle-Marcos, Amann J.M., Bouallou C., 'Pre-combustion, post-combustion and oxy-combustion in thermal power plant for CO2 capture' Applied Thermal Engineering 30 (2010) 53-62

[5] Berstad D., Anantharaman R., Neksa P., 'Low-temperature CO_2 capture technologies: Applications and potential', International Journal of Refrigeration 36 (2013) 1403-1416

[6] http://www.globalccsinstitute.com

[7]http://energy.gov/fe/science-innovation/carbon-capture-and-storage-research/carbon-capture-rd/pre-combustion-carbon

[8] Modigell M., OXYCOAL-AC: 'Oxyfuel power plant concepts for gas separation with oxygen transport membranes', 9. Jülicher Werkstoffsymposium, 15-16 November 2007

[9] Higginbotham P., White V., Fogash K., Guvelioglou G.,' Oxygen Supply for Oxycoal CO_2 Capture' Energy Procedia 4 (2011) 884-891

[10] Tigges F.K.K.D., Bergins C., Busekrus K., Niesbach J., Ehmann M., Kuhr F.H.C., Vollmer B., Buddenberg T., Wu S., Kukoski A., 'Conversion of existing coal-fired power plants to oxyfuel combustion: Case study with experimental results and CFD-simulations' Energy Procedia 1 (2009) 549-556

[11] Matsumoto H., Shimura T., Iwahara H., Higuchi T., Yashiro K., Kaimai A., 'Hydrogen separation using proton-conducting perovskites' Journal Alloys and Compounds. 408-412 (2006) 456-462

[12] J. Sunarso, S. Baumann, J.M. Serra, W.A. Meulenberg, S. Liu, Y.S. Lin, J.C. Diniz da Costa, 'Mixed ionic-electronic conducting (MIEC) ceramic-based membranes for oxygen separation', Journal of Membrane Science 320 (2008) 13–41

[13] E.T. Robinson, 'Oxygen transport membranes for ultra-clean fuel production', Fuel Chemistry Division Preprints 48 (2003) 347–349

[14] M. Czyperek, P. Zapp, H.J.M. Bouwmeester, M. Modigell, K. Ebert, I. Voigt, W.A. Meulenberg, L. Singheiser, D. Stöver, 'Gas separation membranes for zero-emission fossil power plants: MEM-BRAIN', Journal of Membrane Science 359 (2010) 149–159

[15] Baumann S., Serra J.M, Lobera M.P., Escolástico S., Schulze-Küppers F., Meulenberg W.A., 'Ultra high permeation flux through supported $Ba_{0.5}Sr_{0.5}Co_{0.8}Fe_{0.2}O_{3-\delta}$ membranes', Journal of Membrane Science, 377 (2011) 198-205

[16] Bouwmeester H.J.M., Burggraaf A.J., 'Dense Ceramic Membranes for Oxygen Separation' (Chapter 14) Handbook of Solid State Electrochemistry,CRC Press, Inc (1997)

[17] http://www.cfn.kit.edu/deutsch/661.php

[18] Wagner C, 'Über den Mechanismus der electrischen Stromleitung im Nerststifft Naturwissenschaften' 31 (1943) 265-268

[19] Bouwmeester H.J.M.,Burgraaf, 'Dense ceramic membranes for oxygen separation' in A.J. Burggraaf, L.Cot (Eds) Fundamentals of Inorganic Membrane Science and technology, Elsevier, Amsterdam, 1996 pp 435-528

[20] Sunarso J., Liu S., Lin YS., Diniz da Costa JC., 'Oxygen permeation performance of $BaBiO_{3-\delta}$ ceramic membranes' Journal of Membrane Science 344 (2009) 281

[21] Watanabe K., Takauchi D., Yussa M., Kida T., Shimanoe K., Teraoka Y., 'Oxygen Permeation Properties of Co-Free Perovskite-Type Oxide Membranes Based on $BaFe_{1-y}Zr_yO_{3-\delta}$' Journal of Electrochemical Society 156 (2009) 81-85

[22] Shao ZP, Yang WS, Cong Y, Dong H, Tong JH, Xiong GX. 'Investigation of the permeation behavior and stability of a $Ba_{0.5}Sr_{0.5}Co_{0.8}Fe_{0.2}O_{3-\delta}$ oxygen membrane' Journal of Membrane Science 172 (2000) 177-178

[23] Kharton VV, Viskup AP, Kovalevsky AV, Naumovich EN, Marques FMB.'Ionic transport in oxygen-hyperstoichiometric phases with K2NiF4-type structure' Solid State Ionics 143 (2001) 337.

[24] Kharton VV, Kovalevsky AV, Tsipis EV, Viskup AP, Naumovich EN, Jurado JR Fredo J., 'Mixed conductivity and stability of A-site-deficient $Sr(Fe,Ti)O_{3-\delta}$ perovskites'. Journal Solid State Electrochemistry 7 (2002) 30-36

[25] Goldschmidt, V.M., Akad. Oslo., 1946, A42, 224

[26] James M., Cassidy D., Wilson KF., Horvat J., Withers RL., 'Oxygen Vacancy Ordering and Magnetism in the Rare Earth Stabilized Perovskite Form of $SrCO_{3-\delta}$' Solid State Sciences 6 (2004) 655-662

[27] Zhu XF., Wang HH., Yang WS., 'Novel cobalt-free oxygen permeable membrane' Chemical Communications 9 (2004) 1130

[28] Zeng PY., Ran R., Chen ZH Gu HX, Shao ZP., Liu SM., 'Novel mixed conducting $SrSc_{0.05}Co_{0.95}O_{3-\delta}$ ceramic membrane for oxygen separation' AIChE 53 (2007) 3116-3124

[29] Zeng PY, Ran R., Chen ZH., Gu HX, Shao ZP., Liu SM 'Efficient stabilization of cubic perovskite $SrCoO_{3-\delta}$ by B-site low concentration scandium doping combined with sol–gel synthesis' Journal Alloy and Compounds 455 (2008) 465-470

[30] Wang H., Cong Y., Yang WS., 'Oxygen permeation study in a tubular $Ba_{0.5}Sr_{0.5}Co_{0.8}Fe_{0.2}O_{3-\delta}$ oxygen permeable membrane' Journal Membrane Science 210 (2002) 259-271

[31] Iwara H., Esaka T., Uchida H., Maeda N., 'Proton conduction in sintered oxides and its applications to steam electrolysis for hydrogen production'. Solid State Ionics, 3-4 (1981) 359-363

[32] Colomban P.,'Proton Conductors: Solids, Membranes, and Gel-Materials and Devices'. (1992) Cambridge, UK: Cambridge University Press

[33] Norwick A.S. Du Y., 'High-temperature protonic conductors with Perovskite-related structures' Solid State Ionics 77 (1995) 137-146

[34] Hashim S.M., Mohamed A.R., Bhatia S., 'Current Status of ceramic-based membranes for oxygen separation from air', Advances in Colloid and Interface Science 160 (2010) 88-100

[35] Teraoka Y., Zhang H., Yamazone N., 'Oxygen-sorptive properties of defect perovskite-type $La_{1-x}Sr_xCo_{1-x}Fe_yO_{3-\delta}$', Chemical Letters, (1985) 1367-1370

[36] Teraoka Y., Zhang H., Furukawa S., Yamazone N., 'Oxygen-permeation through perovskite type oxide' Chemical Letters 1985, 1743-1746

[37] Teraoka Y., Zhang H., Okamoto K., Yamazone, 'Mixed ionic-electronic conductivity of $La_{1-x}Sr_xCo_{1-y}Fe_yO_{3-\delta}$ perovskite type oxides' Materials Research Bulletin 23 (1988) 51-58

[38] Yokokawa, Sakai N., Kawada T., Dokiya M., 'Thermodynamic stabilities of perovskite oxides for electrodes and other electrochemical materials' Solid State Ionics, 52 (1992) 43-56

[39] Kruidhof H., Bouwmeester H.J.M., Vondoorn R.H.E., Burggraaf, 'Influence of order-disorder transitions on oxygen permeability through selected nonstoichiometric perovskite-type oxides' Solid State Ionics, 63-65 (1993) 816-822

[40] Vente J.F., McIntosh S., Haije W.G., Bouwmeester H.J.M., 'Properties and performance of $Ba_xSr_{1-x}Co_{0.8}Fe_{0.2}O_{3-\delta}$ materials for oxygen transport membranes' Journal of Solid State Electrochemistry 10 (2006) 581-588

[41] Shao Z.P., Xiong G.X., Tong J.H., Dong H., Yang W.S., 'Ba effect in doped $Sr(Co_{0.8}Fe_{0.2})O_{3-\delta}$ on the phase structure and oxygen permeation of properties of the dense ceramic membranes', Separation and Purification Technology 25 (2001) 419-429

[42] Shao Z., Yang W., Cong Y., Dong H., Tong J., Xiong G., 'Investigation of the permeation behavior and stability of a $Ba_{0.5}Sr_{0.5}Co_{0.8}Fe_{0.2}O_{3-\delta}$ oxygen membrane', Journal Membrane Science 172 (2000) 177-188

[43] Niedrig C., Taufall S., Burriel M., Menesklou W., Wagner S., Baumann S., Ivers-Tiffee E., 'Thermal stability of the cubic phase in $Ba_{0.5}Sr_{0.5}Co_{0.8}Fe_{0.2}O_{3-\delta}$ (BSCF)', Solid State Ionics 197 (2011) 25-31

[44] Li X., Kerstiens T., Markus T., 'Oxygen permeability and phase stability of $Ba_{0.5}Sr_{0.5}Co_{0.8}Fe_{0.2}O_{3-\delta}$ perovskite at intermediate temperatures, Journal of Membrane Science 438 (2013) 83-89

[45] Rutkowski B., Malzbender J., Beck T., Steinbrech R.W., Singheiser L., 'Creep behaviour of tubular $Ba_{0.5}Sr_{0.5}Co_{0.8}Fe_{0.2}O_{3-\delta}$ gas separation membranes', Journal of the European Ceramic Society 31 (2011) 493-499

[46] Dyer P., Richards R., Russek S.L., Taylor D. 'Ion transport membrane technology for oxygen separation and syngas production', Solid State Ionics 34 (2000) 21-33

[47] Czyperek M., Zapp P., Bouwmeester H.J.M., Modigell, M., Ebert K., Voigt I., Meulenberg W.A., Singheiser L., Stöver D., 'Gas separation membranes for zero-emission fossil power plants': MEM-BRAIN Journal. Of Membrane Science. 359 (2010) 149-159

[48] Liang F., Jiang H., Luo H. Caro J., Feldhoff A., 'Phase Stability and Permeation Behavior of a Dead-End $Ba_{0.5}Sr_{0.5}Co_{0.8}Fe_{0.2}O_{3-\delta}$ 'Tube Membrane in High-Purity Oxygen Production', Chemistry of. Materiasls., 23 (2011) 4765-4772

[49] Shao Z., Yang W., Cong Y., Dong H., Tong J., Xiong G., 'Investigation of the permeation behavior and stability of a $Ba_{0.5}Sr_{0.5}Co_{0.8}Fe_{0.2}O_{3-\delta}$ oxygen membrane' Journal of. Membrane. Science 172 (2000) 177-188

[50] Švarcová S., Wiik K., Tolchard J., Bouwmeester H.J.M., Grande T., 'Structural instability of cubic perovskite $Ba_xSr_{1-x}Co_{1-y}Fe_yO_{3-\delta}$', Solid State Ionics 178 (2008) 1787-1791

[51] Müller D.N., De Souza R.A., Weirich T.E., Röhrens D., Mayer J., Martin M., 'A kinetic study of the decomposition of the cubic perovskite-type oxide $Ba_xSr_{1-x}Co_{0.8}Fe_{0.2}O_{3-\delta}$ (BSCF) (x = 0.1 and 0.5), Physical. Chemistry Chemical Physics. 12 (2010) 10320-8

[52] Efimov K., Xu Q., Feldhoff A., 'Transmission Electron Microscopy Study of $Ba_{0.5}Sr_{0.5}Co_{0.8}Fe_{0.2}O_{3-\delta}$ Perovskite Decomposition at Intermediate Temperatures', Chemisty .of Materials. 22 (2010) 5866-5875

[53] Müller P., Störmer H., Meffert M., Dieterle L., Niedrig C, Wagner S.F., Ivers-Tiffée E., Gerthsen D., 'Secondary Phase Formation in $Ba_{0.5}Sr_{0.5}Co_{0.8}Fe_{0.2}O_{3-d}$ Studied by Electron Microscopy'. Chemistry.of Materials 25 (2013) 564-573

[54] Engels L., Markus T., Modigell M., Singheiser L., 'Oxygen permeation and stability investigations on MIEC membrane materials under operating conditions for Power-Plant-Processes', Journal of Membrane Science 370 (2011) 59-69

[55] Arnold M., Wang H.H., Feldhoff A., 'Influence of CO_2 on the oxygen permeation performance and the microstructure of perovskite-type $(Ba_{0.5}Sr_{0.5})$ $(Co_{0.8}Fe_{0.2})O_{3-\delta}$ membranes', Journal of Membrane Science 293 (2007) 44-52

[56] Yan A.Y., Yang M., Hou Z.F., Dong Y.L., Cheng M.J., 'Investigation of $Ba_{1-x}Sr_xCo_{0.8}Fe_{0.2}O_{3-\delta}$ as cathodes for low-temperature solid oxide fuel cells both in the absence and presence of CO_2', Journal of Power Sources 185 (2008) 76-84

[57] Haworth P., Smart S., Glasscock J., Diniz da Costa J.C., 'Yttrium doped BSCF membranes for oxygen separation' Separation and Purification Technology 81 (2011) 88–93

[58] Fang S:M., Yoo C.Y., Bouwmeester H.J.M.,'Performance and stability of niobium-substituted $Ba_{0.5}Sr_{0.5}Co_{0.8}Fe_{0.2}O_{3-\delta}$ membranes' Solid State Ionics 195 (2011) 1–6

[59] Meng X., Yang N., Meng B., Tan X., Ma Z., Liu S., 'Zirconium stabilized $Ba_{0.5}Sr_{0.5}(Co_{0.8-x}Zr_x)Fe_{0.2}O_{3-\alpha}$ perovskite hollow fibre membranes for oxygen separation' Ceramics International 37 (2011) 2701-09

[60] Yakovlev S., Yoo C.Y., Fang S., Bouwmeester H.J.M., 'Phase transformation and oxygen equilibration kinetics of pure and Zr-doped $Ba_{0.5}Sr_{0.5}$ $Co_{0.8}Fe_{0.2}O_{3-\delta}$ perovskite oxide probed by electrical conductivity relaxation' Applied Physics Letters 96 (2010) 254101-3

[61] Ravkina O., Klande T., Feldhoff A., 'Investigation of Zr-doped BSCF perovskite membrane for oxygen separation in the intermediate temperature range', Journal of Solid State Chemistry 201 (2013) 101-6

[62] Pei, S., Kleefisch, M.S., Kobylinski, T.P., Faber, K., Udovich, C.A., Zhang-McCoy, V., Dabrowski, B., Balachandran, U., Mieville, R.L., and Poeppel, R.B., 'Failure mechanisms of ceramic membrane reactors in partial oxidation of methane to synthesis gas', Catalysis Letters, 30 (1995) 210–212

[63] Kharton V.V., Figueiredo F.M., Kovalevsky A.V., Viskup A.P., Naumovich E.N., Jurado J.R., Frade J.R. 'Oxygen Diffusion and thermal expansion of $SrTiO_{3-\delta}$ and $CaTiO_{3-\delta}$ based materials'. Defect and Diffusion Forum 186-187 (2000) 119-136

[64] Kharton V.V., Kovalevsky, Viskup A.P., Jurado J.R., Figueiredo F.M., Naumovich E.N., Frade J.R., 'Transport properties and thermal expansion of $Sr_{0.97}Ti_{1-x}Fe_xO_{3-\delta}$ (x=0.2-0.8)', Journal of Solid State Chemistry 156 (2001) 437-444

[65] Mazanec T.J., Cable T.L., Frye J.G., Kliewer W.R., 'Solid multi-component membranes, electrochemical reactor components, electrochemical reactors and use of membranes, reactor components and reactor for oxidation reactions' US Patent 5,744,015 (1998)

[66] Schulze-Küppers F., ten Donkelaar S.F.P, Baumann S., Prigorodov P.,Sohn Y.J., Bouwmeester H.J.M, Meulenberg W.A., 'Structural and functional properties of $SrTi_{1-x}Fe_xO_{3-\delta}$ ($0 \leqslant x \leqslant 1$) for the use as oxygen transport membrane', Separation and Purification Technology (2014) in press

[67] Jordal K., Bredesen R., Kvamsdal H.M., Bolland O., 'Integration of H2-separating membrane technology in gas turbine processes for CO2 capture' Energy 29 (2004) 1269-1278

[68] Czyperek M., Zappa P., Bouwmeester H.J.M., Modigell M., Ebertd K., Voigt I. Meulenberg W.A, Singheiser L., Stöver D. 'Gas separation membranes for zero-emission fossil power plants: MEM-BRAIN'. Journal of Membrane Science 359 (2010) 149-159

[69] Yahima T., Koide K., Fukatsu N., Osashi T., Iwahara H., 'A new hydrogen sensor for molten aluminum'. Sensors and Actuators B, 13-14 (1993) 697-699

[70] Iwahara, H., Technological challenges in the application of proton conducting ceramics'. Solid State Ionics, 77 (1995) 289

[71] Iwahara H. Uchida H., Tanaka S., 'High Temperature type proton conductor based on $SrCeO_3$ and its application to solid electrolyte fuel cells'. Solid State Ionics, 9-10 (1983) 1021

[72] Iwahara H., 'Proton conducting ceramics and their applications'. Solid state Ionics, 86-88 (1996) 9-15

[73] Norby T., 'Solid-state protonic conductors: principles, progress and prospects'. Solid State Ionics 125 (1999) 1-11

[74] Fontaine M.L., Norby T., Larring Y., Grande T., Bredesen R., Chapter 10 'Oxygen and Hydrogen Separation Membranes based on dense ceramic conductors' in Membrane Science and Technology, Volume 13

[75] Norby T., Larring Y., 'Concentration and transport of protons and oxygen defects in oxides, in Ceramic Oxygen Ion Conductors and their technological applications', Steele, B.C., Editor (1996) The Institute of materials

[76] Iwahara H., Ushida H., Maeda N., 'High temperature fuel and steam electrolysis cells using proton conductive solid electrolytes' Journal of Power Sources, 7 (1982) 293-301

[77] Norby T., Kofstad P., 'Proton and native-ion conductivities in Y_2O_3 at high temperatures' Solid State Ionics., 20 (1986) 169-184

[78] Li K., Ceramic Membranes for Separation and Reaction., Wiley 2007

[79] Sammells A.F., Mundschau M.V:, Gupta V.K., Lin J.Y.S., 'Nonporous Inorganic Membranes: for Chemical Processing', chapter 2, Ceramic proton conductors, 2006 Wiley-VCH Verlag GmbH & Co

[80] Shirsat A. N., Kaimal K.N.G., Bharadwaj, Das D., 'Thermodynamic stability of $SrCeO_3$', Journal of Solid State Chemistry, 177 (2004) 2007-2013

[81] Slade R. 'The Perovskite-type proton-conducting solid electrolyte $BaCe_{0.90}Y_{0.10}O_{3-\delta}$ in high temperature electrochemical cells', Solid State Ionics, 61 (1993) 111-114

[82] Kreuer K., 'Aspects of the formation and mobility of protonic charge carriers and the stability of perovskite-type oxides'. Solid State Ionics, 125 (1999) 285-302

[83] Schober T., Bohn H., 'Water vapor solubility and electrochemical characterization of the high temperature proton conductor $BaZr_{0.9}Y_{0.1}O_{2.95}$'. Solid State Ionics, 127 (2000) 351-360

[84] Fukui T., Ohara S., Kawatsu, 'Ionic conductivity of gadolinium doped barium praseodymium oxide'. Solid State Ionics, 116 (1999) 331-337

[85] Shin S., Huang H., Ishigame M., Iwahara H., 'Protonic conduction in the single crystals of $SrZrO_3$ and $SrCeO_3$ doped with Y_2O_3'. Solid State Ionics, 40 (1991) 910-913

[86] Iwahara H., Yahima T., Hibino T., Ozaki K., Suzuki H., 'Protonic conduction in calcium, strontium and barium zirconates'. Solid State Ionics 61 (1993) 65-69

[87] Yahima T., Kazeoka H., Yogo T,. Iwahara H., 'Proton conduction in sintered oxides base on $CaZrO_3$', Solid State Ionics, 47 (1991) 271-275

[88] Sata N., Hiramoto K., Ishigamw M., Hosoya S., Nijumuma, N. Shin., 'Site identification of protons in $SrTiO_3$: mechanism for large protonic conduction'. Physics Reviews, B 54 (1996) 15795-99

[89] Meulenberg, W.A.; Ivanova, M.E.; Roitsch, St.; Serra, J.M. (2011). 'Proton‐conducting ceramic membranes for solid oxide fuel cells and hydrogen (H_2) processing'. In *Advanced membrane science and technology for sustainable energy and environmental applications*, Part IV Membranes for alternative energy applications: batteries, fuel cells and hydrogen (H_2) production, Edts: Angelo Basile, Suzana Pereira Nunes, Woodhead Publishing Series in Energy №25, Woodhead Publishing Limited, Cambridge, UK, ISBN978‐1‐84569‐969‐7, 541‐567 (Chapter 17).

[90] Ivanova, M.E.; Ricote, S.; Baumann, St.; Meulenberg, W.A.; Tietz, F.; Serra, J.M.; Richter, H.. ,Ceramic materials for energy and environmental applications: functionalizing of properties by tailored compositions' in 'Doping: Properties, Mechanisms and Applications', NOVA Science Publishers Inc., NY, USA, (2012) Chapter in press.

[91] Yahima T., Iwahara H., Uchida H., 'Protonic and oxide ionic conduction in $BaCeO_3$- based ceramics-effect of partial substitution for Ba in $BaCe_{0.9}O_{3-\delta}$ with Ca'. Solid State Ionics, 47 (1991) 117-124

[92] Yajima T., Suzuki H., Yogo T., Iwahara, 'Protonic conduction in $SrZrO_3$-based oxides'. Solid State Ionics, 51 (1992) 101-107

[93] Matzke T., Cappadonia M., 'Proton conductive Perovskite solid solutions with enhanced mechanical stability', Solid State Ionics, 86-88 (1996) 659-663

[94] Meulenberg W.A., Ivanova M.E., van Gestel T., Bram T., Buchkremer H.P., Stöver D., Serra J.M., 'State of the art of ceramic membranes for hydrogen separation'. In Hydrogen and Fuel Cells, Edt Stolten D., Wiley-VCH Verlag, Weinheim, (Chapter 16) (2010)

[95] Nomura K., Takeuchi T., Kamo, Kageyama, Miyazaki, 'Proton conduction in doped $LaScO_3$ perovskites', Solid State Ionics 175 (2004) 553-555

[96] Norby T., Dyrlie O., Kofstad P., 'Protonic conduction in acceptor-doped cubic earth sesquioxides', Journal of the American Ceramic Society 75 (1992) 1176-1181

[97] Larring Y., Norby T., 'Protons in rare earth oxides', Solid State Ionics, 77 (1995) 147-151

[98] Larring Y., Norby T., 'The equilibrium between water vapor, protons, and oxygen vacancies in rare earth oxides', Solid State Ionics, 97 (1997) 523-528

[99] Nigara Y., Mizusaki J., Kawamura K., Ishigame M., 'Hydrogen Permeability in $(CeO_2)_{0.9}(CaO)_{0.1}$ at high temperatures', Solid State Ionics, 113-115 (1998) 347-354

[100] Nigara Y., Kawamura K., Mizusaki J., Ishigame M., 'Hydrogen Permeability in CeO_2 at high temperatures'. Journal of the Eletrochemical Society, 146 (1999) 2948-2953

[101] Nigara Y., Kawamura K., Kawada T., Mizusaki J., 'Hydrogen Permeability in sintered CeO_2 at high temperatures', Solid State Ionics, 136-137 (2000) 215-221

[102] Shimura T., Komori M., Iwahara H., 'Ionic conduction in pyrochlore-type oxides containing rare earth elements at high temperature'. Solid State Ionics 86 (1996) 685-689

[103] Norby T., Christiansen N., 'Proton conduction in Ca- and Sr- substituted $LaPO_4$', Solid State Ionics, 77 (1995) 240-243

[104] Chang L.L.Y., Philips B., 'Samarium and lanthanum tungstates of the $3R_2O_3{\cdot}WO_3$ type', Inorganic. Chemistry 3 (1964) 1792-1794

[105] Mc Carthy G.J., Fischer R.D., Johnson Jr., Gooden C.E.,' Crystal chemistry and compound formation in the systems rare earth sesquioxide WO_3' NBS Special Publication: Solid State Chemistry (1972) 364, 397

[106] Shimura T., Fujimoto S., Iwahara H., 'Proton conduction in non-perovskite-type oxides at elevated temperatures' Solid State Ionics 143 (2001) 117-123

[107] Haugsrud R., 'Defects and transport properties in Ln_6WO_{12}' Solid State Ionics 178 (2007) 555-560

[108] Escolastico S., Vert V.B., Serra J.M., 'Preparation and Characterization of Nanocrystalline Mixed Proton−Electronic Conducting Materials Based on the System Ln_6WO_{12}' Chemistry of Materials. 21 (2009) 3079-3089

[109] Norby T., Larring Y., 'Mixed hydrogen ion- electronic conductors for hydrogen permeable membranes'. Solid State Ionics, 136 (2000) 139-148

[110] Yoshimura M., Baumard J.F., 'Electrical conductivity of solid solutions in the system CeO_2-La_6WO_{12}', Materials Research Bulletin 10 (1975) 983-988

[111] Shimura T., Fujimoto S., Iwahara H., 'Proton conduction in non-perovskite-type oxides at elevated temperatures'. Solid State Ionics 143 (2001) 117-123

[112] Haugsrud R., 'Defects and transport properties in Ln_6WO_{12} (Ln=La, Nd, Gd, Er)'. Solid State Ionics 178 (2007) 555-560

[113] Hausgrud R., KjØlseth C., 'Effects of protons and acceptor substitution on the electrical conductivity of La_6WO_{12}'. Journal of Physics and Chemistry of Solids 69 (2008) 1758-1765

[114] Ivanova M.M., Balagina G,M., Rode E., Ya. Inorganic Materials (USSR) 6 (1970) 803

[115] Yoshimura M., Rouanet A., 'High temperature phase relation in the system La_2O_3-WO_3' Materials Research Bulletin. 11 (1976) 151-158

[116] Magrasó A., Frontera C., Marreró-Lopez D., Núñez P., 'New crystal structure and characterization of lanthanum tungstate "La_6WO_{12}" prepared by freeze-drying synthesis', Dalton Transactions (2009) 10273-10283

[117] Solís C., Escolastico S., Haugsrud R., Serra J.M., $La_{5.5}WO_{12-\delta}$ 'Characterization of transport properties under oxidizing conditions: A conductivity oxidation study' The Journal of Physical Chemistry, 115 (2011) 11124-11131

[118] Seeger J., Ivanova M., Meulenberg W.A., Sebold D., Stöver D., Scherb T., Schumacher G., Escolástico S., Solís C., Serra J.M., 'Synthesis and characterization of non-substituted and substituted proton-conducting $La_{6-x}WO_{12-y}$', Inorganic Chemistry 52 (2013) 10375-10386

[119] Chambrier M., Ibberson R., Goutenoire F., 'Structure determination of a-$La_6W_2O_{15}$', Journal Solid State Chemistry 183 (2010) 1297-1302

[120] Ivanova M., Seeger J., Serra J.M., Solis C., Meulenberg W.A., Fischer W., Roitsch S., Buchkremer H.P., 'Influence of the $La_6W_2O_{15}$ phase on the properties and integrity of $La_{6-x}WO_{12-\delta}$-based membranes' Chemistry and Materials Research 2 (2012) 56-81

[121] Sherb T., PhD Thesis, Technische Universität Berlin, doi:http:// dx.doi,org/10.5442/d0014

[122] T. Scherb, S.A.J. Kimber, C. Stephan, G. Schumacher, S. Escolastico, J M. Serra, P.F. Henry, A. H. Hill, J. Seeger, J. Banhart, 'Nanoscale order in the frustrated mixed conductor $La_{5.4}WO_{12-\delta}$' 2013 **rXiv:1305.3385**.

[123] Magraso A., Polfus J., Frontera C., Canales-Vazquez J., Kalland L., Hervoches C., Erdal S., Hancke R., Islam S., Norby T., Haugsrud R., 'Complete structural model for lanthanum tungstate: a chemically stable high temperature proton conductor by means of intrinsic defects', Journal of Materials Chemistry, 22 (2012) 1762

[124] Ivanova M., Seeger J., Serra J.M., Solis C., Meulenberg W., Fischer W., Roitsch S., Buchkremer H., 'Influence of the $La_6W_2O_{15}$ phase on the properties and integrity of $La_{6-x}WO_{12-\delta}$ based membranes', Chemistry and Materials Research 2 (2012) 56-81

[125] Escolastico S., Solis C., Serra J.M., 'Study of hydrogen permeation in $(La_{5/6}Nd_{1/6})_{5.5}WO_{12-\delta}$ membranes'. Solid State Ionics 216 (2012) 31-35

[126] Escolastico S., Solis C., Serra J.M., 'Hydrogen separation and stability study of ceramic membranes based on the system Nd_5LnWO_{12}'. Journal Hydrogen Energy 36 (2011) 11946-11954

[127] Haugsrud, R.; Norby, T. 'Proton conductivity in acceptor substituted $LnTaO_4$'. Journal of American Ceramic Society 90 (2007)1116 – 1121

[128] Weirich ., Gurauskis J., Gil V., Wiik K., Einarsrud M.A., 'Preparation of lantanum tungstate membranes by tape casting technique'. International Journal of Hydrogen Energy 37 **(**2012) 8056-8061

[129] Abedini R., Nezhadmoghadam, 'Application of membrane in gas separation processes: Its suitability and mechanisms' Petroleum and Coal 52 (2010) 69-80

[130] Vente J., Haije W., Jipelaan R., Rusting F., 'On the full scale module design of an air separation unit using mixed ionic electronic conducting membranes' Journal Membrane Science 278 (2006) 66-71

[131] Baumann S., Meulenberg W.A., Buchkremer H.P., Feature article 'Manufacturing strategies for asymmetric ceramic membranes for efficient separation of oxygen from air'. Journal of the European Ceramic Society 33 (2013) 1251-1261

[132] Vente F., Haije W.G., IJpelaan R., Rusting F.T., 'On the full-scale module design of an air separation unit using mixed ionic electronic conducting membranes' Journal of Membrane Science 278 (2006) 66-71

[133] Bruun T, Werswick B. 'Method and equipment for distribution of two fluids into and out of the channels in a multi-channel monolithic structure and use thereof', EP1 627 198 B1. Patent granted on 21.02.2007

[134] Mistler RE. 'Tape casting: past, present, potential'. American Ceramic Society Bulletin 77 (1998) 82-86

[135] http://www.airproducts.com/~/media/Files/PDF/industries/energy-ITM-datasheet-35404.pdf

[136] Bose AC, Stiegel GJ, Armstrong PA, Halper BJ, 'Progress in Ion Transport membranes for Gas Separation Applications' In: Bode AC, editor, Inorganic Membranes for Energy and Environmental Applications, Springer Science+Business Media; 2009

[137] Hendriksen P.V., Larsen P.H., Mogensen M., Poulsen F.W., Wiik K., 'Prospects and problems of dense oxygen permeable membranes' Catalysis Today 56 (2000) 283-295

[138] Julsrud 'Solid Multicomponent mixed proton and electron conducting materials', United States Patent US 7,288,135 B2 October 2007

[139] Kwok K., Frandsen H.L., Søgard M., Hendriksen P.V 'Mechanical reliability of geometrically imperfect tubular oxygen transport membranes' Journal of Membrane Science 470 (2014) 80-89

[140] Rutkowski B., Malzbender J., Beck T., Steinbrech R.W., Singheiser L., 'Creep behavior of tubular $Ba_{0.5}Sr_{0.5}Co_{0.8}Fe_{0.2}O_{3-\delta}$ gas separation membranes' Journal European Ceramic Society 31 (2011) 493-499

[141] www.ami.ac.uk

[142] Morrel R., McCormick N., Bevan J., Lodeiro M., Margetson J., 'Biaxial disc flexure-modulus and strength testing'. British Ceramics Transactions, 98 (1999) 234-240

[143] Lord J.D., Morrell R., Elastic modulus measurement, Measurement good practice Guide No 98, Center for Materials measurement and technology, National Physical Laboratory, 2007

[144] De With G. Wagemans H.M., 'Ball-on-ring test revisited' Journal of American Ceramic Society 72 (1989) 1538-1541

[145] http://www.mtm.kuleuven.be

[146] Malzbender J., Huang B., Mönch J., , 'A comparison of results obtained using different methods to assess the elastic properties of ceramic materials exemplified for $Ba_{0.5}Sr_{0.5}Co_{0.8}Fe_{0.2}O_{3-\delta}$' Journal of Materials Science 45 (2010) 1227-1230

[147] Huang B.X., Malzbender J., Steinbrech R.W., Singheiser L., 'Discussion of the complex thermo-mechanical behavior of $Ba_{0.5}Sr_{0.5}Co_{0.8}Fe_{0.2}O_{3-\delta}$' Journal of membrane Science 359 (2010) 80-85

[148] Lipinska-Chwalek M., Malzbender J., Chanda A., Baumann S., Steinbrech R.W., 'Mechanical characterization of porous $Ba_{0.5}Sr_{0.5}Co_{0.8}Fe_{0.2}O_{3-\delta}$' Journal of the European Ceramic Society 31 (2011) 2997-3002

[149] Lein H.L., Andersen S., Vullum P.E., Lara-Curzio E., Holmestad R., Einarsrud M.A., Grande T., 'Mechanical Properties of mixed conducting $La_{0.5}Sr_{0.5}Fe_{1-x}Co_xO_{3-\delta}$ ($0 \le x \le 1$) materials' Journal of Solid State Electrochemistry 10 (2006) 635-642

[150] Ledbetter H., Lei M., Kim S., 'Elastic constants, Debye temperatures and electron-phonon parameters of superconducting cuprates and related oxides' Phase Transitions, 23 (1990) 61-70

[151] Yasuda K., Uemura K., Shiota T., 'Sintering and mechanical properties of gadolinium-doped ceria ceramics', Journal of Physics, 339 (2012) 1-4

[152] Pećanac G., 'Thermo - mechanical investigations and predictions for oxygen transport membrane materials' PhD Thesis, RWTH Aachen 2012

[153] Huang B.X., 'Thermomechanical Properties of Mixed Ion-Electron Conducting Membrane Materials' PhD Thesis RWTH Aachen 2010

[154] Goretta K.C., Park E.T., Koritala R.E., Cuber M.M., Pascual E.A., Chen N., de Arellano-López A.R., Routbort J.L., 'Thermomechanical response of polycrystalline $BaZrO_3$' Physica C:Superconductivity 309 (1998) 245-250

[155] Yamanaka S., Fujikane M., Hamaguchi T., Muta H., Oyama T., Matsuda T., Kobayashi S., Kurosak K., 'Thermophysical properties of $BaZrO_3$ and $BaCeO_3$' Journal of Alloys and Compounds 359 (2003) 109–113

[156] Roa J.J., Magrasó A., Morales M., Núñez P, Segarra M., 'Determination of hardness, Young's modulus and fracture toughness of lanthanum tungstates as novel proton conductors' Ceramics International 37 (2011) 1593-1599

[157] Tagaki T., Choa Y.A., Sekino T., Niihara K., 'Fabrication and Mechanical properties of $LaNbO_4$ and $LaNbO_4/Al_2O_3$ composites', Key Engineering Materials 161-163 (1999) 181-184

[158] Hillig WB 'General Electric, corporate research and development' No. 85CRD152 1985

[159] ASTM C1239-07 Standard Practice for Reporting Uniaxial Strength data and estimating Weibull Distribution Parameters for Advanced ceramics

[160] Weibull W., 'A statistical theory of the strength of materials' Royal Institute for Eng Res, Stockholm 151 (1939) 1-45

[161].Menćík J., 'Strength and fracture of glass and ceramics', Vol 12 Glass Science and Technology, Elsevier. 1992

[162] ASTM C1683-08 'Size Scaling of tensile strengths using Weibull statistics for advanced ceramics'

[163] Huang B.X., Malzbender J., Steinbrech R.W., Singheiser L., 'Mechanical properties of $La_{0.58}Sr_{0.4}Co_{0.2}Fe_{0.8}O_{3-\delta}$ membranes', Solid State Ionics, 180 (2009) 241-245

[164] Lipińska-Chwałek M., Kiesel L., Malzbender J. 'Mechanical properties of porous MgO substrates for membrane applications' Journal of the European Ceramic Society 34 (2014) 2519–2524

[165] Wiederhorn S.M., 'Subcritical Crack Growth' in Fracture Mechanics of ceramics Vol 2 (1974) 613-646

[166] ASTM C1465 – 08 'Standard Test Method for Determination of Slow Crack Growth Parameters of Advanced Ceramics by Constant Stress-Rate Flexural Testing at Elevated Temperatures' ASTM International, West Conshohocken, PA, 2013, www.astm.org

[167] Choi S.R., Salem J.A., Holland F.A., 'Estimation of Slow crack growth parameters for constant stress-rate test', Data of Advanced Ceramics and Glass by the Individual Data and Arithmetic Mean Methods, NASA Technical Memorandum 107369, 1997

[168] Barsoum W., 'Fundamentals of Ceramics', Published by Institute of Physics Publishing, London

[169] Yang K.H., Ho N.J., Lu H.Y., 'Deformation Microstructure in (001) Single Crystal Strontium Titanate by Vickers Indentation' J. Am. Ceram. Soc., 92 (2009) 2345–2353

[170] Routbort J.L., Goretta K.C., Doshi R., Richards V. L., Krumpelt M., Wolfenstine J., De Arellano-López A. R., 'Mechanical Properties of $Ce_{0.9}Gd_{0.1}O_{2-x}$ and $Ce_{0.9}Gd_{0.1}O_{2-x}+Al_2O_3$ Composites' 22nd Annual Conference on Composites, Advanced Ceramics, Materials, and Structures: A: Ceramic Engineering and Science Proceedings, Volume 19, Issue 3

[171] Dierickx D., Houben I., 'Dense polycrystalline $BaZrO_3$ substrates for $YBa_2Cu_3O_{7-x}$ melt processing' Journal of Materials Science Letters 15 (1996) 1573-1576

[172] Mokkelbost T., Lein H.L., Vulum P.E., Holmestand R., Grande T., Einarsrud M.A., 'Thermal and mechanical properties of $LaNbO_4$-based ceramics' Ceramics International 35 (2009) 2877–2883

[173] Chanda A., Huang B.X., Malzbender J., Steinbrech R.W., 'Micro- and macro-indentation behavior of $Ba_{0.5}Sr_{0.5}Co_{0.8}Fe_{0.2}O3_{-d}$ perovskite' Journal of the European Ceramic Society 31 (2011) 401-408

[174] Roa J.J., Magraso A., Morales M., Nunez P., Segarra M. 'Determination of hardness, Young's Modulus and fracture toughness of lanthanum tungstate as novel proton productors' Ceramics International 37 (2011) 1593-1599

[175] Quinn G.D., 'Fractography of ceramics and glasses'. Practice Guide, NIST National Institute of standards and Technology, Special Publication 960-17 (2007)

[176] ASTM C 1322-05b. Standard Practice for Fractography and Characterization of Fracture Origins in Advanced Ceramics

[177] Griffith A.A., 'The phenomena of rupture and flow in solids', Philosophical Transactions if the Royal Society of London, A 221 (1921) 163-198

[178] Irwin G., 'Analysis of stresses and strains near the end of a crack traversing a plate', Journal of Applied Mechanics, 24 (1957) 361-364

[179] Anderson T.L., 'Fracture mechanics: fundamentals and applications'., (2005) CRC Press 2005

[180] Toonder J.M.J., 'A general introduction to fracture mechanics and mechanical strength of materials' Unclassified report, Philips Electronics., (1998)

[181] Mechanical Testing Handbook, Volume 8, ASM International, 2000

[182] Green D., 'An introduction to the mechanical properties of ceramics', Cambridge Solid State Science Series, Cambridge University Press, 1998

[183] Ashby M.F. Jones D.R.H., 'Engineering materials I: An introduction to their properties and applications', Pergamos Press, 1980

[184] Yi J.X., Lein H.L., Grande T., Yakovlev S., Bouwmeester H.J.M. 'High temperature compressive creep behavior of the perovskite-type oxide $Ba_{0.5}Sr_{0.5}Co_{0.8}Fe_{0.2}O_{3-\delta}$' Solid State Ionics 180 (2009) 1564–1568.

[185] Nabarro F.R.N., 'Report on a conference on strength of solids', the physical society of London, (1948) 75

[186] Herring C.J., 'Diffusional viscosity of a polycrystalline solid', Journal of Applied Physics, 21 (1950) 437-445

[187] Coble R., 'Model for boundary Diffusion- Controlled Creep in Polycrystalline materials, Journal of Applied Physics, 34 (1693) 1679-1682

[188] Chokshi A.H., 'Diffusion creep in oxide ceramics', Journal of the European Ceramic Society, 22 (2002) 2469-2478

[189] Bretheau T., Castaing J., Rabier J.,Veyssière P. 'Summary Dislocation motion and high temperature plasticity of binary and ternary oxides', Advances in Physics, 28:6 (1979) 829-834

[190] Cannon W.R., Langdon T.G., 'Creep of Ceramics: I-Mechanical Characteristics' Journal Materials Science 18 (1983) 1

[191] Cahn R.W., Haasen P., Kramer E.J., Chapter 7. Mechanical properties in Materials Science and Technology, Volume 11 'Structure and properties of ceramics' VCH

[192] Hynes A., Doremus R., 'Theories of creep in ceramics, Critical Reviews in Solid State and materials Sciences, Theories of creep in ceramics' 21 (1996) 129-187

[193] Lipińska-Chwałek M, Pećanac G., Malzbender J. 'Creep behavior of membrane and substrate materials for oxygen separation units' Journal of European Ceramic Society 33 (2013) 1841-1848

[194] K.C. Goretta Park E.T., Koritala R.E., Cuber M.M., Pascual E.A., Chen N., de Arellano-Lopez A.R., Routbort J.L. 'Thermomechanical response of polycrystalline $BaZrO_3$'Physica C 309 (1998) 245

[195] K.C. Goretta, Park E.T., Guan J., Balachandran U., Dorris S.E., Routbort J.L., 'Diffusional creep of $BaCe_{0.8}Y_{0.2}O_{3-\alpha}$ mixed conductors' Solid State Ionics 111 (1998) 295

[196] Dokko P., Pask J.A., 'Plastic Deformation of ceramics' Materials Science and Engineering 25 (1976) 77-86

[197] Wang C.M., Cargill G.S., Harmer M.P., Chan H.M., Cho J 'Atomic structural environment of grain boundary segregated Y and Zr in creep resistant alumina from EXAFS' Acta materialia 47 (1999) 3411-3422

[198] French J.D., Zhao J., Harmer M.P., Chan Miller G.A., 'Creep of duplex microstructures' Journal of American ceramic society 77 (1994) 2857

[199] Li Y.Z., Wang C., Chan C., Rickman H.M., Harmer M.P., Chabala J.M., Gavrilov K.L., Levi-Setti R., 'Co-doping of Alumina to Enhance Creep Resistance' Journal of American Ceramic Society 82 (1999) 1497

[200] Lartigue S., Carry C, and Priester L., 'Grain Boundaries in High Temperature Deformation of Yttria and Magnesia Co-doped Alumina' Journal Physical Colloques (Paris), C1 51(1990) 985–990

[201] Robertson G., Wilkinson D. S., Caćeres C. H., 'Creep and Creep Fracture in Hot-Pressed Alumina' Journal American Ceramic Society 74 (1991)915–921

[202] Wakai F., Iga T., Nagano T., 'Effect of Dispersion of ZrO_2 Particles on Creep of Fine-Grained Alumina' Journal American Ceramic Society 96 (1988) 1206–1209

[203] Cho J., Wang C.M., Chan H.M., Rickman J.M., Harmer M.P, 'Role of segregating dopants on the improved creep resistance of aluminum oxide' Acta Materialia 47 (1999) 4917-4207

[204] Kleveland K., Wereszczak A., Kirkland P., Einarsrud M.A., Grande T., 'Compressive creep performance of $SrFeO_3$' Journal of American Ceramic Society 84 (2001) 1822-1826

[205] Majkic G., Wheeler L., Salama K. 'Characterization of creep behavior of $SrCo_{0.8}Fe_{0.2}O_{3-\delta}$' Acta Materialia 48 (2000) 1907-1917

[206] Ashby M.F., Verall R.A., 'Diffusion-accommodated flow and superplasticity' Acta metallurgica 21 (1973) 149-163

[207] Arellano-López A.R. Balachandran U. Goretta K.C., Routbort J.L., 'High-temperature deformation of $Sr(FeCo)_{1.5}O_x$ ceramics' Acta Materialia 49 (2001) 3109-3116

[208] Singh D., Lorenzo-Martín M., Chen G., Gutiérrez-Mora, Routbort J.L., 'High-temperature deformation behavior in $SrTiO_3$ ceramics' Journal of the European Ceramic Society 27 (2007) 3377-3384

[209] Turlier P., Bussiere P., Prettre M., 'Application de la methode de Kryukov Et Zhukhovitskii a la mesure du coefficient dautodiffusion du strontium dans le metatitanate $SrTiO_3$' Comptes Rendus de l'Académie des sciences 250 (1960) 1649

[210] Park E.T., Nash P., Wolfenstine J., Goretta K.C., Routbort J.L., 'High-temperature creep of polycrystalline $BaTiO_3$." Journal Materials Reséarch 14 (1999) 523-528

[211] Wang Z., Karato S., Fujino K., 'High temperature creep of single crystal strontium titanate ($SrTiO_3$): a contribution to creep systematics in perovskites' 'Physics of the Earth and Planetary Interiors' 79 (1993) 299-312

[212] Wright K., 'Rheology of perovskites and its implications for mantle dynamics'. PhD Thesis. Department of Geological Science, University College, London, United Kingdom, 1991

[213] Domínguez-Rodríguez A., Castaing J., Goretta K.C., Routbort J.L., in point defects and related properties of ceramics ed T.O. Mason and and J.L Routbort American Ceramic Society Westerville, OH, USA 1991, p 139

[214] Thomson D.R., Bool L.E., Chen J.C., 'Oxygen enhanced combustion for NO_x control' Final report, Praxair, 2004

[215] Schulz M., Kriegel R., Burckhardt W., 'Modeling of oxygen flux and stress distribution for $Ba_{0.5}Sr_{0.5}Co_{0.8}Fe_{0.2}O_{3-\delta}$ membranes at application conditions' 10th International Conference of Inorganic Membranes, Japan, 2008

[216] Majkic G.,Wheeler L.T., Salama K. 'Stress-induced diffusion and defect chemistry of $La_{0.2}Sr_{0.8}Fe_{0.8}Cr_{0.2}O_{3-\delta}$: Part 1—creep in controlled-oxygen atmosphere' Solid State Ionics 164 (2003) 137-148

[217] Mitchell T.E., Hobbs L.W., Heuer A.H., Castaing J., Cadoz J., Philibert J., 'Overview No 6: Interaction between point defects and dislocations in oxides' Acta Metallurgica 27 (1979) 1677

[218] Philibert J., 'Creep and diffusion' Solid State Ionics 12 (1984) 321

[219] Poirer J.P., 'Creep of crystals' Cambridge Earth and Science Series, Cambridge, 1985

[220] Kleveland K, Einaursrud M.A., Grande T., 'Sintering behavior, Microstructure. And phase composition of $Sr(Fe, Co)O_{3-\delta}$ ceramics', Journal of American ceramic society 83 (2000) 3158-64

[221] C1322-05b 'Standard Practice for Fractography and Characterization of Fracture Origins in Advanced Ceramics' ASTM International

[222] http://www.veqter.co.uk

[223] http://www.gla.ac.uk/

[224] http://www.oxford-instruments.com/products/microanalysis/ebsd

[225] DIN 50359 – 1 (1997-10-00) Testing of metallic materials – Universal hardness testing – Part I: Test method, DIN Deutsches Institut für Normung e.V.

[226] ASTM C1327-08 Standard Test Method for Vickers Indentation Hardness of Advanced Ceramics, ASTM International, West Conshohocken, PA, 2008, www.astm.org

[227] Hay J.L., Pharr 'Instrumented indentation testing'. In: ASM Handbook, Mechanical Testing and Evaluation, Vol. 8, ed. by H. Kuhn, D. Medlin (ASM Int., Materials Park 2000)

[228] A.C. Fischer-Crips: Nanoindentation Springer, Berlin Heidelberg 2002

[229] Oliver W.C., Pharr G.M., 'Measurement of hardness and elastic modulus by instrumented indentation: Advances in understanding and refinements to methodology", Journal Materials. Research 19 (2004) 3-21.

[230] Gubicza J., Juhász A., Tasnádi P., Aratö P., Vörös G., 'A new method for hardness determination from depth sensing indentation tests' Journal of Materials Science 31 (1996) 3109-3114.

[231] Ponton C.B., Rawlings R.D 'Vickers indentation fracture toughness test Part 2:Application and critical evaluation of standardized indentation toughness equations' Materials Science and technology 5 (1989) 865-872

[232] McColm I.J., 'Ceramic hardness', Plenum Press, New York (1990)

[233] Anstis G.R., Chantikul P., Lawn B.R., Marshall D.B., 'A critical evaluation of Indentation techniques for measuring fracture toughness: I, direct crack measurements', Journal of American Ceramic Society., 64 (1981) 533-538

[234] ASTM E 1876 – 01: Standard Test Method for Dynamic Young's Modulus, Shear Modulus and Poisson's Ratio by Impulse Excitation of Vibration

[235] ASTM Standard C1499-05 'Test Method for Monotonic Equibiaxial Flexural Strength of Advanced Ceramics at ambient temperature" ASTM International, DOI: 10.1520/C1499-05, www.astm.org

[236] Morrel R., 'Biaxial flexural strength testing of ceramic materials'. Measurement good practice guide No. 12, centre for Materials measurement and technology, National Physical Laboratory, 2007

[237] Choi S.R., Salem J.A., Holland F.A., NASA Technical Memorandum 107369 (1997)

[238] ASTM Standard C 1499 – 05, Standard test method for monotonic equibiaxial flexure strength of advanced ceramics at ambient temperature, ASTM, 2004

[239] Salem, J. A. and Powers, L., 'Guidelines for the testing of plates'. Proceedings 27th International Cocoa Beach Conference. Ceram. Eng. Sci. Proc., 2003, 24(4), 357–364.

.

[240] DIN 51105: 2010-08 'Advanced technical ceramics- Mechanical properties of monolithic ceramics at room temperature- Determination of flexural strength by the ring-on-ring test

[241] ASTM F 394-78 (reapproved 1996), Standard test method for biaxial flexure test (modulus or rapture) of ceramic substrates

[242] Börger A., Supansci P., Danzer R., 'The ball on three balls test for strength testing of brittle discs: stress distribution in the disc'. Journal of the European Ceramic Society 22 (2002) 1425-1436

[243] Börger A., Supancic P., Danzer R., 'The ball on three balls test for strength testing of brittle discs: Part II: analysis of possible errors in the strength determination', Journal of the European Ceramic Society 24 (2004) 2917-2928

[244] Danzer R., Harrer W., Supancic P., Lube T., Wang Z., Börger A., 'The ball on three balls test-Strength and failure analysis of different materials', Journal of the European ceramic society 27 (2007) 1481-1485

[245] Danzer R., Supancic P., Harrer W., 'Biaxial Tensile Strength test for brittle rectangular plates' Journal of the ceramic Society of Japan 114 (11) (2006) 1054- 1060

[246] Fett T., Rizzi G., Ernst E., Müller R., Oberacker R., 'A 3-balls-on-balls strength test for ceramic discs' Journal of the European Ceramic Society **27** (2007) 1-12

[247] Börger A., Supancic P., Danzer R., 'The ball on three balls test for strength testing of brittle discs: stress distribution in the disc' Journal European Ceramic Society, 22 (2002) 1425-1436

[248] http://wm.unileoben.ac.at:8080/webMathematica/ISFK/B3B_strength_webApp.jsp

[249] Rutkowski Thesis, 'Mechanical Properties and Microstructureof Dense Ceramic Membranes for Oxygen Separation in Zero–Emission Power Plant' RWTH Aachen 2012

[250] Poteat L.E. 'Deformation Mechanisms in Thoria at Elevated Temperatures' PhD Thesis, North Carolina State University, Raleigh, N.C 1966 Order No. 66-11, 978

[251] Pfaff E., Kaletsch A., Broeckmann., 'Design of a Mixed Ionic/Electronic Conducting Oxygen Transport Membrane Pilot Module', Chemical Engineering Technology 35 (2012) 455-463

[252] Cocco F., Massazza, 'Microscopic study of the system SrO-TiO_2' Ann. Chim. (Rome) 53 (1963) 892

[253] F.J. Humphreys, M. Hatherly "Recrystallization and Related Annealing Phenomena" Elsevier, 2004, ISBN 978-0-08-044164-1

[254] Pećanac G., Kiesel L., Malzbender J., 'Steady-state creep of porous and an extended analysis on the creep of dense BSCFZ perovskite', Journal Membrane Science, 456 (2014) 134-138

[255] Palcut M, Wiik K., Grande T., 'Cation Self-Diffusion and Nonstoichiometry of Lanthanum Manganite Studied by Diffusion Couple Measurements', Journal of Physical. Chemistry. B. 111 (2007) 813-822

[256] Palcut M., Wiik K., Grande T., 'Cation Self-Diffusion in $LaCoO_3$ and La_2CoO_4 Studied by Diffusion Couple Experiments' Journal of Physical Chemistry B 111 (2007) 2299-2308

[257] Smith J.B., Norby T., 'On the Steady-State Oxygen Permeation Through $La_2Ni_{O4+\delta}$ Membranes' J. Electrochem. Soc. 153 (2006) A233-8

[258] Nabarro, F.R.N., Conference Strength of Solids (Phys. Soc., London 1948).

[259] Herring C. 'Diffusional Viscosity of a Polycrystalline Solid', Journal Applied Physics 2 (1950) 437-445

[260] Coble RL. 'A Model for Boundary Diffusion Controlled Creep in Polycrystalline Materials' Journal Applied Physics 34 (1963) 1679-1683

[261] Yi J.X., Lein H.L., Grande T., Yakovlev S, Bouwmeester H.J.M., 'High-temperature compressive creep behaviour of the perovskite-type oxide $Ba_{0.5}Sr_{0.5}Co_{0.8}Fe_{0.2}O_{3-\delta}$' Solid State Ionics (2009) 1564-1568

[262] Schröder M., Project MEM-BRAIN Status Report, Valencia, 2011

[263] Stournari V., ten Donkelaar S.F.P., Malzbender J., Beck T., Singheiser L.,. Bouwmeester H.J.M., 'Creep behavior of perovskite-type oxides $Ba_{0.5}Sr_{0.5}(Co_{0.8}Fe_{0.2})_{1-x}Zr_xO_{3-\delta}$', Journal of the European Ceramic Society, 35 (2015) 1841-1846

[264] Vegard L.,'Die Konstitution der Mischkristalle und die Raumfüllung der Atome, Zeitschrift für Physik', 5 (1921) 17-26

[265] Rothschild A., Litzerlman S.J., Tuller H.L., Menesklou W., Schneider T., Iverse-Tiffée E., 'Temperature-independent resistive oxygen sensors based on $SrTi_{1-x}Fe_xO_{3-\delta}$ solid solutions' Sensors and Actuators, B 108 (2005) 223-230

[266] Shannon R.D., Prewitt C. T., 'Effective ionic radii in oxides and fluorides', Acta Crystallographica., B25 (1969) 925-946

[267] Huang B.X., Steinbrech R.W., Baumann S., Malzbender J., 'Creep behavior and its correlation with defect chemistry of $La_{0.58}Sr_{0.4}Co_{0.2}Fe_{0.8}O_{3-\delta}$', Acta Materialia, 60 (2012) 2479-2484

[268] Steinvik S., Bugge R., Glonnes J., Tafto J., Norby 'The defect structure of $SrTi_{1-x}Fe_xO_{3-y}$ (x´=0 0.8) investigated by electrical conductivity measurements and electron energy loss spectroscopy (EELS)' Journal Physical chemistry of solids 58 (1997) 969-976

[269] Holt A., Glenne R., Norby T., 'Defects and Transport in $SrFe_{1-x}Co_xO_{3-\delta}$' Ionics 5 (1999) 434-443

[270] Freer R., 'Self-diffusion and impurity diffusion in oxides' Journal of materials science 15 (1980) 803-824

[271] Donkelaar S.F.P. ten, Stournari V., Malzbender J., Nijmeijer A., Bouwmeester H.J.M., 'High-temperature compressive creep behaviour of perovskite-type oxides $SrTi_{1-x}Fe_xO_{3-\delta}$' Journal of the European Ceramic Society, 35 (2015) 4203 - 4209

[272] Fagg D.P., Kharton V.V., Kovalensky A.V., Viskup A.P., Naumovich E.N., Frade J.R., 'The stability and mixed conductivity in La and Fe doped $SrTiO_3$ in the search for potential SOFC anode materials', Journal of the European Ceramic Society 21 (2001) 1831-1835

[273] Atkison A., Ramos T.M.G.M., 'Chemical-induced stresses in ceramic oxygen ion-conducting membranes', Solid State Ionics 129 (2000) 259-269

[274] McIntosh S., Vente J.F., Haije W.G., Blank D.H.A., Bouwmeester H.J.M., 'Oxygen stoichiometry and chemical expansion of $Ba_{0.5}Sr_{0.5}Co_{0.8}Fe_{0.2}O_{3-\delta}$ measured by in situ neutron diffraction' Chemistry of Materials 18 (2006) 2187-2193

[275] Balaguer- Ramirez M., PhD Thesis 'New solid state oxygen and hydrogen conducting materials. Towards their applications as high temperature electrochemical devices and gas separation membranes', Universitat Polytechnica de Valencia, 2013

[276] Atkinson A., Ramos T.M.G.M., 'Chemically-induced stresses in ceramic oxygen ion-conducting membranes', Solid State Ionics 129 (2000) 2559-269

[277] Trunec M., 'Effect of grain size on mechanical properties of 3Y-TZP ceramics', Ceramics − Silikáty 52 (2008)165-171

[278] Wachtman JB., 'Mechanical Properties of ceramics' Wiley, 2006, New York

[279] Vøllestad E., Norby T., Haugsrud R., 'Inter-diffusion in lanthanum tungsten oxide', Solid State Ionics, 244 (2013) 57-62

[280] Escolastico S., Seeger J., Roitsch S., Ivanova M., Meulenberg W.A., Serra J.M., 'Enhanced H_2 Separation through Mixed Proton–Electron Conducting Membranes Based on $La_{5.5}W_{0.8}Mo_{0.2}O_{11.25-d}$' ChemSusChem 6 (2013) 1523 – 1532

[281] Lein H.L., Wiik K., Einarsrud M.A., Grande T., 'High-Temperature Creep Behavior of Mixed Conducting
$La_{0.5}Sr_{0.5}Fe_{1-x}Co_xO_{3-\delta}$ ($0.5 \leq x \leq 1$) Materials' Journal of the American Ceramic Society 89 (2006) 2895–2898

[282] Zou Y., Schulze-Küppers F. Malzbender J., 'Creep behavior of porous $La_{0.6}Sr_{0.4}Co_{0.2}Fe_{0.8}O_{3-\delta}$ oxygen transport membrane supports' Ceramics International 41 (2015) 4064-4069

[283] Lipinska-Chwałek M., Pećanac G., Malzbender J., 'Creep behaviour of membrane and substrate materials for oxygen separation units' Journal of the European Ceramic Society 33 (2013) 1841–1848

[284] Kriegel R., Schulz M., Ritter K., Pippardt U., Sthahn M., Voigt I., 'Advanced Membrane Design for Oxygen Separation' 2. ICEPE, Book of Extended Abstracts. Dechema, Frankfurt a.M (2011) 114-117

Band / Volume 291
Characterization & Modification of Copper and Iron Oxide Nanoparticles for Application as Absorber Material in Silicon based Thin Film Solar Cells
M. R. Nuys (2015), XII, 123 pp
ISBN: 978-3-95806-096-8

Band / Volume 292
Interpretation of L-band brightness temperatures of differently tilled bare soil plots
M. Dimitrov (2015), XIV, 116 pp
ISBN: 978-3-95806-098-2

Band / Volume 293
Atrazine in the environment 20 years after its ban: long-term monitoring of a shallow aquifer (in western Germany) and soil residue analysis
D. S. Vonberg (2015), 149 pp
ISBN: 978-3-95806-099-9

Band / Volume 294
Yttria-Stabilized Zirconia / Gadolinium Zirconate Double-Layer Plasma-Sprayed Thermal Barrier Coating Systems (TBCs)
E. Bakan (2015), vi, 132 pp
ISBN: 978-3-95806-100-2

Band / Volume 295
Hydration and dehydration at the tropical tropopause
C. Schiller (2015), 72 pp
ISBN: 978-3-95806-101-9

Band / Volume 296
Influence of Impurities on the Fuel Retention in Fusion Reactors
M. Reinhart (2015), 140 pp
ISBN: 978-3-95806-105-7

Band / Volume 297
The role of abiotic processes in the formation and degradation of gaseous nitrogen compounds in the soil
J. Heil (2015), XIV, 106 pp
ISBN: 978-3-95806-106-4

Band / Volume 298
12th Carolus Magnus Summer School on Plasma and Fusion Energy Physics
edited by Kristel Crombé (2015), 468 pp
ISBN: 978-3-95806-107-1

Band / Volume 299
Optical near-field investigations of photonic structures for application in silicon-based thin-film solar cells
A. M. Ermes (2015), vi, 157 pp
ISBN: 978-3-95806-108-8

Band / Volume 300
Strom- und Gasmarktdesign zur Versorgung des deutschen Straßenverkehrs mit Wasserstoff
M. Robinius (2015), VI, 255 pp
ISBN: 978-3-95806-110-1

Band / Volume 301
Alterung von Vakuum-plasmagespritzten MCrAlY-Schutzschichten und ihre Wechselwirkung mit Nickel- und Cobalt-basierten γ/γ'-Superlegierungen
P. J. Terberger (2015), IX, 149 pp
ISBN: 978-3-95806-113-2

Band / Volume 302
Verbundvorhaben ELFA Effiziente Luftfahrzeuge
Brennstoffzellensysteme zur Energieerzeugung BREZEN – Teilprojekt: Kerosinaufbereitung
R. Peters, J. Meißner, J. Pasel, R. C. Samsun, D. Stolten
(2016), viii, 84 pp
ISBN: 978-3-95806-114-9

Band / Volume 303
Cavity-Ringdown-Spektroskopie zur Untersuchung der Rolle höherer Stickoxide für den nächtlichen Schadstoffabbau in der unteren Atmosphäre
S. Schrade (2016), II, 118 pp
ISBN: 978-3-95806-116-3

Band / Volume 304
Thermo-mechanical Properties of Mixed Ionic-Electronic Conducting Membranes for Gas Separation
V. K. Stournari (2016), 167 pp
ISBN: 978-3-95806-117-0

Weitere ***Schriften des Verlags im Forschungszentrum Jülich*** unter
http://wwwzb1.fz-juelich.de/verlagextern1/index.asp

Energie & Umwelt /
Energy & Environment
Band / Volume 304
ISBN 978-3-95806-117-0